

UNCLASSIFIED

AD **408 669**

DEFENSE DOCUMENTATION CENTER

FOR

SCIENTIFIC AND TECHNICAL INFORMATION

CAMERON STATION, ALEXANDRIA, VIRGINIA



UNCLASSIFIED

NOTICE: When government or other drawings, specifications or other data are used for any purpose other than in connection with a definitely related government procurement operation, the U. S. Government thereby incurs no responsibility, nor any obligation whatsoever; and the fact that the Government may have formulated, furnished, or in any way supplied the said drawings, specifications, or other data is not to be regarded by implication or otherwise as in any manner licensing the holder or any other person or corporation, or conveying any rights or permission to manufacture, use or sell any patented invention that may in any way be related thereto.

408 669

63 4-2

U. S. A R M Y
TRANSPORTATION RESEARCH COMMAND
FORT EUSTIS, VIRGINIA

CATALOGED BY DDC

AS AD No. 408 669

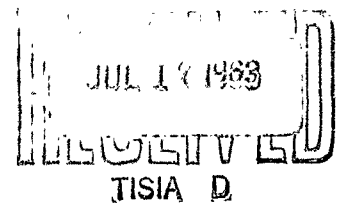
TRECOM TECHNICAL REPORT 63-11

**THEORETICAL AND EXPERIMENTAL STUDIES
OF IMPINGING UNIFORM JETS**

Task 1D121401A14129
(Formerly Task 9R38-01-017-29)

Contract DA 44-177-TC-782

April 1963



prepared by:

* CORNELL AERONAUTICAL LABORATORY, INC.
Buffalo 21, New York



DISCLAIMER NOTICE

When Government drawings, specifications, or other data are used for any purpose other than in connection with a definitely related Government procurement operation, the United States Government thereby incurs no responsibility nor any obligation whatsoever; and the fact that the Government may have formulated, furnished, or in any way supplied the said drawings, specifications, or other data is not to be regarded by implication or otherwise as in any manner licensing the holder or any other person or corporation, or conveying any rights or permission, to manufacture, use, or sell any patented invention that may in any way be related thereto.

* * *

ASTIA AVAILABILITY NOTICE

Qualified requesters may obtain copies of this report from

Armed Services Technical Information Agency
Arlington Hall Station
Arlington 12, Virginia

* * *

This report has been released to the Office of Technical Services, U. S. Department of Commerce, Washington 25, D. C., for sale to the general public.

* * *

The findings and recommendations contained in this report are those of the contractor and do not necessarily reflect the views of the U. S. Army Mobility Command, the U. S. Army Materiel Command, or the Department of the Army.

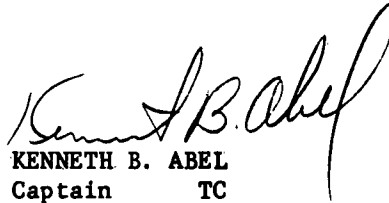
HEADQUARTERS

U. S. ARMY TRANSPORTATION RESEARCH COMMAND

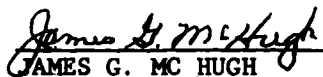
Fort Eustis, Virginia

This report has been reviewed by the U. S. Army Transportation Research Command and is considered to be technically sound. The report is published for the exchange of information and the stimulation of ideas.

FOR THE COMMANDER:


KENNETH B. ABEL
Captain TC
Adjutant

APPROVED BY:


JAMES G. MC HUGH
USATRECOM Project Engineer

Task 1D121401A14129
(Formerly Task 9R38-01-017-29)

Contract DA 44-177-TC-782

TRECOM Technical Report 63-11

April 1963

THEORETICAL AND EXPERIMENTAL STUDIES
OF IMPINGING UNIFORM JETS

CAL Report BB-1657-S-1

Prepared by
Cornell Aeronautical Laboratory, Inc.
Buffalo 21, New York

FOR
U. S. ARMY TRANSPORTATION RESEARCH COMMAND
FORT EUSTIS, VIRGINIA

FOREWORD

The work described in this report was accomplished by the Cornell Aeronautical Laboratory, Inc. (CAL), Buffalo, New York, for the U. S. Army Transportation Research Command (USATRECOM), Fort Eustis, Virginia, over a twelve-month period starting December 1961. The work was performed under Contract DA 44-177-TC-782, Task 9R38-01-017-29, "VTOL Downwash Impingement Problems". Messrs. W. Gordon Brady and Gary R. Ludwig of CAL conducted the study, and Mr. Robert R. Graham administered the project for USATRECOM.

The authors extend their appreciation to Messrs. C. Ryan, A. Sowyrda, and J. Nemeth of CAL for their significant contributions to the investigation.

TABLE OF CONTENTS

	<u>Page</u>
FOREWORD	iii
LIST OF ILLUSTRATIONS	vi
LIST OF SYMBOLS	ix
SUMMARY	1
CONCLUSIONS	3
RECOMMENDATIONS	4
I INTRODUCTION	5
II EXPERIMENTAL PROGRAM	7
III THEORETICAL ANALYSES	13
IV COMPARISON OF THEORY AND EXPERIMENT AND DISCUSSION OF RESULTS	24
V BIBLIOGRAPHY	32
APPENDIX I - DERIVATION OF EQUATIONS FOR INVISCID IMPINGING JET FLOW	35
APPENDIX II - CALCULATION OF GLAUERT'S FORM PARAMETER	44
DISTRIBUTION	106

LIST OF ILLUSTRATIONS

<u>Figure</u>		<u>Page</u>
1	Notation for Flow in Impinging Jet	46
2	View of Experimental Apparatus	47
3	View of Experimental Apparatus	48
4	Pattern of Static Pressure Taps on Ground Board	49
5	Boundary Layer Traverse Mechanism	50
6	Free-Jet Dynamic Pressure Profiles	51
7	Dynamic Pressure Profiles in Impinging Jet ($H/D = 4.0$) Compared With Free-Jet Profiles	52
8	Experimental Velocity Distributions at Nozzle Exit	53
9	Ground-Plane Static Pressure Distributions	54-58
10	Jet Centerline Static Pressure Distributions	59
11	Ground-Plane Velocity Distributions Computed From Experimental Pressure Distributions	60
12	Ground-Plane Boundary Layer Profiles - $H/D = 0.5$	61-63
13	Ground-Plane Boundary Layer Profiles - $H/D = 1.0$	64-66
14	Ground-Plane Boundary Layer Profiles - $H/D = 2.0$	67-69
15	Ground-Plane Boundary Layer Profiles - $H/D = 4.0$	70-72

<u>Figure</u>		<u>Page</u>
16	Velocity Profiles Near the Ground for $r/D > 1.0$, $U_{\infty} = 191$ fps	73-77
17	Boundary Layer Velocity Profiles for $r/D > 1.0$, $U_{\infty} = 191$ fps	78-82
18(a)	Velocity Profiles Near the Ground for $r/D > 1.0$, $H/D = 0.5$, $U_{\infty} = 121$ fps	83
18(b)	Boundary Layer Velocity Profiles for $r/D > 1.0$, $H/D = 0.50$, $U_{\infty} = 121$ fps	84
19	Flow Model for Circular Impinging Uniform Jet Used in References 8, 9, and 10	85
20	Radial Position of the Point of Neutral Stability in the Laminar Boundary Layer versus Nozzle Reynolds Number for Various Values of H/D	86
21	Universal Curve of Radial Mass Flow versus r/R	87
22	Variation of Experimental Maximum Local Velocity Near the Ground With r/D Compared With Theory for $U_{\infty} = 191$ fps	88-92
23	Variation of Experimental Values of $y_{1/2}/R$ With r/D Compared With Theory for $U_{\infty} = 191$ fps	93-97
24	Lines of Constant Dynamic Pressure in Mixing Region Surrounding the Potential Core of the Free Jet	98
25	Experimental Curve of Dynamic Pressure in the Mixing Region Surrounding the Potential Core of the Free Jet - $U_{\infty} = 121$ fps	99
26	Constant Velocity Contours in Mixing Region Surrounding the Potential Core of the Free Jet	100

<u>Figure</u>		<u>Page</u>
27	Comparison of Predicted and Experimental Ground-Plane Static Pressure Distributions - H/D = 1.0 to 2.0	101
28	Comparison of Predicted and Experimental Jet Centerline Static Pressure Distributions - H/D = 1.0 to 2.0	102
29	Representation of Vorticity Layer on Edge of Inviscid Jet	103
30	Flow Model Used in Present Analysis for Circular Impinging Uniform Jet	104
31	Variation of Glauert's Parameter α versus $u_m \delta_t / \nu$	105

LIST OF SYMBOLS

D	Diameter of jet nozzle at exit = 1 foot
H	Distance of jet nozzle exit from ground, foot
M_r	Radial momentum flux, slugs-ft. / (sec.) ²
P_A	Atmospheric pressure, psf.
P_P	Wind tunnel settling chamber pressure, psf.
P_S	Static pressure, psf.
P_T	Total pressure = $P_P - P_A$, psf.
Q_r	Radial mass flow, slugs/sec.
R	$D/2$
Re	Reynolds number
\bar{U}	Average velocity in nozzle = $\frac{2}{R^2} \int_0^R v r dr$, fps.
U_∞	Jet reference velocity = $\sqrt{2P_T/\rho}$, fps.
q	Dynamic pressure, psf.
r	Radial distance along ground board from stagnation point, foot
r_0	Location of r - coordinate of virtual origin for lines of constant dynamic pressure in free-jet flow (see Figure 24)
t	Distance from nozzle exit, positive toward ground-plane, foot
t_0	Location of t - coordinate of virtual origin for lines of constant dynamic pressure in free-jet flow (see Figure 24)
u	Local velocity parallel to ground plane, fps.
u_I	Local inviscid velocity, parallel to ground plane, fps. (see Figure 1)

u_m	Maximum value of u attained in the ground flow at any one radial station, fps. (see Figure 1)
v	Local velocity perpendicular to ground plane, fps.
y	Distance above ground board, foot
y_m	y at which $u = u_m$ (see Figure 1)
$y_{1/2}$	y at which $u = \frac{1}{2} u_m$ in outer ground flow region (see Figure 1)
z	Distance above ground board along jet centerline, foot
α	Form parameter associated with ground flow Reynolds number for radial wall-jet (see Reference 12)
ρ	Air density, slugs/ft. ³
δ^*	Boundary layer displacement thickness, foot
δ_t^*	$= y_m - y_{1/2}$, foot
ν	Kinematic viscosity, ft. ² /sec.
τ_0	Shear stress at the wall, psf.

SUMMARY

The purpose of the theoretical and experimental study reported herein was to investigate the flow characteristics of circular uniform jets impinging normally on a ground plane in order to further the understanding of the aerodynamic processes associated with ground particle entrainment in the impinging downwash of VTOL aircraft. Particular emphasis was placed on the flow properties in the ground-plane boundary layer where entrainment occurs. On the basis of the investigation that was conducted, the following general conclusions were drawn.

Experimental

The effect of the ground on the jet exit velocity profile for a circular uniform jet impinging normally on the ground is negligible for jet exits more than 1.5 to 2.0 nozzle diameters above the ground plane. For jet heights of more than 2.0 nozzle diameters above the ground plane, changes in the jet flow characteristics with height are primarily associated with the effects of viscous mixing.

Three distinct boundary layer regions occur in the ground-plane flow. A laminar boundary layer exists for $0 \leq r/D \leq 0.8$; a transition region of mixed turbulent and laminar boundary layer flow occurs for $0.8 \leq r/D \leq 2.0$; beyond $r/D = 2.0$ for values of the nozzle height-to-diameter ratio, H/D , less than or equal to 4, the ground flow is of the turbulent radial wall-jet type. Characteristics and extent of the transition boundary layer region vary with H/D . For the larger values of H/D , the transition to turbulent flow appears to be forced by interaction of the mixing region of the jet with the boundary layer. The start of the fully developed wall-jet flow occurs at values of r/D which decrease as H/D decreases.

Theoretical

Currently available methods of predicting the inviscid three-dimensional impinging jet flow suffer from the lack of an accurate method of predicting the shape and position of the free-stream surface. A plausible iterative technique is proposed for doing this, but numerical results using this technique have not yet been obtained. Calculations of ground-plane pressure distribution based on a jet boundary derived by Schach (Reference 8) for the infinite impinging jet and using the vortex sheet formulation for the jet developed during the present research resulted in relatively good agreement with experiment.

An approximate three-dimensional boundary layer analysis accurately predicts the laminar portion of the boundary layer, using experimentally derived pressure gradients, but fails to predict the experimental transition point at all H/D 's. This failure is apparently a result of the effect of the jet mixing region interacting with the boundary layer prior to natural transition for $H/D \geq 1.0$. Glauert's wall-jet theory is directly applicable to the ground-plane flow for the $r/D \geq 2.0$ for all H/D 's tested. A semiempirical method was developed for predicting boundary layer characteristics in the transition region. This method in conjunction with the Glauert theory allows prediction of velocities and boundary layer thickness to within about 10 percent of experimental values in the wall-jet flow regime of the ground flow.

CONCLUSIONS

On the basis of the results obtained, the following conclusions can be drawn regarding the experimental flow properties of uniform, circular, normal impinging jets, and regarding the theoretical analyses conducted:

1. The effect of the ground on the jet-exit velocity profile is negligible for jet exits more than one and one-half to two nozzle diameters above the ground plane.
2. Changes in the jet flow characteristics with jet nozzle height are primarily associated with the effects of viscous mixing for nozzle heights greater than two nozzle diameters above the ground plane.
3. For values of $H/D < 2$ the pressure distribution on the ground under a viscous impinging jet is essentially that obtained with an inviscid jet.
4. Transition from laminar to turbulent flow in the ground-plane boundary layer is considerably affected by interaction of the jet mixing region with the ground boundary layer.
5. The start of a radial wall-jet flow occurs at radial distances from the ground-plane stagnation point which decreases with decreasing jet nozzle height. For small nozzle-to-ground distances ($H/D \leq 2$), this decrease is primarily associated with the reduction in mean velocity in the nozzle as H/D decreases.
6. Approximate boundary layer analyses resulted in good to excellent agreement with experimental data, except in the small region between the radius where transition to turbulent flow occurs and the radius at which the velocity profiles first approach the form predicted by Glauert, for which region there is no applicable theory.

RECOMMENDATIONS

On the basis of the experimental results obtained and the analyses conducted, the following recommendations are made:

1. An experimental investigation of the jet flow characteristics and boundary layer flow characteristics should be made of a normally impinging nonuniform jet representative of the downwash of helicopter rotors and ducted fans.
2. Theoretical calculations of the flow field of the inviscid uniform impinging jet should be made for the range of jet nozzle height-to-diameter ratios of practical interest.
3. Experimental measurements should be made of the aerodynamic forces on objects in flows representative of the ground flows generated by jets, ducted fans, and rotors.

I INTRODUCTION

Of the many VTOL/STOL operational problems, one of the more serious is that of particle entrainment in jet or rotor downwash during near-ground hovering or slow-speed flight. Such entrainment can lead to loss of visibility for the pilot, loss of concealment for the aircraft, and damage to powerplant and structure. A considerable body of literature has grown over the past few years concerning various aspects of this problem. References 1, 2, and 3 are typical of the experimental studies of impinging downwash from jets, ducted fans and rotors; data have been obtained on both particle entrainment and the associated flow field.

Vidal, in Reference 4, reviewed the impinging-downwash, particle-entrainment problem from the point of view of available experimental data and theory in order to determine mechanisms for entrainment. A drag criterion for particle entrainment has been proposed (Reference 1), based on the drag required to start a particle moving while in contact with the ground. Particles are entrained in the flow by bouncing off projections on the ground. Vidal proposed, in addition, a lift criterion for entrainment, based on the lift required to pick up a particle clear of the ground. The lift on the particle is dependent on the velocity gradient in the ground boundary layer, as well as on the mean dynamic pressure of the flow at the particle. On the basis of the drag and lift criteria for entrainment, and using certain simplifying assumptions, Vidal showed qualitative agreement between calculated areas of particle entrainment under an impinging downwash and areas estimated from available experimental data. The relative importance of the two criteria depends primarily on the size of the particle compared to the boundary layer thickness.

A quantitative understanding of the entrainment mechanism may well lead to effective means of preventing or at least reducing the severity of the particle entrainment problem in impinging downwash flows. Inasmuch as entrainment occurs in the flow along the ground and as the boundary layer appears to play an important, if not dominant, part in this process, the need for accurate experimental data for the ground-flow boundary layer is apparent. Although there is a considerable body of experimental data for both impinging jets and rotor downwash flows, to the authors' knowledge there is none in which a detailed study of the boundary layer in the flow along the ground has been made. The experimental and theoretical results obtained from this and further research should provide the basis for the development of an accurate analytical technique for predicting areas under the impinging downwash of VTOL-type aircraft where ground particles can be entrained. It is believed that the development of effective and practical methods of preventing or at least alleviating the serious consequences of particle entrainment would be materially advanced thereby.

The research described in this paper was an experimental and analytical program to study the flow processes in a uniform impinging jet. Analytical methods for predicting the flow in such a jet, with particular emphasis on the boundary layer flow, were the primary aim. Experimental data on the flow in the uniform impinging jet and in the ground boundary layer are presented, as are the results of the theoretical studies obtained thus far.

II EXPERIMENTAL PROGRAM

Experimental Setup

The CAL-Air Force One-Foot High-Speed Wind Tunnel was used during the experimental research. The transonic-supersonic test section was completely removed. A 12-inch-diameter molded Fiberglas nozzle, designed to produce a uniform and parallel flow at the exit, was mounted to an adapter plate. The plate was attached to the test-section face of the wind tunnel settling chamber. The ground board was 8 feet x 8 feet square and could be set at varying distances from the jet nozzle. Figures 2 and 3 show the experimental setup. A pattern of static pressure taps was located in the ground board (Figure 4).

Velocities and static pressures in the jet were measured with a Pitot-static probe mounted on a traverse mechanism. Ground flow measurements were obtained from static and total head probes mounted in a second traverse mechanism so made that positioning of the probe relative to the ground board could be made with accuracy (Figure 5).

The ground-board static pressure lines were connected to an inclined manometer board. The boundary layer probes, of 0.014-inch outside diameter hypodermic tubing with a tip tapered to 0.009 inch, were attached to a small U-tube manometer mounted on the reverse side of the ground board. Pressure data from the larger jet flow Pitot-static probe were read either from a micromanometer or from the inclined manometer.

Experimental Results

Test data were obtained at five ground-board locations corresponding to nozzle height-to-nozzle diameter ratios, H/D of 4, 2, 1, 0.5, and 0.25.

Data were obtained for two mass flows corresponding to jet nozzle velocities of 121 ft. /sec. and 191 ft. /sec. At each H/D , velocity surveys were made at the jet nozzle and at various distances in the jet above the ground board. Static pressure distributions were measured along the jet centerline between the ground board and the jet nozzle and also along the ground board. Measurements of velocity in the flow along the ground were obtained at various radial distances from the stagnation point between $r = 6$ inches and $r = 48$ inches.

Dynamic pressure profiles, where dynamic pressure is normalized by the total pressure in the jet, are shown in Figure 6 for the jet exhausting into essentially free air. To obtain these data, the ground board was moved as far as possible from the nozzle ($H/D = 7.3$). The results shown are for $U_{\infty} = 121$ fps. There was no measurable difference between these profiles and corresponding data obtained for $U_{\infty} = 191$ fps. The figure shows that the mixing region surrounding the potential core of the jet grew in width with increasing nondimensional distance from the nozzle, t/D . The potential core vanished completely at $t/D \approx 4.7$.

Figure 7 shows the nondimensional dynamic pressure profiles in the jet obtained with the ground board set at $H/D = 4$. There was, again, no difference between profiles obtained with $U_{\infty} = 121$ and 191 fps. Free-jet dynamic pressure profiles corresponding to the same values of t/D are shown for comparison. Note that the two sets of data are identical for measurements made at distances greater than about two diameters from the ground ($z/D > 2$). Even at $z/D = 1.08$, the impinging jet corresponds closely to the free jet except in the vicinity of the jet centerline. Deceleration of the impinging flow near the jet centerline at small values of z/D is to be expected; the symmetry of the flow requires that there be a stagnation point at $r/D = z/D = 0$.

Figure 8 shows the velocity distributions at the nozzle for $H/D = 4, 2, 1, 0.5$ and 0.25 ; the velocities are normalized by the jet reference

velocity, U_{∞} . The velocity distribution for $H/D = 2.0$ was essentially identical to that for $H/D = 4.0$. The increasing effect of the ground board on the jet flow at the nozzle is quite evident in the $H/D = 1, 0.5$, and 0.25 velocity distributions. At $H/D = 1.0$ the velocity is no longer uniform and is reduced at the center of the nozzle to $0.96 U_{\infty}$. The velocity distribution is increasingly nonuniform for $H/D = 0.5$ and 0.25 ; at $H/D = 0.25$ the velocity at the center is down to $0.35 U_{\infty}$.

The static pressure distributions on the ground are presented in Figures 9(a) through 9(f) for the different values of H/D tested. Static pressures are here made nondimensional by the static pressure difference between the wind tunnel settling chamber and atmospheric pressure, which is equivalent to the total pressure in the jet. The data at each H/D for tests at $U_{\infty} = 191$ and 121 fps are nearly identical; hence, these pressure distributions are independent of mass flow. Although not all points are plotted, the data shown represent the maximum amount of scatter between measurements made along two perpendicular lines through the stagnation point and, also, between measurements made at six evenly spaced pressure taps on 6-inch and 12-inch radii centered on the stagnation point. The excellent symmetry of the flow in each case is demonstrated by the very small scatter.

Figure 10 shows static pressure distributions along the jet centerline. It can be seen that the data, up to $H/D = 2$, lie along one curve, at least up to z/D 's fairly close to the nozzle. The pressure distribution for $H/D = 4$ is somewhat below the curve. Static pressure is essentially the ambient pressure for $z/D \gtrsim 1.5$ at $H/D \gtrsim 2$. Note that pressure data were obtained a short distance inside the nozzle for $H/D = 0.25$ and $H/D = 0.50$.

Figure 11 shows nondimensionalized velocity distributions derived from the experimental static pressure distributions measured on the ground

board for various values of H/D . These velocity distributions were computed by assuming that there were no losses in the flow. The velocity distributions for $H/D = 1.0$ and 2.0 are identical within experimental error, while for $H/D = 0.5$ and 0.25 the distributions show the increasing effect of proximity of the nozzle to the ground.

Figures 12, 13, 14, and 15 present the boundary layer velocity profiles obtained at several radial stations between $r/D = 0.5$ and $r/D = 1.33$ for $H/D = 0.5, 1, 2$, and 4 , respectively. No measurements were made in this range of r/D for $H/D = 0.25$. The velocity has been divided by the maximum velocity in the flow above the boundary layer at each station. The height above the board has been nondimensionalized by the nozzle diameter and multiplied by the square root of the nozzle Reynolds number. Data for both $U_\infty = 191$ and $U_\infty = 121$ fps are included. Up to $r/D \approx 0.8$, in all cases, the boundary layers appear to be laminar, witness the shape of the profiles and the fact that data for both mass flows normalize to one curve with Reynolds number. The change in shape of the boundary layer velocity profiles between $r/D = 0.83$ and $r/D = 1.17$ suggests that transition to turbulent flow has occurred in the intervening region, although not necessarily at exactly the same radius for each value of H/D . Note the excellent repeatability demonstrated by the data of Figures 12(f) and 13(f) and the slightly poorer, although acceptable, repeatability of the data in Figures 14(f) and 15(f). The repeat data were obtained after the ground board had been moved and then repositioned to the H/D desired.

The differences between original and repeat data in Figures 14(f) and 15(f) can be attributed to a change in displacement effect of the boundary layer probe near the ground plane; for both cases these differences were of the order of 0.001 inch in terms of distance from the ground plane. Apparently, at the start of the tests, the boundary layer probe had an

inner coating of oil which, as the tests proceeded, collected lint and dust; as a result, about halfway through the tests, the probe became completely blocked. The probe was then cleaned out with alcohol and a fine wire, and tests were resumed. The tests which had been completed prior to the cleaning were those at $H/D = 4$ and $H/D = 2$. All data for $H/D = 1, 0.5$, and 0.25 , and all repeat data, were obtained after the cleaning. It is believed that the lint and dust were deposited asymmetrically on the inside of the probe in such a manner that the effective center of the opening in the probe was moved closer to the board than the geometric center. Consequently, the velocity profiles calculated from the data with the geometric center of the probe as a reference would necessarily be displaced away from the board. In confirmation, the theoretical laminar boundary layer profiles at $r/D = 0.5$ and 0.667 check quite well with the experiments for tests run after the probe was cleaned and are displaced below the experimental profiles by about the same amount as the difference between the original and repeat runs at $H/D = 4$ and 2 .

In Figures 16(a) through 16(e), u/u_m is plotted versus $y/y_{1/2}$ for the flow near the ground for $r/D \geq 1.17$ and $U_\infty = 191$ fps at all values of H/D tested; $y_{1/2}$ is the distance to the point outside the boundary layer at which $u = \frac{1}{2}u_m$ (see Figure 1). In general, the data falls essentially on a single curve for $1.33 \leq r/D \leq 4.0$. At $H/D = 4$, the lower limit becomes $1.67 \leq r/D$. The accuracy of measurements made at $r/D = 1.67$ is doubtful. To obtain the data at $r/D = 1.67$ required a modification of the traversing mechanism which decreased its rigidity.

In Figures 17(a) through 17(e), the boundary layer region for the data of Figures 16 is plotted on a greatly expanded scale. The comments made above apply here as well. Velocity profiles in this range of r/D were

also measured with $U_{\infty} = 121$ fps. The data obtained indicated that these profiles, when normalized as in Figures 16 and 17, are independent of U_{∞} , at least over the range tested. A typical set of data is presented for $U_{\infty} = 121$ fps and $H/D = 0.5$ in Figures 18(a) and 18(b). These figures can be compared with the corresponding profiles for $U_{\infty} = 191$ fps.

III THEORETICAL ANALYSES

Basic Approach

The classical approach to the theoretical analysis of boundary layers is first to compute the outer inviscid flow ignoring the effect of the boundary layer on that flow. The boundary layer is then computed assuming that the flow conditions on the outer edge of the boundary layer are those predicted at the surface by the inviscid flow analysis. This is basically the approach adopted in the theory reported in this paper. It is assumed that the effects of viscous mixing in the impinging jet flow do not materially affect the static pressure distribution on the ground plane. The boundary layer in the outer ground flow region, where the ground-plane static pressure is essentially zero and where viscous mixing is a basic part of the flow processes, is treated separately.

Uniform Inviscid Impinging Jet Theory

An inviscid jet in fluid otherwise at rest is in the class of free streamline flows. The essential difficulty in treating such flows analytically lies in the fact that even though there are well defined boundary conditions on the free streamlines in such flows, the location of the free streamline is not known in advance and must be determined as part of the solution.

There is a considerable body of literature concerning the theory of inviscid and viscous jet flows, as noted in Reference 5. Exact solutions for two-dimensional inviscid impinging jet flows using hodograph techniques have been obtained (References 6 and 7); but the available theoretical treatments of inviscid uniform three-dimensional impinging jets are

limited to approximate or numerical methods. Of these, the approaches of Schach (Reference 8), Leclerc (Reference 9), and Shen (Reference 10) are worthy of note because the flow model on which they based their analyses (Figure 19) is a good approximation to the infinite impinging jet, and they obtain results which are in reasonable qualitative agreement with available experimental data.

Schach (Reference 8) used an integral equation method developed by Trefftz and solved numerically for the jet boundary (BC in Figure 19) by successive approximations. A shape for the unknown boundary was assumed. On the basis of the known behavior of the velocity potential on the assumed free boundary BC (because of the boundary condition that the velocity is a constant) and the boundary conditions on AF and EF, it is possible to compute numerical values along the assumed boundary BC of a function which is zero if the boundary is the correct one for the flow. If this function is not zero, a new jet boundary was then assumed, and the process was repeated. The primary difficulty with this technique was that no rational basis was derived or shown for correcting the boundary shape. In Schach's analysis, the ratio $H/D = 1.5$ and $L = 2$ in Figure 19.

Leclerc's approach (Reference 9) is of particular interest. He used an electrolytic analog to experimentally determine the shape of the free streamline boundary. The internal flow was then computed numerically using relaxation techniques. If carefully done, one would expect the experimental analog results to be equivalent to an "exact" solution for the assumed model of the impinging jet.

Shen (Reference 10) obtained an approximate solution for the model of Figure 19, using spherical coordinates, by expanding the velocity potential $\phi(r, \theta)$ in series involving spherical harmonics. A finite number

of terms in the series is used; boundary conditions are not satisfied identically on the boundaries, but in an average or weighted sense. For example, along boundary BC in Figure 19, the boundary condition is $(\partial\varphi/\partial S)_{BC} = U_\infty$, where S is tangent to curve BC. Shen satisfies the condition

$$\int_{\theta_B}^{\theta_C} \left(\frac{\partial\varphi}{\partial S} \right)_{BC} w_i(\theta) d\theta = U_\infty \int_{\theta_B}^{\theta_C} w_i(\theta) d\theta$$

where w_i is a weighting function. If n terms in the series for φ are considered, there are n constants to be determined and, hence, n equations like the one above are required. As many equations are obtained as needed by considering different weighting functions, w_i . On boundary BC, only the condition that the tangential velocity equals U_∞ is used; for a given assumed boundary BC, the solution obtained is checked by computing the weighted velocity component normal to the boundary. If this condition is satisfied, within the limits of the method, the solution has been obtained. If this condition is not satisfied, a new boundary must be assumed and the process repeated. Shen indicates a possible iterative technique for obtaining the "exact" boundary for the flared jet which involves the solution of simultaneous nonlinear algebraic equations, but gives numerical results only for the successive approximations type of analysis.

All of the above authors used trial and error techniques to determine the free streamline boundaries of the impinging jet flow, although Shen does suggest a possible iterative technique. In addition, the effects on the jet flow of a ground plane in proximity to a jet exit cannot be determined from these approaches without modifications in the assumed model. As the jet exit approaches the ground plane, there is a back-pressure which is reflected at the exit in terms of reduced dynamic pressure in the center of the jet, and the jet exit velocity profile is no longer uniform (Figure 8).

The analysis of the inviscid impinging jet performed during the current research was motivated by a need for a theory which would account for the effect of the ground on the exit velocity distribution of a jet nozzle. A systematic iterative method to determine the free jet boundary was sought. A formulation of the inviscid jet flow has been derived in terms of a vortex sheet representation for the jet boundaries, and a plausible iterative technique was determined for deriving the free jet boundary. These are presented in Appendix I. An IBM 704 program has been written and is currently being checked out. At this writing, conclusive final results have not been obtained; however, the results so far obtained are encouraging. The method of analysis derived during this research may well be applicable to a much broader class of inviscid three-dimensional free-streamline flows than merely the uniform inviscid impinging jet.

Certain basic properties of the flow of an inviscid impinging uniform jet can be inferred without actually solving for the flow. Call \bar{U} the equivalent uniform velocity in the tube. At some distance along the ground plane from the stagnation point, where the pressure has fallen to near ambient pressure, $u_r \approx U_\infty$ for $0 < y < \gamma_s(r)$, where $\gamma_s(r)$ is the height of the free stream surface above the ground plane. Reich (Reference 11) showed experimentally that this is true for $r/D \geq 1.5$. Conservation of mass requires that

$$\pi \rho R^2 \bar{U} \approx 2\pi \rho r \gamma_s U_\infty$$

or

$$\gamma_s(r) \approx \frac{R^2 \bar{U}}{2r U_\infty} \quad (1)$$

Hence, for a given H/D (and, hence, \bar{U}/U_∞), γ_s varies hyperbolically with r . This fact was utilized by Schach and Shen (References 8 and 10) in their work, and Leclerc (Reference 9) used this result as part of a check on the accuracy of the results of his electrolytic analog experiment.

Boundary Layer Analysis

The boundary layer on the ground plane created by an impinging jet can be divided into two distinct regions separated by a transition zone. In the vicinity of the stagnation point, the boundary layer will be laminar and its properties will be determined by the static pressure distribution on the ground. At radial distances from the stagnation point sufficiently large to approximate a zero static pressure gradient at the ground, the flow will assume the form of a radial wall jet which has been analytically described by Glauert (Reference 12). In the following analysis, the two regions have been considered separately, and an assumption about the loss in momentum flux in the transition zone has been used to estimate the initial radius of the wall-jet flow and its properties at that radius.

Laminar Boundary Layer

An approximate method devised by Smith (Reference 13) was used to calculate the properties of the laminar boundary layer in the vicinity of the stagnation point. This method was selected because of its accurate prediction of velocity profiles in regions of accelerating flows, such as exist in the present application, and because of its simplicity. The experimental pressure distributions on the ground were used in these calculations for each H/D . The potential velocity distributions associated with the pressure distributions have been presented in Figure 11. Boundary layer velocity profiles predicted for various values of H/D are shown in Figures 12 through 15.

The location of transition from laminar to turbulent flow in the boundary layer was investigated by consideration of boundary layer stability theory. Two-dimensional stability criteria were applicable to this work (Reference 4). These criteria were used to determine the radius

for neutral stability of the laminar boundary layer, $(r/D)_{crit.}$, in the following manner. The critical Reynolds number, $\frac{u_m \delta^*}{\nu}$, was obtained from Reference 14 as a function of Pohlhausen's form parameter, Λ . A relation between Λ and the included wedge angle for flow over a wedge was taken from Reference 15. The equivalent wedge angle, u_m/U_∞ and δ^*/D had already been obtained as functions of r/D in the application of Smith's method, so these results were combined to calculate curves of nozzle Reynolds number $\frac{U_\infty D}{\nu}$ versus $(r/D)_{crit.}$. Figure 20 shows the final result of these calculations for various nozzle-to-ground distances.

In view of the large amount of turbulence in the mixing region of the impinging jet, the stable region in Figure 20 should be interpreted as an indication of the maximum radial distance that the boundary layer will remain laminar for a given nozzle Reynolds number. Also, because of the steepness of the curves in the region $r/D \leq 1$, it can be inferred that turbulence feeding into the laminar boundary layer at values of r/D only slightly less than $(r/D)_{crit.}$ will be highly damped. Hence, the curves should provide a relatively good criterion for estimating the radius of transition from laminar to turbulent boundary layer flow. This criterion should be especially accurate when $(r/D)_{crit.} < 1$.

Wall Jet

At values of $r/D \geq 2$, the pressure gradient along the ground was found to be essentially zero for all values of H/D tested. In this region, Glauert's analysis (Reference 12) of the radial wall jet should apply. The turbulent flow solution is the one of interest for the present investigation. The shape of the theoretical velocity profiles was prescribed by a parameter, α , which in turn depended weakly on the Reynolds number, $\frac{u_m \delta^*}{\nu}$, where u_m is the local peak velocity in the radial

wall flow and δ_t is the distance between the point at which $u = u_m$ and the point at which $u = \frac{1}{2}u_m$ (see Figure 1). A free constant, κ^* , was used to determine a quantitative relation between $\frac{u_m \delta_t}{\nu}$ and α . The value of κ was found to be 0.013 in Reference 16. This value of κ , rather than the value $\kappa = 0.012$ suggested by Glauert, was used in the current analysis.

It is desirable to obtain an estimate of α from the properties of the jet before impingement. Because of the weak dependence of α on $\frac{u_m \delta_t}{\nu}$, this can be accomplished with considerable accuracy even if some relatively broad assumptions are made. It was assumed that Glauert's theory applies at $r/D \approx 1.5$, that $u_m/U_\infty \approx 1$ at this radius, and that the loss in radial momentum flux due to the wall shear stress is negligible. On this basis $\alpha = 1.16$ for $0.50 \leq H/D \leq 4.0$ and $\alpha = 1.17$ for $H/D = 0.25$ are predicted. These values compare favorably with the value $\alpha = 1.16$ which was derived from the experimental measurements of $\frac{u_m \delta_t}{\nu}$ for $0.25 \leq H/D \leq 4.0$. A numerical example of this calculation is presented in Appendix II.

Once the shape of the velocity profiles in the wall-jet portion of the flow has been determined by α , the functional dependence of $y_{1/2}$ and u_m on r is given by

$$\frac{u_m}{U_\infty} = C_1 \left(\frac{r}{R} \right)^a, \quad \frac{y_{1/2}}{R} = C_2 \left(\frac{r}{R} \right)^b \quad (2)$$

where the exponents a and b depend on the value of α , and the constants C_1 and C_2 may be functions of H/D . The determination of C_1 and C_2 forms the remaining portion of the analysis.

As noted in Equation (1), the height of the free-stream surface of the inviscid impinging jet above the ground plane is, for $r/D \gg 1.5$,

$$y_s(r) = \frac{R^2}{2r} \left(\frac{U}{U_\infty} \right)$$

where
$$\bar{U} = \frac{2}{R^2} \int_0^R u r dr$$

in the nozzle.

The radial momentum flux M_r is given by

$$M_r = 2 \pi \rho r U_\infty^2 y_s(r) = \pi \rho R^2 U_\infty \bar{U} \quad (3)$$

provided that r/D is large enough so that the pressure gradient at the wall is approximately zero. This relation must necessarily be applicable to the direct impact of two equal viscous jets, where there is no mechanism for a loss in momentum flux, even though the mass flow may be greatly increased between the nozzle and the radial station in question. The jet impinging on the ground, on the other hand, will suffer a loss in momentum flux due to the presence of the wall shear stress, τ_0 . This loss can be calculated for the laminar portion of the boundary layer. With an assumption about the additional losses in the transition region, a momentum flux relation can be derived to obtain one equation for the proportionality constants in Equation (2). This relation will have the form of Equation (3) with a term added to account for losses due to the wall shear stress. It can be written

$$\frac{M_r + \Delta M_r}{\pi \rho R^2 U_\infty^2} \left(\frac{U_\infty}{\bar{U}} \right) = 1 \quad (4)$$

where M_r is the radial momentum flux at radius r and ΔM_r is the loss in radial momentum flux up to r .

An additional relation is required to obtain the two unknowns in Equation (2). This relation was obtained empirically. It was observed that experimentally the quantity $\frac{y_{1/2} u_m}{R U_\infty}$ is independent of the mass flow entrainment process occurring in the jet before impingement. This result suggested that the radial mass flow could be combined with \bar{U}/U_∞ to obtain a universal curve of radial mass flow, Q_r , versus r . Now the

radial momentum flux $M_r \sim u_m^2 y_{1/2} r$ and the mass flow $Q_r \sim u_m y_{1/2} r$. If ΔM_r is either negligible or roughly constant for all H/D's at the start of the wall-jet flow, then $\frac{u_m^2 y_{1/2}}{U_\infty^2 R} \sim \frac{\bar{U}}{U_\infty}$ and $\frac{u_m y_{1/2}}{U_\infty R}$ will be proportional to $(\bar{U}/U_\infty)^X$ where X is a constant. Hence, the quantity

$$\frac{Q_r}{\pi \rho R^2 U_\infty} \left(\frac{U_\infty}{\bar{U}} \right)^X$$

would be independent of H/D. The collapse of the experimental data with $X = 0.65$ is illustrated in Figure 21. This normalization appears to be quite satisfactory except, possibly, for the data obtained at H/D = 1.0. At values of $r/R \lesssim 4$, the pressure gradient is not zero, so that the wall-jet solution does not apply in this region.

The variation of Q_r with r is prescribed by the form parameter α . From Reference 12 the exponents a and b in Equation (2) are -1.075 and 1.008, respectively, for $\alpha = 1.16$. Hence, $Q_r \sim u_m y_{1/2} r \sim (r)^{0.933}$. The effect of varying nozzle size and U_∞ on the exponent should be negligible over quite a large range of these parameters because of the insensitivity of α to nozzle Reynolds number. The relation

$$\frac{Q_r}{\pi \rho U_\infty R^2} \left(\frac{U_\infty}{\bar{U}} \right)^{0.65} = 0.46 \left(\frac{r}{R} \right)^{0.933} \quad (5)$$

seems to give the best fit to the experimental data.

Equations (4) and (5) provide a means of finding the unknown constants C_1 and C_2 . The loss in momentum flux, ΔM_r , was estimated by assuming that the boundary layer is completely laminar up to the transition point predicted in Figure 20 and that the loss in momentum flux varies with r in accordance with Glauert's solution for the radial wall jet beyond this radius.

After computing* that

$$\frac{Q_r}{\pi \rho R^2 U_\infty} = 1.46 \frac{M_r}{\pi \rho R^2 U_\infty^2} \left(\frac{U_\infty}{u_m} \right)$$

in the wall jet for $\alpha = 1.16$, one can obtain

$$\frac{u_m}{U_\infty} \approx 3.18 \left[1 - \frac{\Delta M_{r_t}}{\pi \rho R^2 U_\infty \bar{U}} \right] \left(\frac{\bar{U}}{U_\infty} \right)^{0.35} \left(\frac{r_t}{R} \right)^{0.142} \left(\frac{r}{R} \right)^{-1.075}$$

where ΔM_{r_t} is the loss in momentum flux in the laminar boundary layer up to the predicted transition radius, r_t . Both of these quantities are available from the laminar boundary layer calculations. Hence,

$$C_1 = 3.18 \left[1 - \frac{\Delta M_{r_t}}{\pi \rho R^2 U_\infty \bar{U}} \right] \left(\frac{\bar{U}}{U_\infty} \right)^{0.35} \left(\frac{r_t}{R} \right)^{0.142} \quad (6)$$

Finally, since* $\frac{Q_r}{\pi \rho R^2 U_\infty} = 2.22 C_1 C_2 \left(\frac{r}{R} \right)^{0.933}$ for $\alpha = 1.16^*$, we have

$$C_2 = \frac{0.207}{C_1} \left(\frac{\bar{U}}{U_\infty} \right)^{0.65} \quad (7)$$

These relations for C_1 and C_2 were used in conjunction with Equation (2) to predict the variation of u_m/U_∞ and $y_{1/2}/R$ with r/R in the wall-jet region. The results are presented in Figures 22 and 23.

*The numerical constants in these equations and Equation 8 on the following page were obtained by integration of the theoretical velocity profiles. That is,

$$Q_r = 2\pi\rho r \int_0^\infty u dy = 2\pi\rho u_m y_{1/2} r \int_0^\infty \left(\frac{u}{u_m} \right) d\left(\frac{y}{y_{1/2}} \right)$$

$$\frac{Q_r}{\pi \rho R^2 U_\infty} = 2.22 \frac{u_m}{U_\infty} \frac{y_{1/2}}{R} \frac{r}{R}, \text{ where } 2 \int_0^\infty \left(\frac{u}{u_m} \right) d\left(\frac{y}{y_{1/2}} \right) = 2.22 \quad \alpha = 1.16$$

and

$$M_r = 2\pi\rho r \int_0^\infty u^2 dy = 2\pi\rho (u_m)^2 y_{1/2} r \int_0^\infty \left(\frac{u}{u_m} \right)^2 d\left(\frac{y}{y_{1/2}} \right)$$

$$\frac{M_r}{\pi \rho R^2 U_\infty^2} = 1.524 \left(\frac{u_m}{U_\infty} \right)^2 \left(\frac{y_{1/2}}{R} \right) \left(\frac{r}{R} \right), \text{ where } 2 \int_0^\infty \left(\frac{u}{u_m} \right)^2 d\left(\frac{y}{y_{1/2}} \right) = 1.524$$

$$\alpha = 1.16$$

Transition Zone

In the zone between the laminar boundary layer region and the wall-jet region, the ground flow was assumed to follow Glauert's velocity profile with the condition that $u_m/U_\infty = \text{constant} = \text{value of } u_m/U_\infty \text{ at predicted transition}$. This assumption and the one pertaining to the loss in momentum flux used in the wall-jet analysis allowed an estimation of $y_{1/2}/R$ in the transition zone. With $d = 1.16$, the result was

$$y_{1/2}/R \approx \frac{1}{1.524} \frac{U}{U_\infty} \left(1 - \frac{\Delta M_{rt}}{\pi \rho R^2 U U_\infty}\right) \left(\frac{r}{r_t}\right)^{-0.142} \left(\frac{U_\infty}{u_{mt}}\right) \left(\frac{r}{R}\right)^{-1} \quad (8)$$

where u_{mt} is the peak velocity at predicted transition ($0.98 \leq \frac{u_{mt}}{U_\infty} \leq 0.99$ for all values of H/D considered in the present work). The ground flow predicted in this manner cannot apply immediately downstream of the transition radius because a finite distance is required to establish some sort of equilibrium between the jet mixing zone and the ground boundary layer. It is plausible, however, that this distance may be considerably less than that required to establish a pure wall-jet flow. Hence, the above relation is proposed to bridge a portion of the gap between the wall-jet flow and the laminar boundary layer.

IV COMPARISON OF THEORY AND EXPERIMENT, AND DISCUSSION OF RESULTS

Free-Jet Flow

Points of constant dynamic pressure in the mixing region of the jet exhausting into free air are shown in Figure 24. These points were cross-plotted from the dynamic pressure profiles of Figure 6. The data appear to be well represented by straight lines radiating from a virtual origin, $t_0/D \approx -0.50$ and $r_0/D \approx 1.04$, except for stations very close to the nozzle exit. In the range of t/D where this radial straight line representation is applicable, the dynamic pressure distributions will be similar, that is, $q/(\frac{1}{2}\rho U_\infty^2)$ will be a unique function of $(r-r_0)/(t-t_0)$. As shown in Figure 25, the dynamic pressure distributions in the mixing region are at least approximately similar when plotted versus $(r-r_0)/(t-t_0)$, provided that the distance from the nozzle exit is greater than $t/D \approx 1$. The function

$$\left[e^{-56 \left(\frac{r-r_0}{t-t_0} + 0.097 \right)^2} \right]^2$$

provides an excellent empirical fit to the data. The velocity distribution is given simply by the square root of this function:

$$\frac{v}{U_\infty} = e^{-56 \left(\frac{r-r_0}{t-t_0} + 0.097 \right)^2}$$

where

$$\frac{r_0}{D} = 1.04, \quad \frac{t_0}{D} = -0.50 \quad \text{for} \quad \frac{t}{D} > 1.$$

Kueth (Reference 17) has derived theoretically the velocity distribution in the mixing region surrounding the core of an axially symmetric circular jet. The theoretical constant velocity curves are compared with the current data in Figure 26. The agreement between theory and

experiment is satisfactory except, possibly, near the outer edge of the mixing region where the velocity is almost zero. Velocity distributions derived from the theory should be more accurate than the above empirical formula in the region $0 \leq \frac{t}{D} \leq 1$, whereas the empirical expression provides a simple and probably quite accurate method of finding velocity distributions when $t/D > 1$.

Impinging Jet Flow

Although the theoretical analysis of the inviscid impinging jet has, as yet, not been completed, some calculations have been made. The results of calculations of ground-plane and jet-centerline pressure distributions based on the vortex sheet model of the present theory and using the curve for the free jet boundary computed by Schach are presented in Figures 27 and 28. The corresponding pressure distributions computed by Schach, Leclerc, and Shen (References 8, 9, and 10) and the experimental pressure distributions for $H/D = 1$ and 2 are shown for comparison.

At distances greater than some fixed height, say H_f , from the plane, the infinite inviscid jet impinging normally on a ground plane has essentially a constant diameter and uniform velocity distribution with the velocity equal to U_∞ , the free streamline velocity at the jet boundary. Hence, for a uniform inviscid jet issuing from a nozzle at height $\gg H_f$ above the ground plane, there would be no difference in the impinging flow from that of an infinite inviscid jet. Schach (Reference 18) found this H/D to be approximately 2 from experiments on water jets in air, which is consistent with the present results (Figure 10). For an actual jet of air into air at rest, viscous mixing occurs. For such a viscous jet, at H/D 's large enough that the jet is a fully developed turbulent jet prior to impingement, it is clear that all of

the impinging flow is influenced by the viscous mixing in the jet, and that the concept of an "infinite inviscid jet" no longer is relevant. For $H/D \ll 1.0$, it is reasonable to expect that, in the neighborhood of the stagnation point, the flow along the ground is not materially influenced by the mixing. Therefore, there must be some intermediate H/D at which the effect of the mixing in the jet prior to impingement is first felt in the flow along the ground plane, as reflected in the ground-plane pressure distribution near the stagnation point.

It is inferred from the present data and from the results obtained by Leclerc (Reference 9) that the effects of jet mixing on the pressure distribution on the ground are important only for $H/D > 2$. Since the velocity at the nozzle was uniform and equal to U_∞ for $H/D \gg 2$, the effect of the ground on the flow at the nozzle was negligible (Figure 8). Hence, any differences in the pressure distributions measured at values of $H/D > 2$ can only be due to mixing in the jet prior to impingement. The measured pressure distributions on the ground were identical for $H/D = 1$ and 2 (Figure 11), and agreed extremely well with the results obtained by Leclerc for an inviscid jet at essentially an infinite value of H/D (Figure 27). The pressure distribution obtained at $H/D = 4$, however, differed substantially from those measured at $H/D = 1$ and 2, even in the neighborhood of the stagnation point. There is a possibility that the effects of mixing and of ground proximity cancel each other for $1 \lesssim H/D \lesssim 2$ and, hence, lead to agreement with the inviscid results of Leclerc. However, since the effect of ground proximity is negligible at the nozzle for $H/D \gg 2$, with or without mixing (cf. previous paragraph), one must conclude that the effect of mixing in the jet is negligible for $H/D \lesssim 2$. It should be noted that the effects of mixing for $H/D = 4$ were evident in the vicinity of the stagnation point even though measurements showed that there was still a potential

core in the jet just prior to impingement. (Potential core diameter was approximately $0.35D$ at one nozzle diameter above the ground.)

Because mixing in the jet prior to impingement affects the ground pressure distribution for $H/D > 2$, it appears that theoretical solutions for the inviscid jet will be useful only for $H/D \leq 2$. Any theory for H/D much larger than 2 must, somehow, account for viscous mixing in the jet if it is to result in accurate predictions of the ground plane pressure distribution. The starting point for such a theory could be taken at two to three jet diameters above the ground, where the velocity profile was found to be identical to that of the corresponding free jet (cf. Section II and Figure 7).

Ground Flow

Comparisons between the theoretical laminar boundary layer profiles and experimental boundary layer profiles are presented in Figures 12 through 15 for $H/D = 0.5, 1, 2$, and 4. It is evident that the experimental results are predicted quite satisfactorily for $r/D \leq 0.7$, if allowance is made for the uncertainty in specifying the correction for the distance of the effective center of the probe from the ground. These "zero errors" have been discussed in Section II. As the radial distances increase above $r/D = 0.7$, the agreement between experiment and the laminar theory deteriorates progressively from the outer edge of the boundary layer inward. For the particular case presented in Figure 12 ($H/D = 0.5$), the calculated critical radius for transition of the boundary layer was $r/D = 1.08$ for $U_{\infty} = 191$ fps and $r/D = 1.17$ for $U_{\infty} = 121$ fps. This result suggests that in the subcritical range of r/D , the irregularities at the outer edge of the boundary layer are due to the diffusion of turbulence from the jet mixing region into the laminar boundary layer.

As r/D is increased, this turbulence is able to penetrate deeper into the boundary layer by virtue of the decreased stability until, at the critical radius, the boundary layer becomes completely turbulent. The diffusion process was more marked at the larger H/D 's, where the jet mixing region before impingement was wider and the rate of change of pressure gradient with r/D more gradual. In fact, at $H/D = 4$ (Figure 15), the boundary layer appeared to be almost completely turbulent at $r/D = 1.0$, whereas the calculated critical radii occurred at $r/D = 1.2$ and 1.36 for $U_\infty = 191$ and 121 fps, respectively.

The experimental velocity profiles of the flow near the ground for $r/D \geq 1.17$ are given in nondimensional form in Figures 16(a) through 16(e) along with the velocity profiles predicted by Glauert (Reference 12) for values of $\alpha = 1.1$ and 1.2 . If it is recalled that the appropriate value of α was found to be 1.16 , the agreement between theory and experiment can be seen to be generally very good for $1.33 \leq r/D \leq 4.0$, with the lower limit increasing to 1.67 at $H/D = 4$. In the range $y/y_k > 1.2$, the experimental data diverge from the theory. This deviation has been noted by other experimenters (References 16, 19) and is probably due to errors incurred by angularity of the flow with respect to the probe, or to the decreasing accuracy of the measurements at the very low velocities encountered.

The boundary layer region of Figure 16 is plotted in Figures 17(a) through 17(e). The theoretical profile for $\alpha = 1.16$ has been added to these figures. The theory again appears to give an excellent prediction of the flow for $r/D \geq 1.33$, except in the region very close to the wall. Near the wall the turbulent flow will undergo transition to what is generally referred to as the laminar sublayer. The outer edge of this transition region can be estimated from the criterion $(y\sqrt{\tau_0/\rho})/\nu > 70$ for purely turbulent flow (Reference 14). With the aid of Blasius'

formula for turbulent pipe flow, this becomes

$$\frac{y}{y_{\frac{1}{2}}} > \sqrt[3]{\frac{70\nu}{0.0225}} \left(\frac{u_m y_m}{\nu} \right)^{\frac{1}{6}} / (u_m y_{\frac{1}{2}})$$

for the region of completely turbulent flow in Figures 17(a) through 17(e). This expression is approximately equal to 0.015 for all values of H/D tested in the current work. Hence, the experimental data can be expected to diverge from that predicted by the wall-jet theory when $y/y_{\frac{1}{2}} < 0.015$. Accordingly, the theoretical profile for $\alpha = 1.16$ has been modified by matching the inner portion of the universal velocity distribution for smooth pipes (Figure 20.4 of Reference 14) to the theoretical curve at $y/y_{\frac{1}{2}} = 0.015$. The resulting curve now agrees with the experimental data even in the region where $y/y_{\frac{1}{2}}$ is small enough to make the flow primarily dependent on viscous stresses rather than Reynolds stresses.

The shape of the nondimensional velocity profiles has been shown in the previous paragraphs to be adequately predicted by theory. The adequacy of the analysis is also dependent on its accuracy in predicting u_m/U_{∞} and $y_{\frac{1}{2}}/R$ in the wall-jet region and on whether u_m is equal to u_I in the laminar region. The theoretical variation of u_m/U_{∞} with r/D for $U_{\infty} = 191$ fps is compared to its experimental equivalent in Figures 22(a) through 22(e). In the laminar region the assumption $u_m = u_I$ appears to be valid up to the predicted transition radius for $H/D = 0.5$ and 1.0 . At $H/D = 2$ and 4 , the experimental value of u_m begins to fall below u_I at radii less than that for predicted transition. This behavior is consistent with the appearance of an apparently forced transition of the laminar boundary layer at radii less than that for neutral stability. In the wall-jet region, u_m/U_{∞} was evaluated from Equations (2) and (6). The calculated curves of u_m/U_{∞} are, in general, about 10 percent higher than the experimental

data. Judging from these results, the assumption that the momentum flux variation with r has the same form throughout both the transition region and the wall-jet region may possibly be inadequate. However, the errors could also be due, in part, to the occurrence of the above-mentioned forced transition or to small differences between theory and experiment in the values of the exponents a and b in Equation (2). Recalculation of C_1 with $a = 1.143$ and $b = 1.028$ to conform with the experimental results provided estimates of C_1 which were, in general, considerably more accurate over the H/D range tested. The curves obtained with this modified analysis are also shown in Figures 22. The improved accuracy suggests that the discrepancy between the analysis and experiment is due primarily to small differences between predicted and actual values of a and b .

The variation of $y_{1/2}/R$ with r/D in the wall-jet region is shown in Figures 23(a) through 23(e). By virtue of the inverse relation between C_1 and C_2 in Equation (7), these predictions are too low by the same amount that u_m/U_∞ is too high. The improvement in the analysis obtained by using the experimental values of a and b is reflected here as well as in the calculation of u_m/U_∞ .

In deriving Equation (8) for the value of $y_{1/2}/R$ in the transition zone, it was assumed that Glauert's theoretical velocity profiles applied, even though the flow in this region does not actually conform to a true radial wall jet. Some insight as to the accuracy of this assumption can be obtained by inspection of the velocity profiles in Figures 16 and 17. At all values of H/D except 4, the profiles are accurately predicted for $r/D \geq 1.33$. At $H/D = 4$ the boundary layer region of the velocity profiles is predicted satisfactorily for $r/D \geq 1.33$ and the outer flow region is given quite well for $r/D \geq 1.67$. The value of u_m/U_∞

assumed for the transition region is shown for each H/D in Figures 22(a) through 22(e), and the resulting values of $y_{1/2}/R$ are shown in Figures 23(a) through 23(e). The over-all accuracy of the predictions in this region is comparable to that for the wall-jet flow provided that $r/D \geq 1.33$. The juncture between the theoretical transition and wall-jet regimes appears to give a reliable estimate of the radius at which the experimental data approach the equivalent of a true wall jet. The region between $r/D = 1.33$ and the transition radius cannot be analyzed by the method presented. Fortunately, this region appears to be very small.

V BIBLIOGRAPHY

1. Kuhn, R. E. , An Investigation to Determine Conditions Under Which Downwash from VTOL Aircraft Will Start Surface Erosion from Various Types of Terrain, NASA TN-D-56, 1959.
2. Morse, G. , VTOL Downwash Impingement Study Summary Report, U. S. Army Transportation Research Command, TCREC TR-61-37, August 1961.
3. Anon. , Exploratory Investigation of the Usefulness of Some Diffusor Systems in Alleviating Ground-Erosion Problems from the Downwash Impingement of VTOL Lifting Systems, Nationaal Lucht-en Ruimtevaartlaboratorium Report A. 1547, October 1961.
4. Vidal, R. J. , Aerodynamic Processes in the Downwash Impingement Problem, IAS Paper No. 62-36, January 1962.
5. Birkhoff, G. and Zarantonello, E. H. , Jets, Wakes and Cavities, Academic Press, Inc. , New York, 1957.
6. Milne-Thompson, L. M. , Theoretical Hydrodynamics, Second Edition, The MacMillan Company, New York, 1950, pp. 277-279, 489.
7. Strand, T. , "Inviscid-Incompressible-Flow Theory of Static Two-Dimensional Solid Jets in Proximity to the Ground", Journal of the Aerospace Sciences, Vol. 29, No. 2, February 1962, pp. 170-184.

8. Schach, W. , "Umlenking eines Kreisformigen Flussigkeitsstrahles an einer ebenen Platte Senkrecht zur Stromungsrichtung", ("Deflection of a Circular Fluid Jet by a Flat Plate Perpendicular to the Flow Direction"), Ingenieur-Archiv, Vol. VI, 1935, pp. 51-59.
9. LeClerc, A. , Deflection of a Liquid Jet by a Perpendicular Boundary, M. S. Thesis, State University of Iowa, 1948.
10. Shen, Y. C. , Theoretical Analysis of Jet-Ground Plane Interaction, IAS Paper No. 62-144, June 1962.
11. Reich, F. , Umlenkung eines freien Flussigkeitsstrahles an einer zur Stromungsrichtung senkrecht stehenden ebenen Platte (Deflection of a Free Fluid Jet by a Flat Plate Normal to the Flow), VDI-Forsch. Heft 290, 1929.
12. Glauert, M. B. , "The Wall Jet", Journal of Fluid Mechanics, Vol. 1, Pt. 6, December 1956, p. 625.
13. Smith, A. M. O. , "Rapid Laminar Boundary Layer Calculations by Piecewise Application of Similar Solutions", Journal of Aeronautical Sciences, Vol. 23, No. 10, October 1956.
14. Schlichting, H. , Boundary Layer Theory, Fourth Edition, McGraw-Hill Book Company, New York, 1960, pp. 414, 509.
15. Pretsch, J. , "The Stability of Two-Dimensional Laminar Flow With Pressure Drop and Pressure Rise", British Reports and Translations, No. 22, File No. B.I.G.S. -37

16. Bakke, P., "An Experimental Investigation of the Wall Jet", Journal of Fluid Mechanics, Vol. 2, Pt. 5, July 1957, p. 467.
17. Kuethe, A. M., "Investigations of the Turbulent Mixing Regions Formed by Jets", Journal of Applied Mechanics, Vol. 2, 1935, pp. A-87 - A-95.
18. Schach, W., "Umlenkung eines freien Flüssigkeitsstrahles an einer ebenen Platte" ("Deflection of a Free Fluid Jet by a Flat Plate"), Ingenieur-Archiv, Vol. V, 1934, pp. 245-265.
19. Bradshaw, B. A. and Love, E. M., "The Normal Impingement of a Circular Air Jet on a Flat Surface", Aeronautical Research Council, Reports and Memoranda, R & M No. 3205, 1961.

APPENDIX I
DERIVATION OF EQUATIONS FOR INVISCID IMPINGING JET FLOW

Basic Formulation

Consider a Cartesian coordinate system with the z-axis directed along the axis of symmetry of the flow, positive vertically up from the ground plane, and the x-y plane ($z = 0$) coincident with the ground plane. Consider an element of volume $d\tau(x', y', z')$ with vorticity vector $\bar{\xi}(x', y', z')$. For vorticity distributed throughout a given volume V , one can write the vector velocity, \bar{q} , at any point (x, y, z) in the fluid as (Reference 6)

$$\bar{q}(x, y, z) = \frac{1}{4\pi} \int_V \frac{\bar{\xi}(x', y', z') \times \bar{d}}{|\bar{d}|^3} d\tau(x', y', z') \quad (I-1)$$

where

$$\bar{d} = (x - x')\hat{i} + (y - y')\hat{j} + (z - z')\hat{k}$$

and $\hat{i}, \hat{j}, \hat{k}$ are unit vectors in the x, y, and z directions, respectively. In the case of axially symmetric flow,

$$\bar{\xi} = \xi_x \hat{i} + \xi_y \hat{j}$$

The transformation to cylindrical coordinates (r, z, θ) , where

$$x = r \cos \theta, \quad y = r \sin \theta$$

and

$$\xi_x = \xi_0 \sin \theta, \quad \xi_y = -\xi_0 \cos \theta$$

gives

$$\bar{\xi} \times \bar{d} = \xi_0 [-\hat{i}_r (z - z') \cos \theta - \hat{j}_\theta (z - z') \cos \theta + \hat{k}_z (r \cos \theta - r')]$$

and

$$|\bar{d}|^3 = [(z - z')^2 + r^2 + (r')^2 - 2rr' \cos \theta']^{3/2}$$

where $\hat{i}_r, \hat{j}_\theta$ and \hat{k}_z are unit vectors in the r , θ and z directions, respectively. Because of axial symmetry, only the $\theta = 0$ plane need be considered.

Substituting in Equation (I-1) and equating vector components, we have

$$\begin{aligned} u &= - \frac{1}{4\pi} \int_V \frac{\zeta_0(r', z') (z - z') \cos \theta' d\tau(r', z', \theta')}{[(z - z')^2 + r^2 + (r')^2 - 2rr' \cos \theta']^{3/2}} \\ v &= \frac{1}{4\pi} \int_V \frac{\zeta_0(r', z') (r \cos \theta' - r') d\tau(r', z', \theta')}{[(z - z')^2 + r^2 + (r')^2 - 2rr' \cos \theta']^{3/2}} \\ v_\theta &= 0 \end{aligned} \quad (I-2)$$

where u , v are the velocity components parallel to the r -axis and the z -axis, respectively, and v_θ is the velocity component perpendicular to the meridian plane. The integration is taken over the volume V which includes all the distributed vorticity of intensity $\zeta_0(r, z)$.

Consider now the vorticity distributed in a thin layer on the edge of the jet. Consider a given element of volume, $d\tau$, of this layer (Figure 29) whose projection on the meridian plane is ϵdS , where ϵ is the infinitesimal thickness of the layer and dS is the length of the element along the curve $r = r_0(z)$ which defines the edge of the jet. From Stoke's Theorem (Reference 6, page 46) for a circuit C in the meridian plane enclosing the projection of $d\tau$, we have

$$\int_{S'} \bar{n} \cdot \bar{\zeta} dA = \int_C \bar{q} \cdot d\bar{s}$$

where \bar{n} is the unit outward normal vector to the surface enclosed by C , S' is the area enclosed by C , and \bar{q} is the velocity vector around C . The integral on the right-hand side is taken in the clockwise direction. Then

$$\begin{aligned} \int_{S'} \bar{n} \cdot \bar{\zeta} dA &= \zeta_0 \epsilon dS \\ \int_C \bar{q} \cdot d\bar{s} &= (q_1 - q_2) ds \end{aligned}$$

hence,

$$\zeta_0 \epsilon = q_1 - q_2$$

where q_1 and q_2 are as shown in Figure 29. If we let $\epsilon \rightarrow 0$, $\zeta_0 \rightarrow \infty$ such that

$$\zeta_0 \epsilon = \xi, \text{ a constant}$$

then

$$\xi = q_1 - q_2$$

Also,

$$\begin{aligned} \zeta_0 d\tau &= \zeta_0 \epsilon r_0 ds d\theta' \\ &= \xi r_0(z') \sqrt{1 + \left[\frac{dr_0(z')}{dz} \right]^2} dz' d\theta' \end{aligned}$$

Thus, Equation (I-2) can be written

$$\begin{aligned} u(r, z) &= \frac{1}{4\pi} \int_S \frac{\xi(r') r_0(z') \sqrt{1 + \left[\frac{dr_0(z')}{dz} \right]^2} (z - z') \cos \theta' dz' d\theta'}{[(z - z')^2 + r^2 + [r_0(z')]^2 - 2 r r_0(z') \cos \theta']^{3/2}} \\ v(r, z) &= \frac{1}{4\pi} \int_S \frac{\xi(z') r_0(z') \sqrt{1 + \left[\frac{dr_0(z')}{dz} \right]^2} [r \cos \theta' - r_0(z')] dz' d\theta'}{[(z - z')^2 + r^2 + [r_0(z')]^2 - 2 r r_0(z') \cos \theta']^{3/2}} \end{aligned} \quad (\text{I-3})$$

where the integration is carried out over the entire vortex sheet S .

The Boundary Conditions for Infinite Impinging Jet

The boundary conditions on the inviscid impinging jet flow are: along the surface $z = 0$, $v = 0$; along the jet boundary which is a free streamline, the velocity is equal to a constant and, therefore, ξ is also constant, as just outside the jet the velocity is zero.

To satisfy the boundary condition that $v = 0$ for $z = 0$, the plane $z = 0$ is made a plane of symmetry for the impinging jet and its image. Hence, the integration over S , Equation (I-3), must be carried out over two

vortex sheets, that defining the imping jet and that for the image jet.

The Boundary Conditions for Jet Nozzle at Finite Height Above the Ground

The jet is assumed to issue from a straight tube of constant diameter (Figure 30) at finite height, H , above the ground. A free-stream surface issues from the edge of the jet exit, B in Figure 30, such that the free streamline velocity vector at B is parallel to the side of the tube. The flow inside the tube along the side of the tube must be tangential to the side; but, of course, the streamline along this side is no longer a free streamline, as a pressure difference can exist and, hence, the magnitude of the edge velocity may vary. The boundary condition along the edge of the tube is, then, that the normal component of velocity, u , is zero. In addition, at B in Figure 30, v is continuous. Again, along the free streamline BC, the velocity and, hence, ξ are constant.

Final Form for Velocity Components

Figure 30 illustrates the flow model as thus far developed. The straight tube of constant diameter, D , centered on the z -axis extends from $x = H$ to $z = \infty$. For $0 < z < H$, the curve $r = r_0(z)$ defines the edge of the jet. To insure that v is tangential at B in Figure 30, we require that $\frac{dr_0}{dz} = 0$ at $z = H$; that is, there is no discontinuity in slope between the side of the nozzle and the free-stream surface. The sides of the tube and the jet are represented by a vortex sheet of vorticity $\bar{\xi}(r_0, z)$ per unit area whose r - and z -components are zero. The image of this vortex system for $0 > z > -\infty$ assures that the boundary condition for no normal flow across OD is satisfied.

The integrations with respect to θ' can be done in closed form in each of the integrals of Equation (I-3). If we let $z = \bar{z}R$, $z' = \bar{z}'R$, $r = \bar{r}R$, $r_0 = \bar{r}_0R$ and $\xi = \bar{\xi} \xi(H)$, there results

$$\begin{aligned}
 u(\bar{r}, \bar{z}) = & -\frac{\xi(H)}{2\pi\bar{r}} \left\{ \int_{\frac{H}{R}}^{\infty} \frac{\bar{\xi}(\bar{z}')(\bar{z}-\bar{z}')}{\sqrt{(\bar{z}-\bar{z}')^2 + (\bar{r}+1)^2}} \left[\frac{(\bar{z}-\bar{z}')^2 + \bar{r}^2 + 1}{(\bar{z}-\bar{z}')^2 + (\bar{r}-1)^2} E(k_1) - K(k_1) \right] d\bar{z}' \right. \\
 & - \int_{\frac{H}{R}}^{\infty} \frac{\bar{\xi}(\bar{z}')(\bar{z}+\bar{z}')}{\sqrt{(\bar{z}+\bar{z}')^2 + (\bar{r}+1)^2}} \left[\frac{(\bar{z}+\bar{z}')^2 + \bar{r}^2 + 1}{(\bar{z}+\bar{z}')^2 + (\bar{r}-1)^2} E(k_2) - K(k_2) \right] d\bar{z}' \\
 & + \int_0^{\frac{H}{R}} \frac{[\bar{z}-\bar{z}'] \sqrt{1 + \left[\frac{d\bar{r}_0(\bar{z}')}{d\bar{z}} \right]^2}}{\sqrt{(\bar{z}-\bar{z}')^2 + [\bar{r} + \bar{r}_0(\bar{z}')]^2}} \left\{ \frac{[\bar{z}-\bar{z}]^2 + \bar{r}^2 + [\bar{r}_0(\bar{z}')]^2}{[\bar{z}-\bar{z}]^2 + [\bar{r} - \bar{r}_0(\bar{z}')]^2} E(k_3) - K(k_3) \right\} d\bar{z}' \\
 & \left. + \int_0^{\frac{H}{R}} \frac{[\bar{z}+\bar{z}'] \sqrt{1 + \left[\frac{d\bar{r}_0(\bar{z}')}{d\bar{z}} \right]^2}}{\sqrt{(\bar{z}+\bar{z}')^2 + [\bar{r} + \bar{r}_0(\bar{z}')]^2}} \left\{ \frac{[\bar{z}+\bar{z}]^2 + \bar{r}^2 + [\bar{r}_0(\bar{z}')]^2}{[\bar{z}+\bar{z}]^2 + [\bar{r} - \bar{r}_0(\bar{z}')]^2} E(k_4) - K(k_4) \right\} d\bar{z}' \right\} \\
 v(\bar{r}, \bar{z}) = & \frac{\xi(H)}{2\pi} \left\{ \int_{\frac{H}{R}}^{\infty} \frac{\bar{\xi}(\bar{z}')}{\sqrt{(\bar{z}-\bar{z}')^2 + (\bar{r}+1)^2}} \left[\frac{(\bar{z}-\bar{z}')^2 + \bar{r}^2 - 1}{(\bar{z}-\bar{z}')^2 + (\bar{r}-1)^2} E(k_1) - K(k_1) \right] d\bar{z}' \right. \\
 & - \int_{\frac{H}{R}}^{\infty} \frac{\bar{\xi}(\bar{z}')}{\sqrt{(\bar{z}+\bar{z}')^2 + (\bar{r}+1)^2}} \left[\frac{(\bar{z}+\bar{z}')^2 + \bar{r}^2 - 1}{(\bar{z}+\bar{z}')^2 + (\bar{r}-1)^2} E(k_2) - K(k_2) \right] d\bar{z}' \\
 & + \int_0^{\frac{H}{R}} \frac{\sqrt{1 + \left[\frac{d\bar{r}_0(\bar{z}')}{d\bar{z}} \right]^2}}{\sqrt{(\bar{z}-\bar{z}')^2 + [\bar{r} + \bar{r}_0(\bar{z}')]^2}} \left[\frac{(\bar{z}-\bar{z}')^2 + \bar{r}^2 - [\bar{r}_0(\bar{z}')]^2}{(\bar{z}-\bar{z}')^2 + [\bar{r} - \bar{r}_0(\bar{z}')]^2} E(k_3) - K(k_3) \right] d\bar{z}' \\
 & - \int_0^{\frac{H}{R}} \frac{\sqrt{1 + \left[\frac{d\bar{r}_0(\bar{z}')}{d\bar{z}} \right]^2}}{\sqrt{(\bar{z}+\bar{z}')^2 + [\bar{r} + \bar{r}_0(\bar{z}')]^2}} \left[\frac{(\bar{z}+\bar{z}')^2 + \bar{r}^2 - [\bar{r}_0(\bar{z}')]^2}{(\bar{z}+\bar{z}')^2 + [\bar{r} - \bar{r}_0(\bar{z}')]^2} E(k_4) - K(k_4) \right] d\bar{z}' \left. \right\}
 \end{aligned}$$

where $K(k)$ is the complete elliptic integral of the first kind, and $E(k)$ is the complete elliptic integral of the second kind, with modulus k ; also,

$$(k_1)^2 = \frac{4\bar{r}}{(\bar{z} - \bar{z}')^2 + (\bar{r} + 1)^2}, \quad (k_2)^2 = \frac{4\bar{r}}{(\bar{z} + \bar{z}')^2 + (\bar{r} + 1)^2}$$

$$(k_3)^2 = \frac{4\bar{r}\bar{r}_0(\bar{z}')}{(\bar{z} - \bar{z}')^2 + [\bar{r} + \bar{r}_0(\bar{z}')]^2}, \quad (k_4)^2 = \frac{4\bar{r}\bar{r}_0(\bar{z})}{(\bar{z} - \bar{z}')^2 + [\bar{r} + \bar{r}_0(\bar{z}')]^2}$$

These integrals are valid everywhere except on the boundaries, at $(1, \bar{z})$ for $\bar{z} \gg \frac{H}{R}$ and $(\bar{r}_0(\bar{z}), \bar{z})$ for $\bar{z} \leq \frac{H}{R}$, where the integrands are singular. However, even on the boundaries, it can be shown that the Cauchy principal values of these integrals exist.

Equations (I-4) enable the velocity at any point in the flow to be computed, once the form of $\bar{r}_0(\bar{z})$, the curve defining the boundary of the jet, and $\bar{\xi}(\bar{z})$, the vorticity area density of the vortex sheet on the boundary of the jet and the tube, are known.

Equations (I-4) with the associated boundary conditions

$$\lim_{\bar{r} \rightarrow 1} u(\bar{r}, \bar{z}) = 0, \quad \bar{z} \gg H/R, \quad \bar{r} < 1$$

$$\lim_{\bar{r} \rightarrow \bar{r}_0} \frac{u(\bar{r}, \bar{z})}{v(\bar{r}, \bar{z})} = \frac{d\bar{r}_0(\bar{z})}{d\bar{z}}, \quad \bar{z} \leq H/R, \quad \bar{r} < \bar{r}_0$$

give rise to simultaneous nonlinear integral equations for $\bar{\xi}(\bar{z})$ and $\bar{r}_0(\bar{z})$, which, as they stand, do not admit of solution in closed form. However, by means of a high-speed large-capacity digital computer, a solution may be possible if a convergent iterative process can be derived which will permit the determination of the jet boundary $\bar{r}_0(\bar{z})$. What appears to be a rational process for doing this has been derived and programmed on the IBM 704 computer. However, the results obtained as yet are not conclusive because of difficulties with the program. Therefore, only a brief outline of the computational process is presented here.

The general computational procedure adopted is as follows:

1. The initial shape of the free streamline boundary is assumed.
2. The boundary condition that the flow at the wall of the tube is parallel to the tube is used to determine the varying area vorticity density of the vortex sheet representing the tube and the constant area vorticity density of the free-stream surface vortex sheet.
3. The flow normal to the free-stream surface is then evaluated; if there is a velocity normal to the boundary assumed for the free-stream surface, that assumed boundary is incorrect and must be adjusted.
4. The iteration proceeds for the adjusted boundary (by going back to Step 1).

The process of determining the revised jet boundary in Step 3 is based on the boundary condition along the jet boundary free streamlines, that the velocity normal to the boundary is zero. For example, if the computed velocity normal to the jet boundary is directed outward, this intuitively would suggest that the assumed boundary should be displaced outward. Let the curve for the assumed free jet boundary BC (Figure 30) for the i^{th} repetition of Steps 1 through 3 be

$$(\bar{r}_0)_i = [\bar{r}_0(\bar{z})]_i$$

Once the distribution of the vorticity in the vortex sheet is known from Step 2, above, it is possible to compute the velocity vector anywhere in the flow, based on $(\bar{r}_0)_i$, the assumed free-stream surface boundary

using Equations (I-4). The velocity components $u(\bar{r}_0, \bar{z})$, $v(\bar{r}_0, \bar{z})$ at the boundary are computed; then $[u(\bar{r}_0, \bar{z})/v(\bar{r}_0, \bar{z})]$ is the slope of the velocity vector along the i^{th} assumed boundary. If this slope is equal to $d(\bar{r}_0)_i/d\bar{z}$ all along the assumed boundary, $(\bar{r}_0)_i$ is the correct curve, as all boundary conditions are then satisfied. If not, two possible approaches for deriving a revised boundary are as follows:

1. As
$$\bar{r}_0(\bar{z}) = 1 - \int_{\frac{H}{R}}^{\bar{z}} \frac{d\bar{r}_0(\bar{z}')}{d\bar{z}}, \quad 0 < \bar{z} < \frac{H}{R}$$

a new boundary $(\bar{r}_0)_{i+1}$ can be obtained from

$$[\bar{r}_0(\bar{z})]_{i+1} = [\bar{r}_0(\bar{z})]_i - K_1 \int_{\frac{H}{R}}^{\bar{z}} \left[\frac{u(\bar{r}_{0i}, \bar{z})}{v(\bar{r}_{0i}, \bar{z})} - \frac{d[\bar{r}_0(\bar{z}')_i]}{d\bar{z}} \right] d\bar{z}' \quad (\text{I-5})$$

where K_1 is a constant. The slope of $[\bar{r}_0(\bar{z})]_{i+1}$ is then

$$\frac{d[\bar{r}_0(\bar{z})]_{i+1}}{d\bar{z}} = (1-K_1) \frac{d[\bar{r}_0(\bar{z})]_i}{d\bar{z}} + K_1 \frac{u(\bar{r}_{0i}, \bar{z})}{v(\bar{r}_{0i}, \bar{z})}$$

2. More simply, we could let

$$[\bar{r}_0(\bar{z})]_{i+1} = [\bar{r}_0(\bar{z})]_i - K_2 \left\{ \frac{u(\bar{r}_{0i}, \bar{z})}{v(\bar{r}_{0i}, \bar{z})} - \frac{d[\bar{r}_0(\bar{z})_i]}{d\bar{z}} \right\}, \quad (\text{I-6})$$

where K_2 is a constant.

Either approach (1 or 2), hopefully, provides a rational basis for an iterative technique. It should be noted that no theoretical rigor is claimed for this procedure; it is primarily a systemization of the method which a computer might use to adjust boundaries in a successive approximation technique. It is obviously intended for use in an electronic digital computer program. Convergence can, thus far, be determined only by a trial and error process. Several iterations would be made with a selected value of either of the constants K_1 or K_2 depending on which method is used. If the successive boundaries appear to be

diverging, then successively smaller values of K_1 or K_2 would be used until convergence is obtained.

Method 1, above, (Equation I-5) for deriving successive jet boundaries was incorporated in the IBM 704 program with the constant $K_1 = 1.0$. In this program, the distribution of vorticity density ξ is determined, for a given assumed free jet boundary, by a collocation procedure. At specified points on the tube (boundary AB in Figure 30), the velocity normal to the tube is computed in terms of ξ and set equal to zero. There results a set of linear equations in terms of $\xi(z)$. As a check on the integration accuracy, the velocity at the free jet boundary is computed, once convergence is obtained, to determine whether it is, in fact, equal to U_∞ .

As noted in the body of this report, calculations of velocities along the jet centerline and along the ground plane have been made using as an assumed curve for the jet boundary, one derived by Schach (Reference 8) by a successive approximations technique. As this boundary corresponds essentially to that for the infinite impinging jet, the corresponding vorticity area density on the vortex sheet should be constant, and this was assumed. The ground plane static pressures and jet centerline static pressures resulting from this calculation are shown in Figures 27 and 28 and are in relatively good agreement with experimental pressures for $H/D = 2$. The agreement is better, generally, than Schach's computed pressures. The difference between the present results and those of Schach, based on the same boundary, are probably a result of the more accurate numerical integration which can be obtained on a large digital computer.

Preliminary calculations obtained during partial runs of the complete program are encouraging and offer hope that, in fact, the process will converge. It is expected that eventually calculations of the inviscid impinging jet flow will be obtained for a range of values of H/D .

APPENDIX II

CALCULATION OF GLAUERT'S FORM PARAMETER, α

The value of the shape parameter α as a function of the Reynolds number $u_m \delta_t / \nu$ is shown in Figure 31. This curve was calculated from the data presented in Table 1 of Reference 12. for $K = 0.013$. It is evident that α depends only weakly on $u_m \delta_t / \nu$. Thus, only a rough estimate of the Reynolds number is required if α is to be determined with satisfactory accuracy; an error of ± 0.02 in α will lead to negligible differences in the predicted characteristics of the flow at the ground.

It has been generally observed that the flow on the ground under an impinging jet reaches a maximum velocity at $1 \lesssim r/D \lesssim 2$ and that this maximum velocity is approximately equal to that corresponding to the total pressure in the jet before impingement. With these observations as a guide, it was assumed that $u_m/U_\infty = 1$ at $r/D = 1.5$, that Glauert's theory applies at this radius, and that the loss in momentum flux due to the wall shear stress is negligible up to this radius.

The radial momentum flux in wall-jet flows is given by

$$\frac{M_r}{\pi \rho R^2 U_\infty^2} = \text{Const.} \left(\frac{u_m}{U_\infty} \right)^2 \frac{y_{1/2}}{R} \frac{r}{R}.$$

The constant is equal to 1.514 at $\alpha = 1.0$ and increases gradually to 1.547 at $\alpha = 1.6$. Since this range of α is the one most likely to be encountered in practice, an average value of the constant, equal to 1.53, represents a very good compromise. Hence,

$$\frac{M_r}{\pi \rho R^2 U_\infty^2} \approx 1.53 \left(\frac{u_m}{U_\infty} \right)^2 \frac{y_{1/2}}{R} \frac{r}{R}$$

and from Equation (4) in the body of this report

$$\frac{M_r}{\pi \rho R^2 U_\infty^2} = \frac{\bar{U}}{U_\infty} \quad \text{if losses are neglected.}$$

Combining these two equations and putting $\frac{u_m}{U_\infty} = 1$ at $r/D = 1.5$ gives

$$\frac{u_m y_{1/2}}{U_\infty R} \approx \frac{1}{1.53} \frac{\bar{U}}{U_\infty} \left(\frac{1}{2} \right) \left(\frac{1}{1.5} \right)$$

or

$$\frac{u_m \delta_t}{\nu} = \frac{u_m y_{1/2}}{\nu} \left(\frac{\delta_t}{y_{1/2}} \right) \approx \frac{1}{9.18} \left(\frac{\bar{U}}{U_\infty} \right) \left(\frac{U_\infty D}{\nu} \right) \left(\frac{\delta_t}{y_{1/2}} \right) \quad (\text{II-1})$$

A first approximation, $(\alpha)_1$, to the required value of α is obtained by choosing $\delta_t/y_{1/2} = 1$ and using Equation (II-1) to find $\left(\frac{u_m \delta_t}{\nu} \right)_1 = \frac{u_m y_{1/2}}{\nu}$ and, hence, $(\alpha)_1$ from Figure 31. For example, in the current tests, at $H/D = 0.5$ and $U_\infty = 191$ fps, $\frac{U_\infty D}{\nu}$ equalled 1.22×10^6 and \bar{U}/U_∞ was 0.84. This gave $\left(\frac{u_m \delta_t}{\nu} \right)_1 = 1.12 \times 10^5$, which corresponds to $\alpha = 1.16$. At this value of $(\alpha)_1$, $\delta_t/y_{1/2} \approx 0.9$ and a second approximation using $\left(\frac{u_m \delta_t}{\nu} \right)_2 = 0.9 \left(\frac{u_m y_{1/2}}{\nu} \right)$ can be performed. The result, $(\alpha)_2 = 1.16$, is the same as that for $(\alpha)_1$. At very much lower Reynolds numbers, the second approximation will be slightly higher than the first.

At very large values of H/D , the jet just prior to impingement will be fully turbulent. In this case, effective values for nozzle radius and U_∞ should be used. The effective radius could be defined by the radius of a free jet, at a distance from the nozzle equal to H , for which the velocity equals $\frac{1}{2}$ the centerline velocity. The reference velocity U_∞ would be taken as the free jet centerline velocity at this same distance.

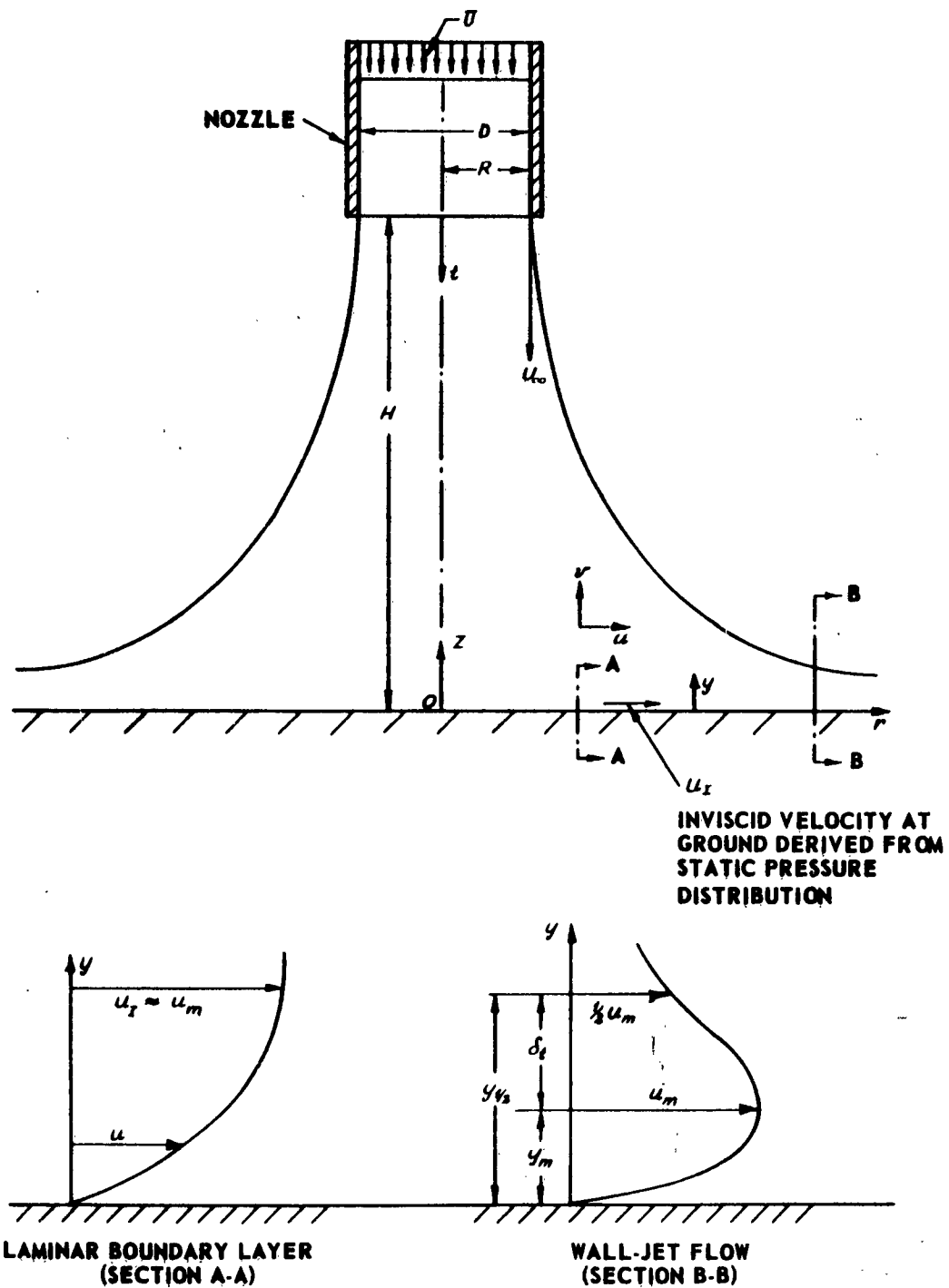


Figure 1. NOTATION FOR FLOW IN IMPINGING JET



Figure 2. VIEW OF EXPERIMENTAL APPARATUS

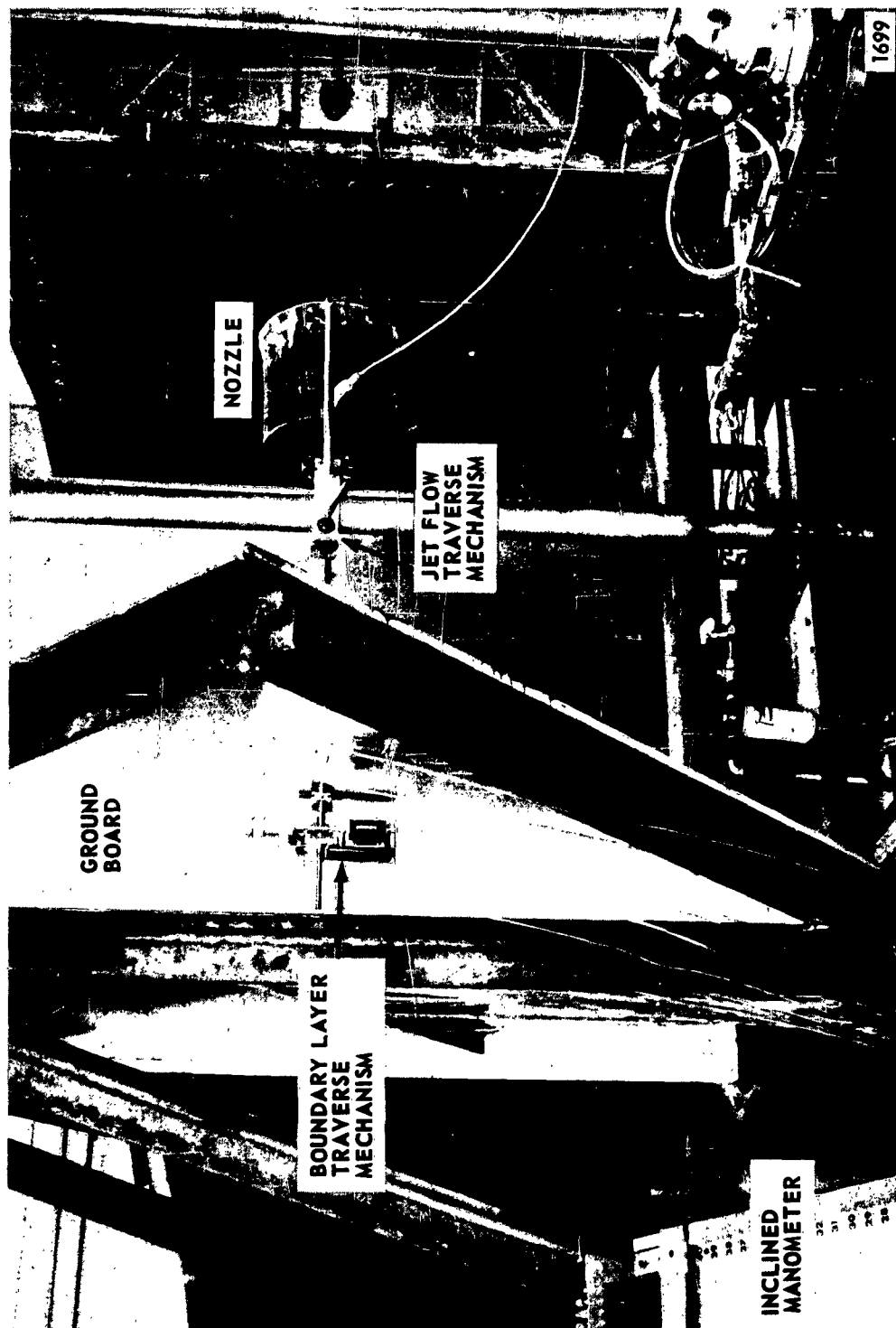


Figure 3. VIEW OF EXPERIMENTAL APPARATUS

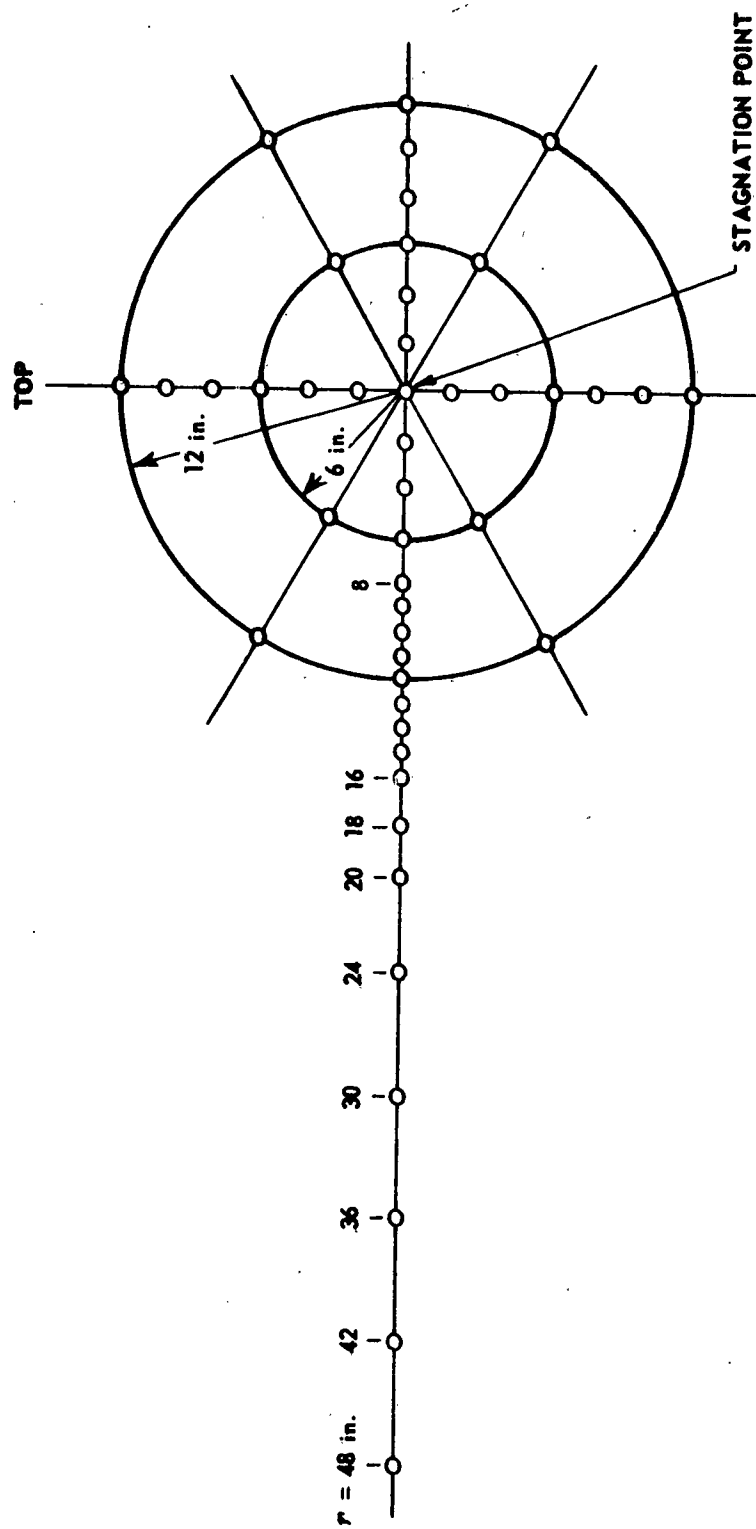


Figure 4. PATTERN OF STATIC PRESSURE TAPS ON GROUND BOARD

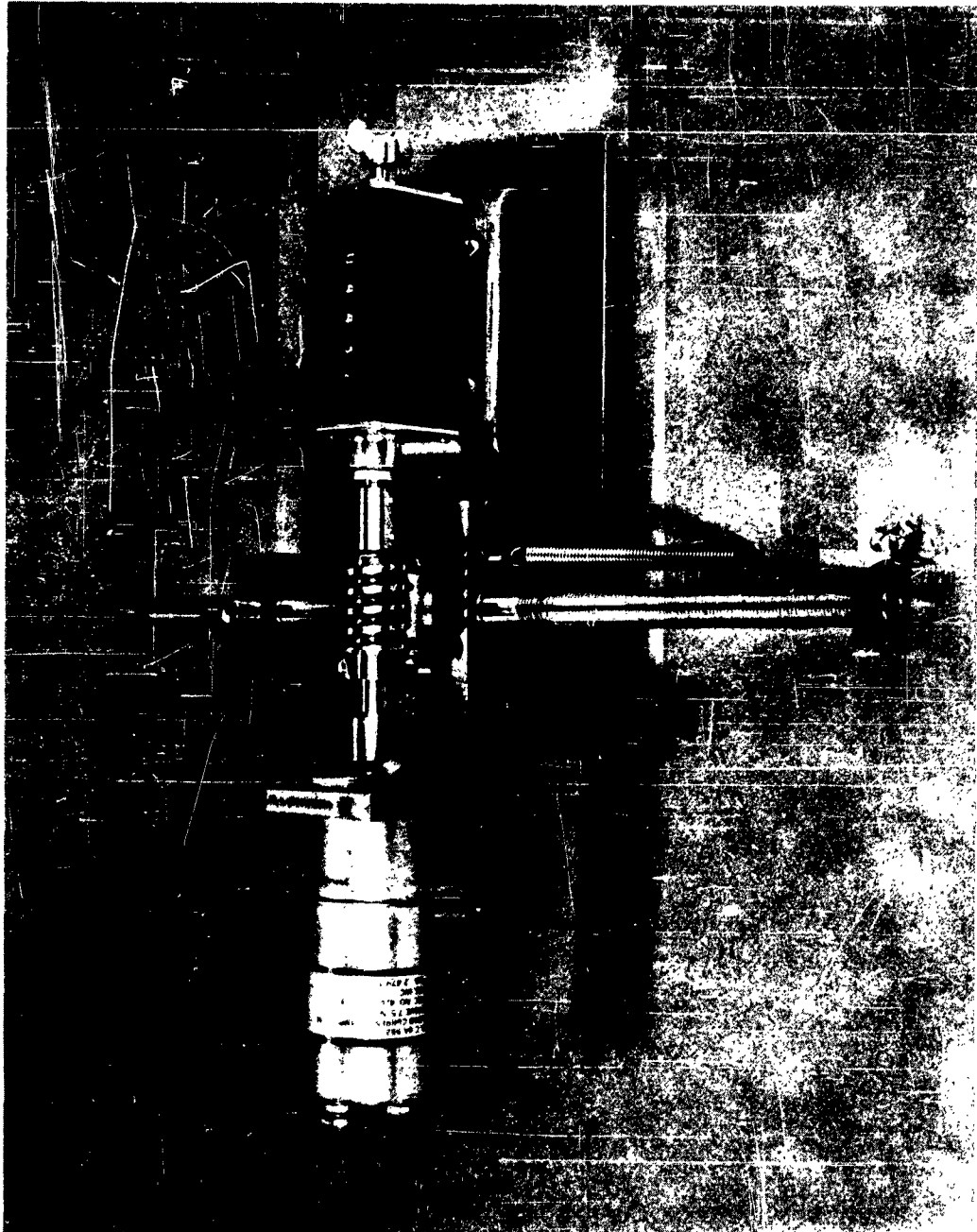


Figure 5. BOUNDARY LAYER TRAVERSE MECHANISM

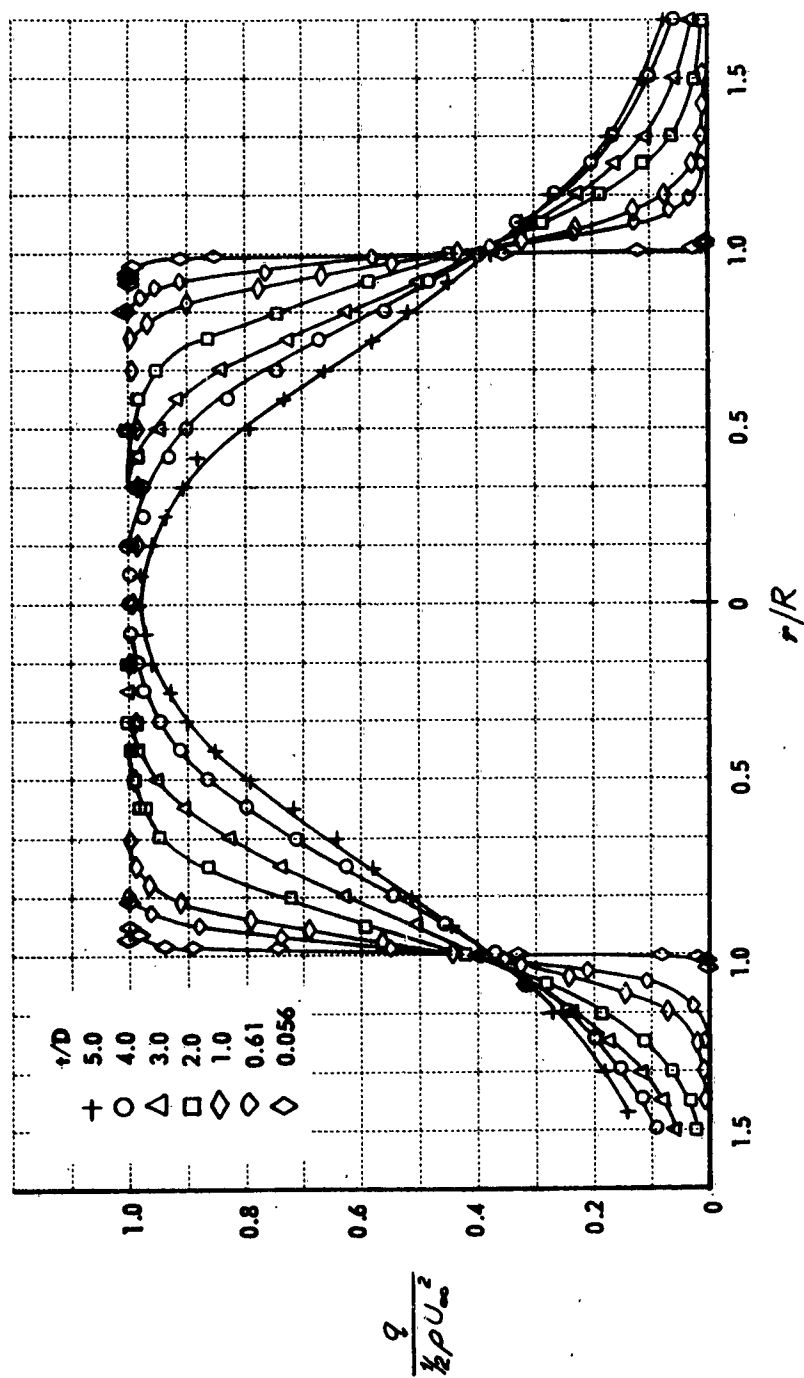


Figure 6. FREE-JET DYNAMIC PRESSURE PROFILES

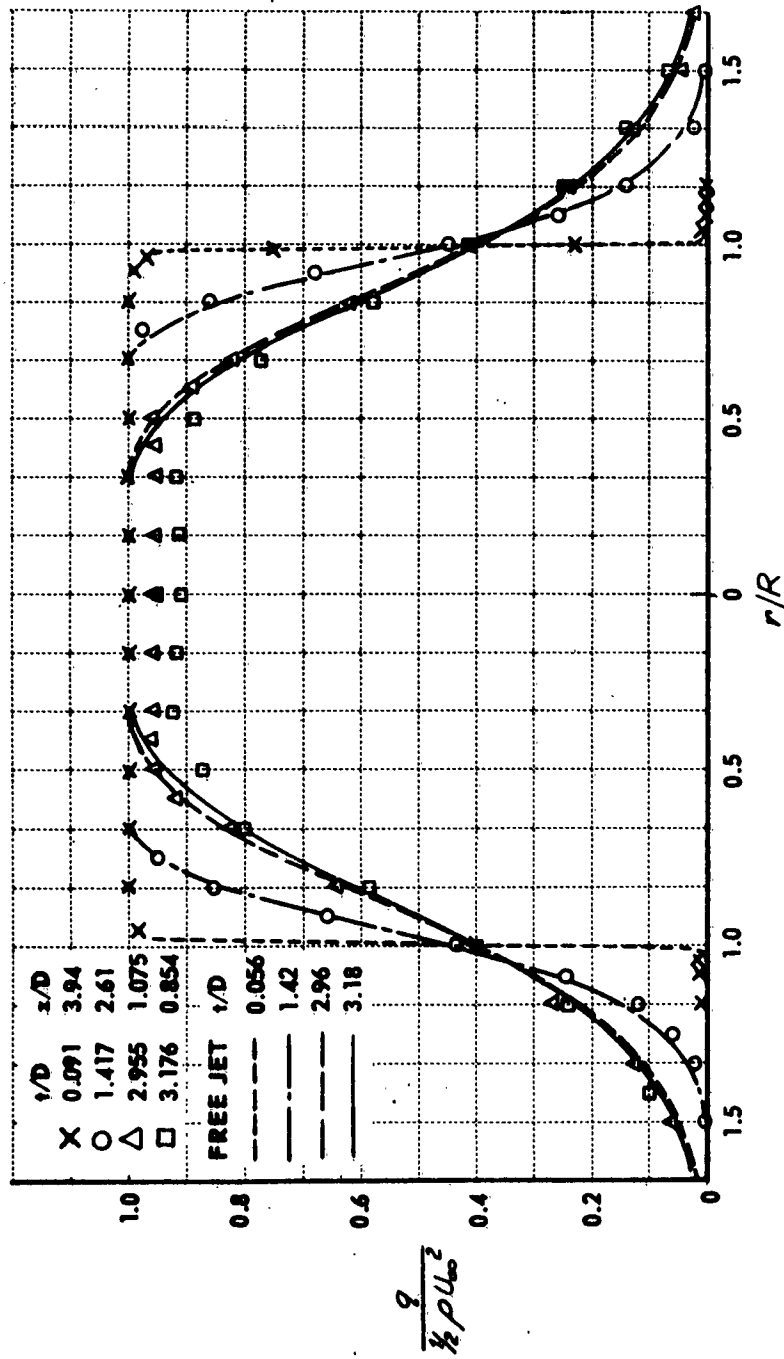


Figure 7. DYNAMIC PRESSURE PROFILES IN IMPINGING JET ($H/D = 4.0$) COMPARED WITH FREE-JET PROFILES

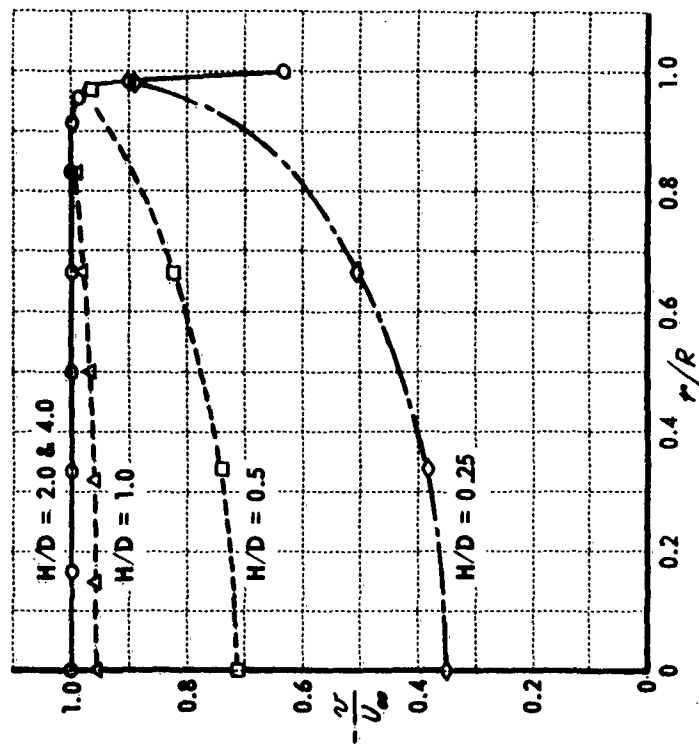


Figure 8. EXPERIMENTAL VELOCITY DISTRIBUTIONS AT NOZZLE EXIT

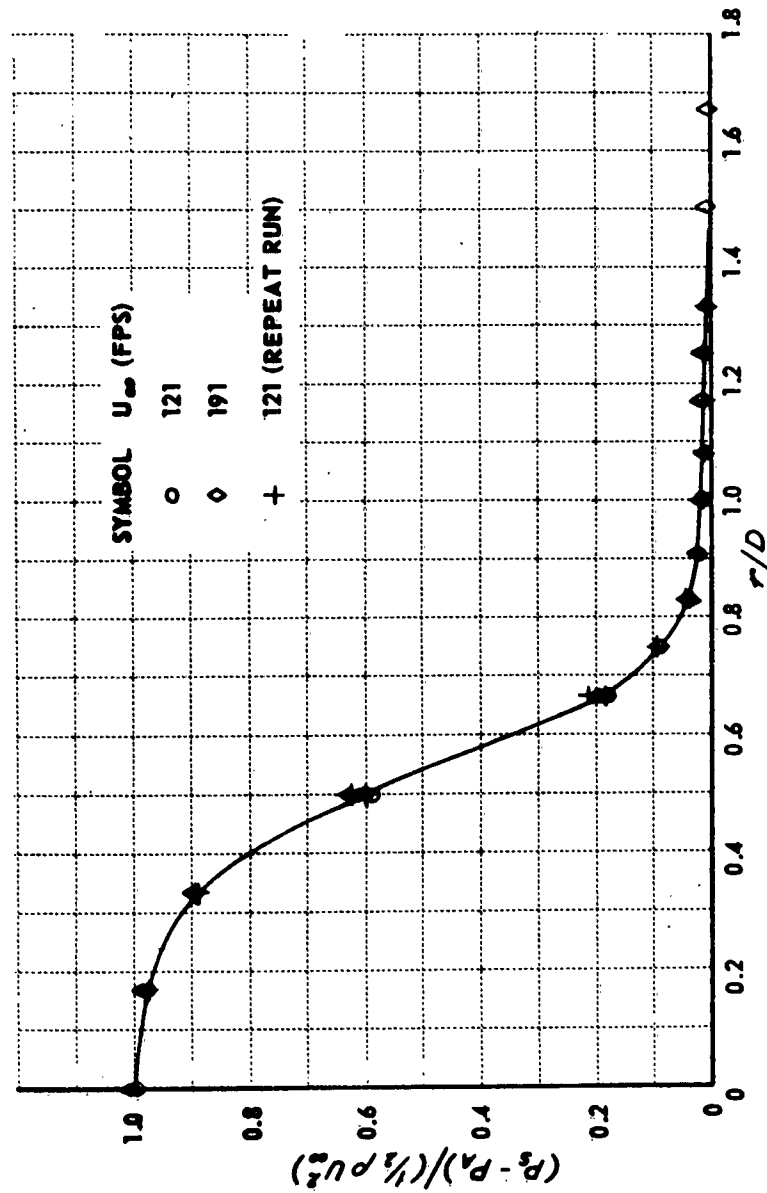


Figure 9(e). GROUND-PLANE STATIC PRESSURE DISTRIBUTION - $H/D = 0.25$

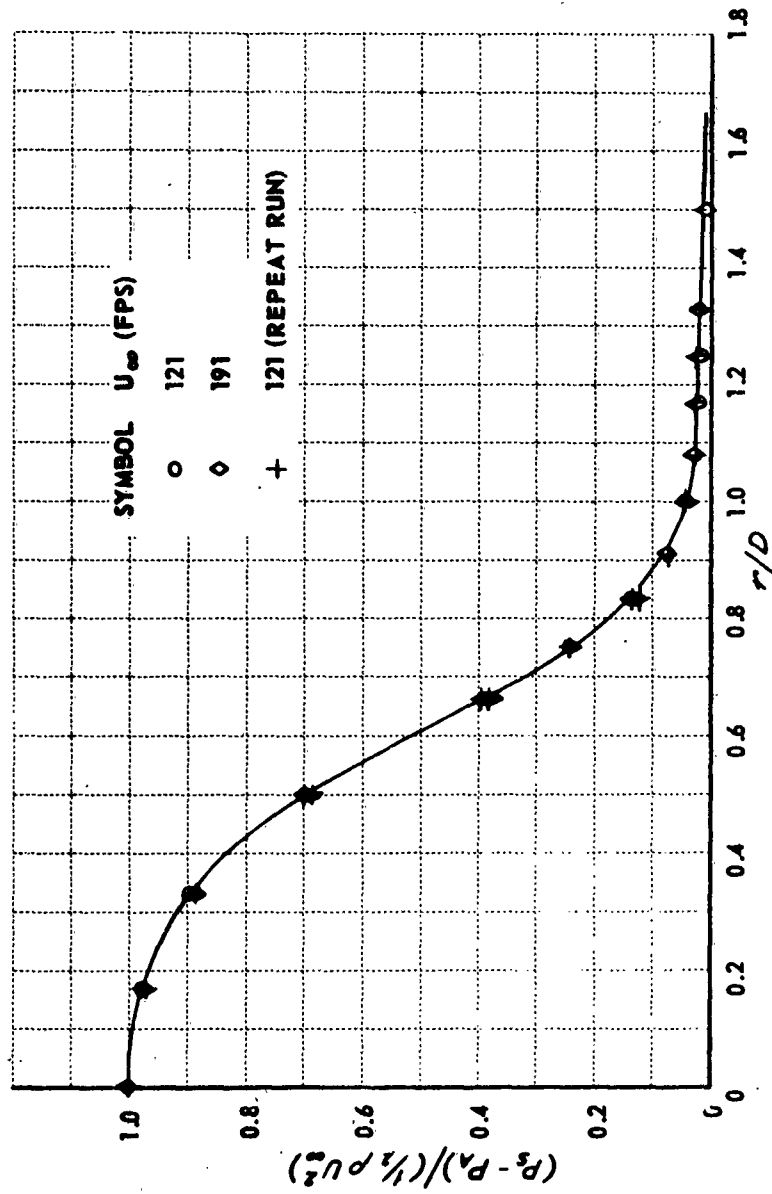


Figure 9(b). GROUND-PLANE STATIC PRESSURE DISTRIBUTION - $H/D = 0.5$

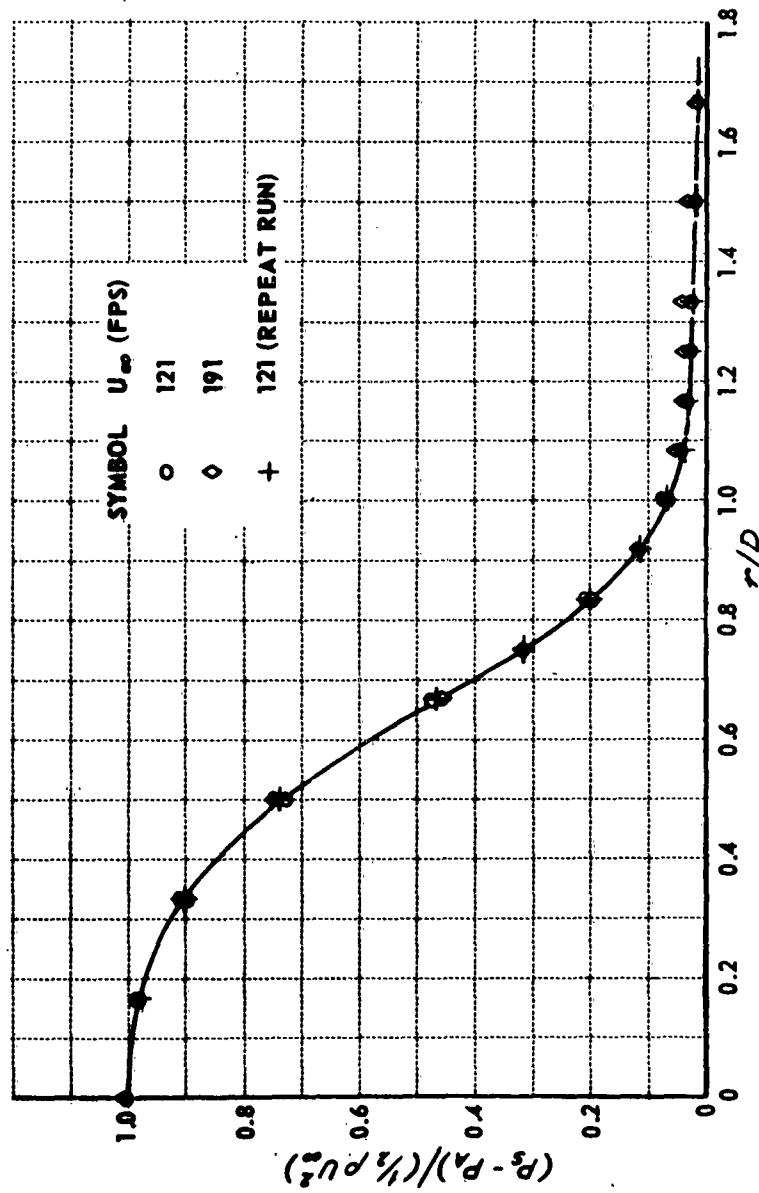


Figure 9(c). GROUND-PLANE STATIC PRESSURE DISTRIBUTION - $H/D = 1.0$

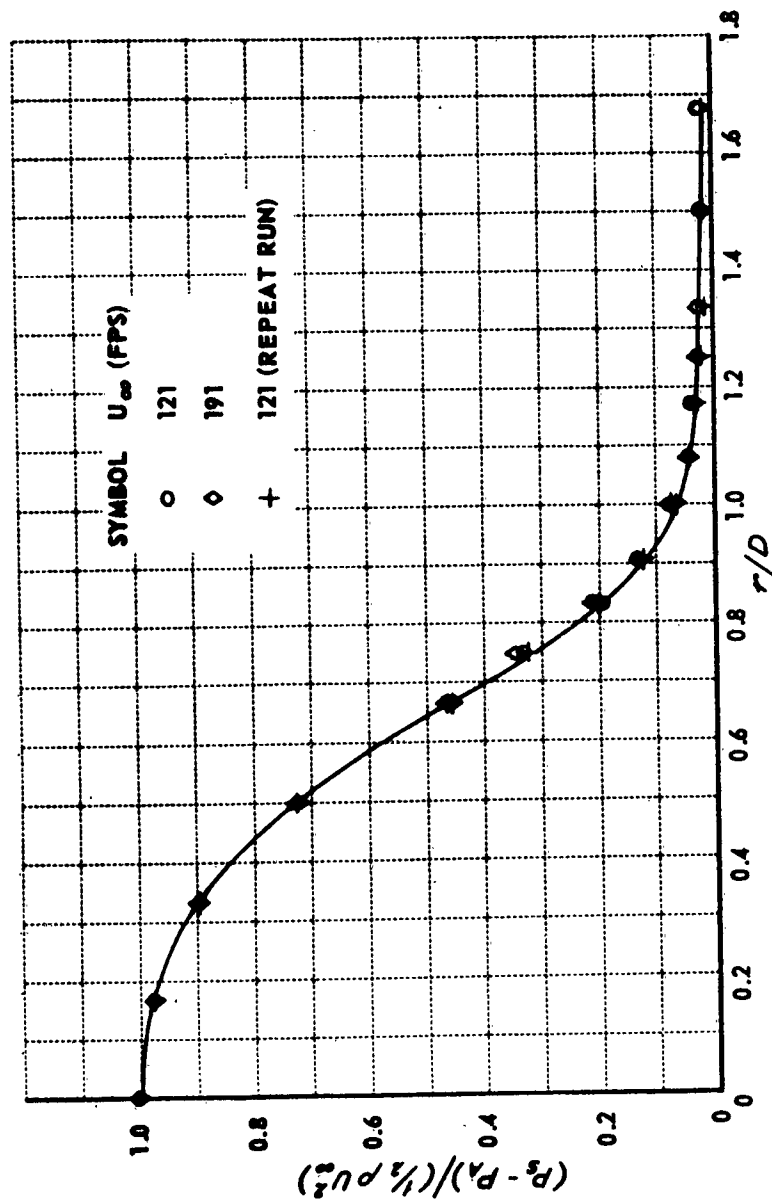


Figure 9(d). GROUND-PLANE STATIC PRESSURE DISTRIBUTION - $H/D = 2.0$

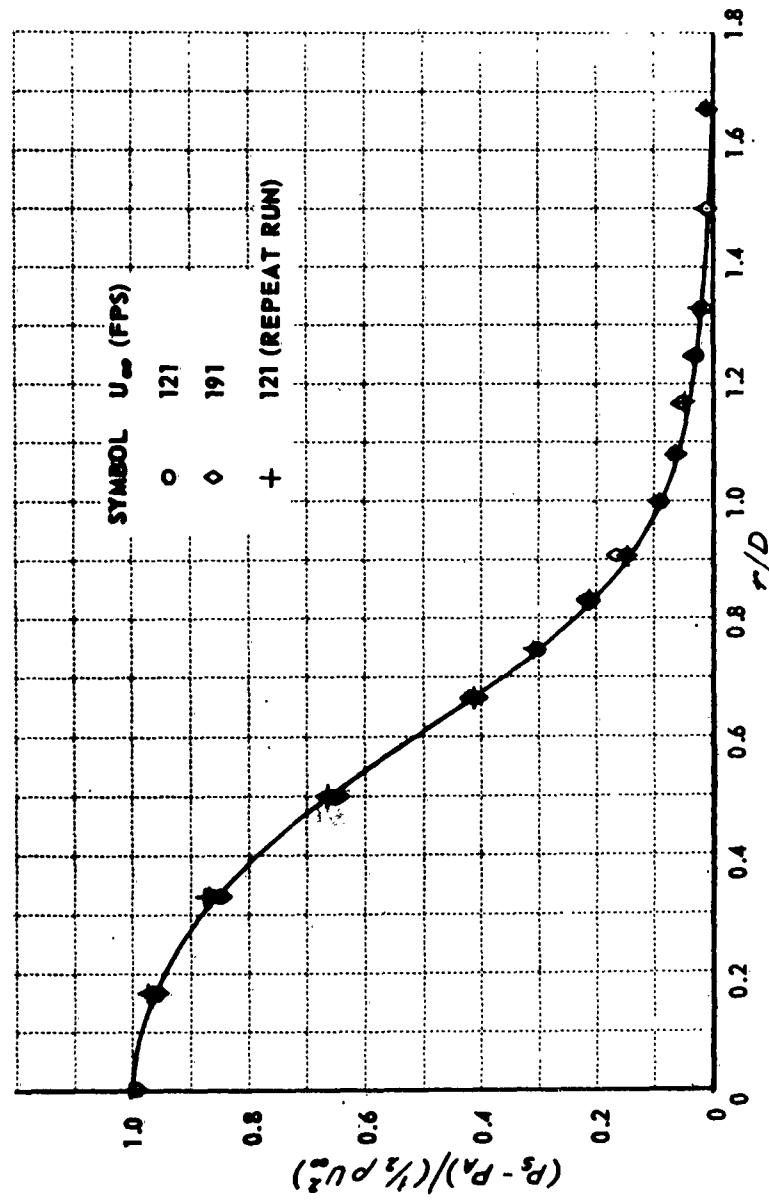


Figure 9(e). GROUND-PLANE STATIC PRESSURE DISTRIBUTION - $H/D = 4.0$

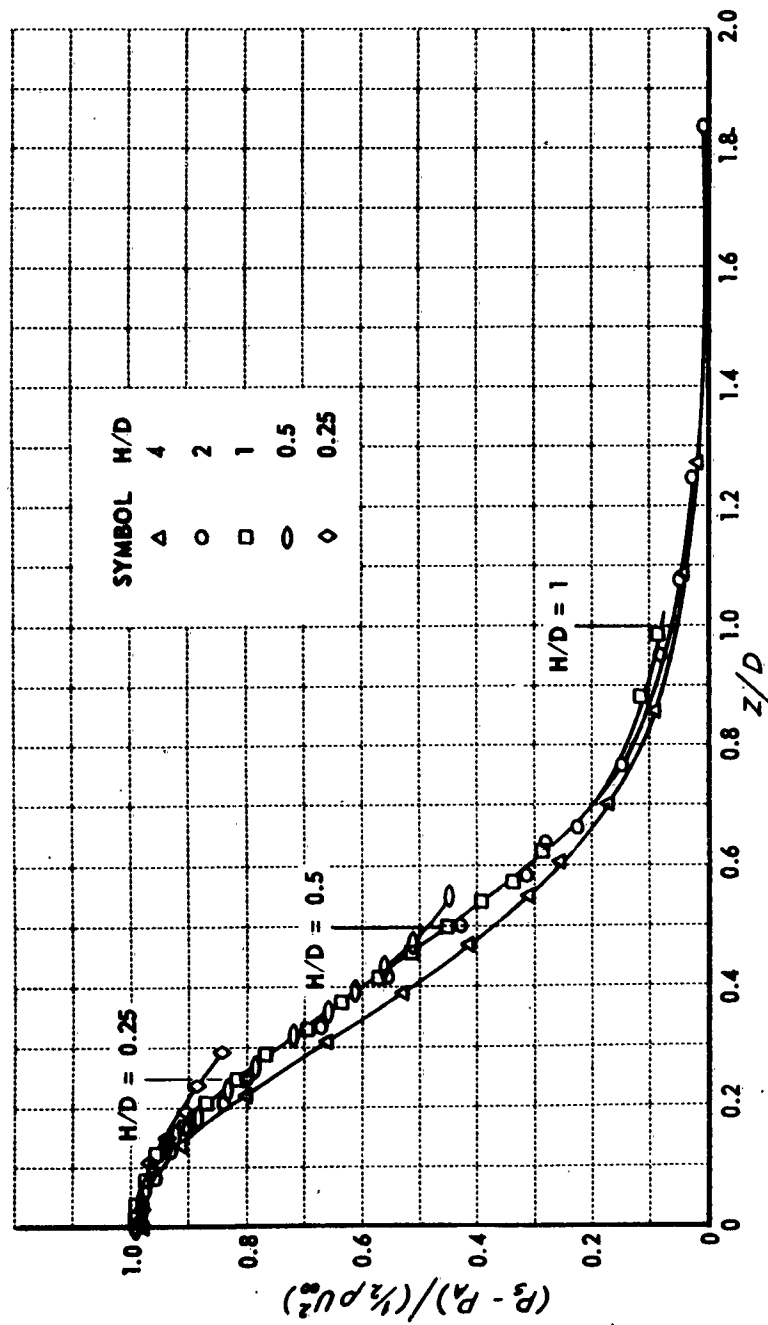


Figure 10. JET-CENTERLINE STATIC PRESSURE DISTRIBUTIONS

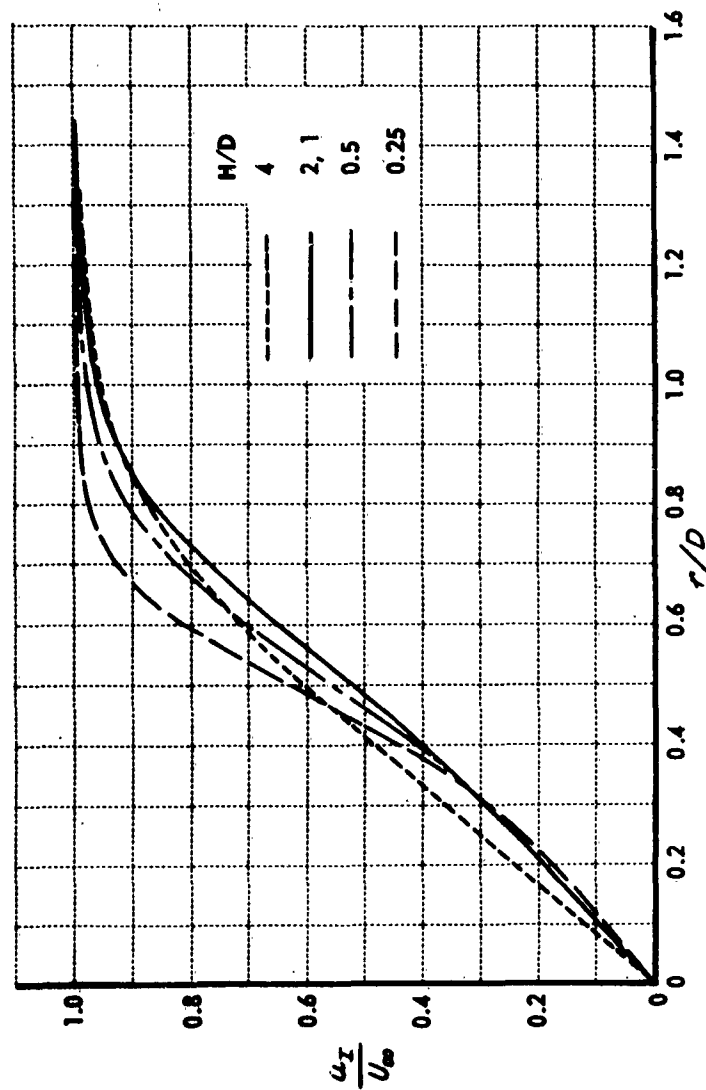


Figure 11. GROUND-PLANE VELOCITY DISTRIBUTIONS COMPUTED FROM EXPERIMENTAL PRESSURE DISTRIBUTIONS

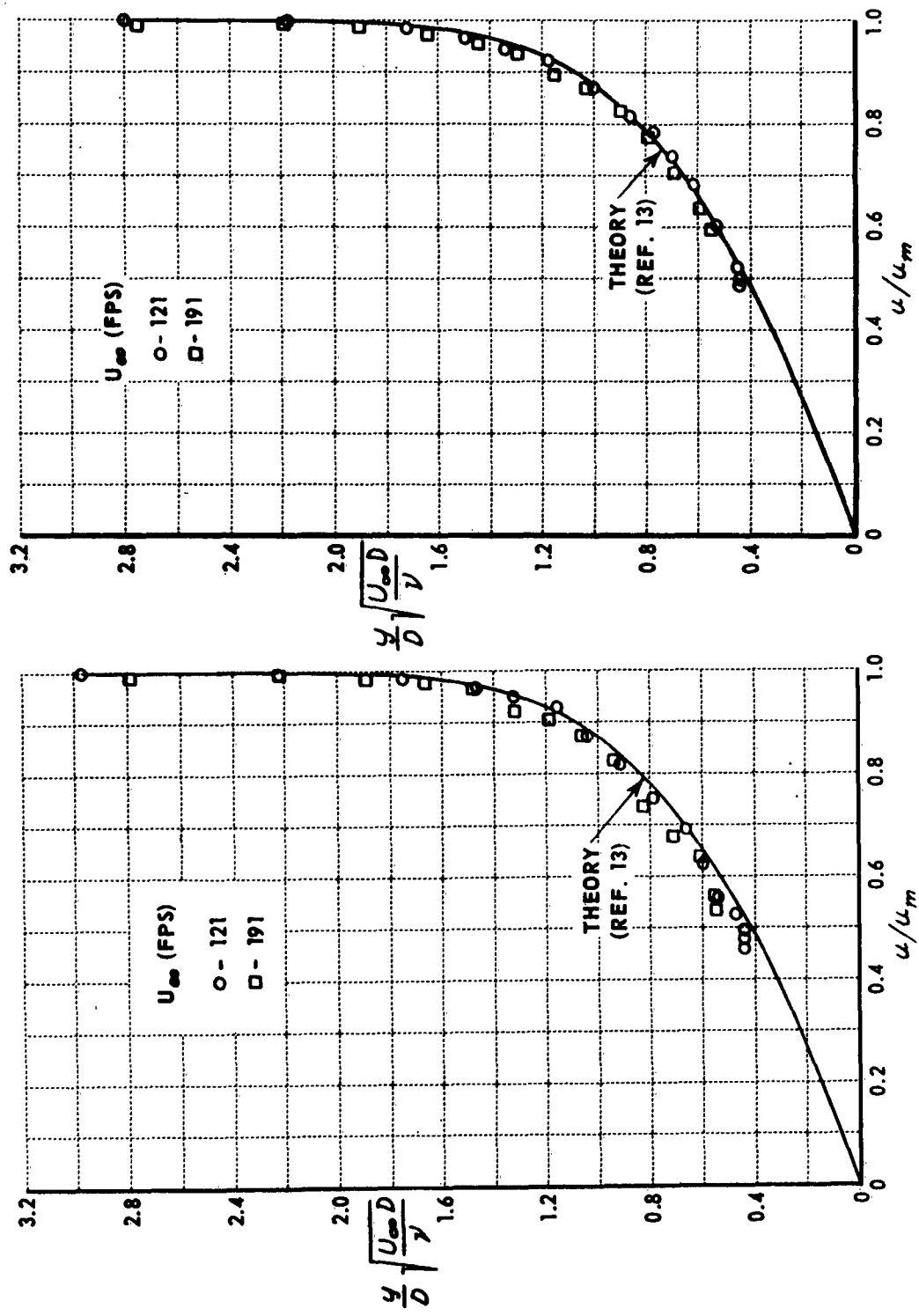


Figure 12(b). GROUND-PLANE BOUNDARY LAYER
PROFILES - $H/D = 0.5, r/D = 0.667$

Figure 12(a). GROUND-PLANE BOUNDARY LAYER
PROFILES - $H/D = 0.50, r/D = 0.5$

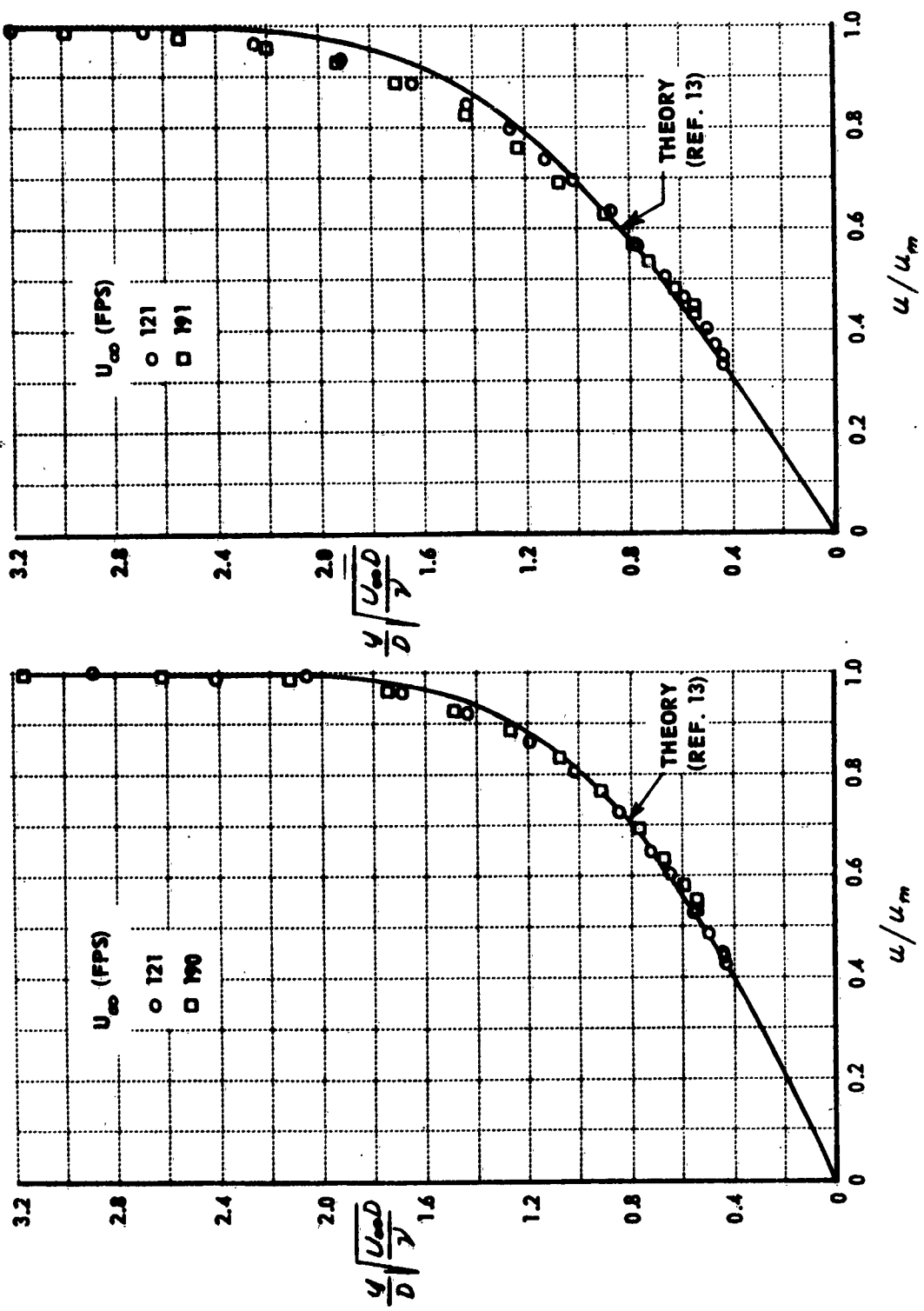


Figure 12(c). GROUND-PLANE BOUNDARY LAYER PROFILES - $H/D = 0.5$, $r/D = 0.83$ Figure 12(d). GROUND-PLANE BOUNDARY LAYER PROFILES - $H/D = 0.5$, $r/D = 1.0$

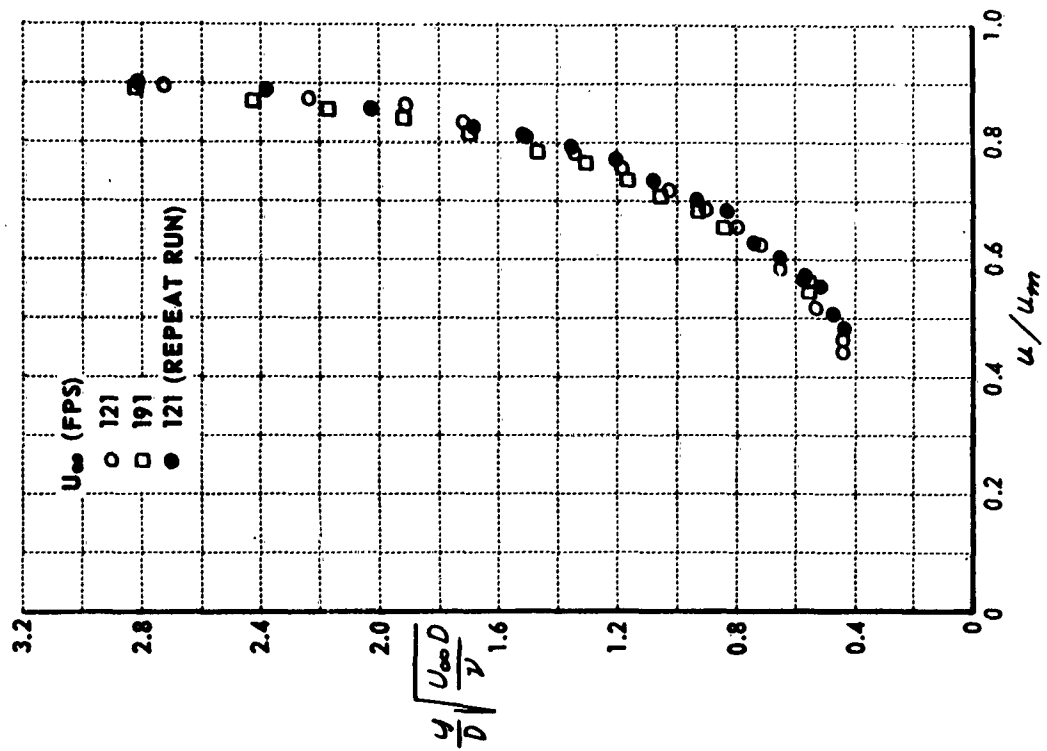


Figure 12(e). GROUND-PLANE BOUNDARY LAYER
PROFILES - $H/D = 0.5$, $r/D = 1.17$

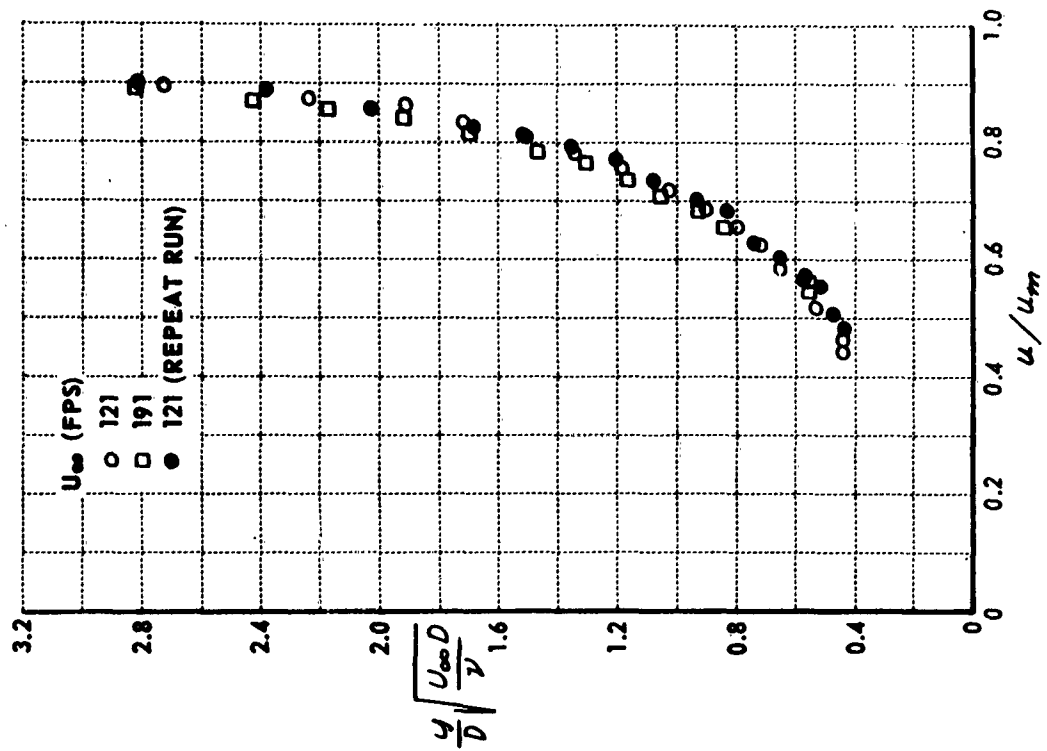


Figure 12(f). GROUND-PLANE BOUNDARY LAYER
PROFILES - $H/D = 0.5$, $r/D = 1.33$

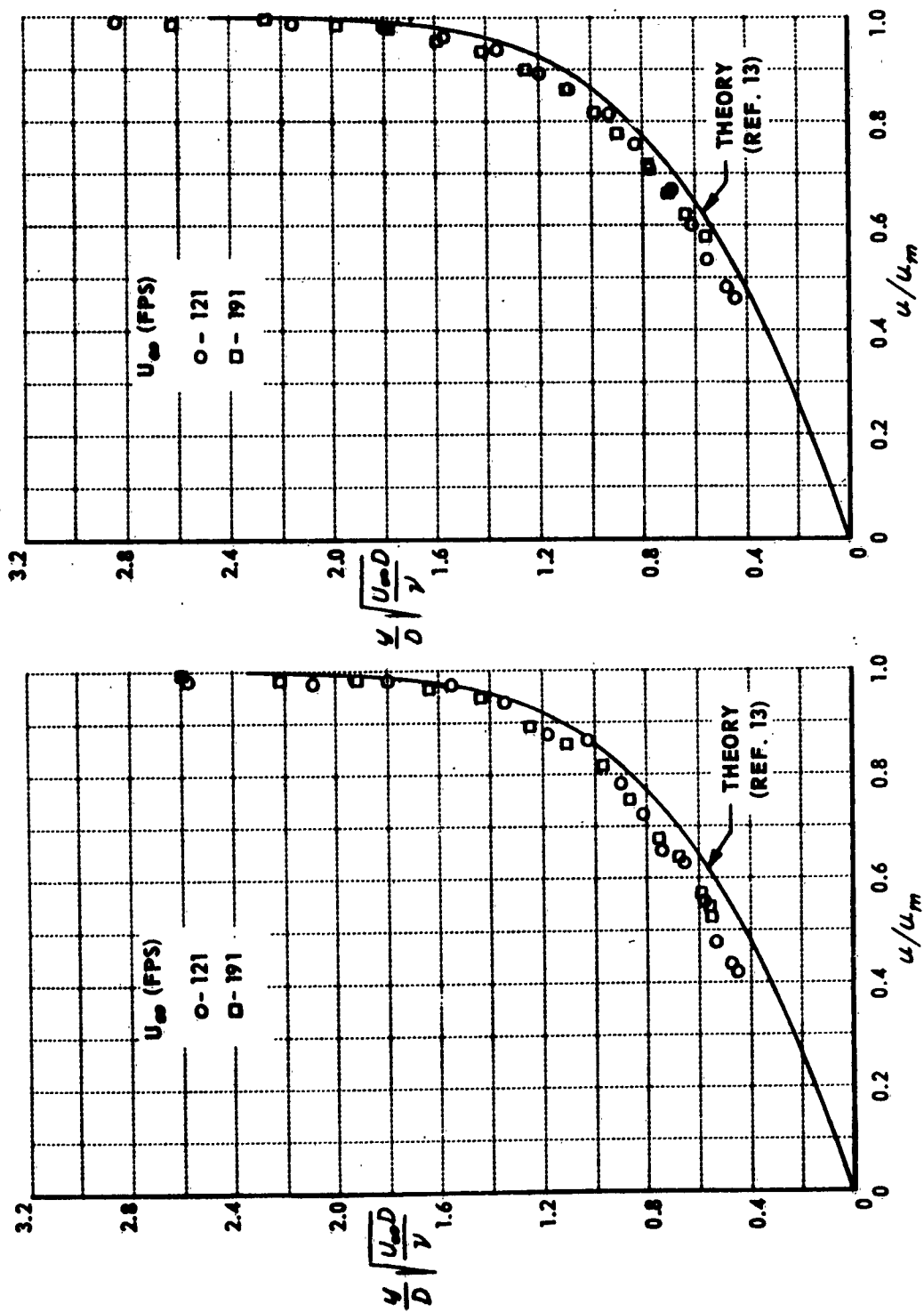


Figure 13(a). GROUND-PLANE BOUNDARY LAYER PROFILES - $H/D = 1.0, r/D = 0.5$

Figure 13(b). GROUND-PLANE BOUNDARY LAYER PROFILES - $H/D = 1.0, r/D = 0.667$

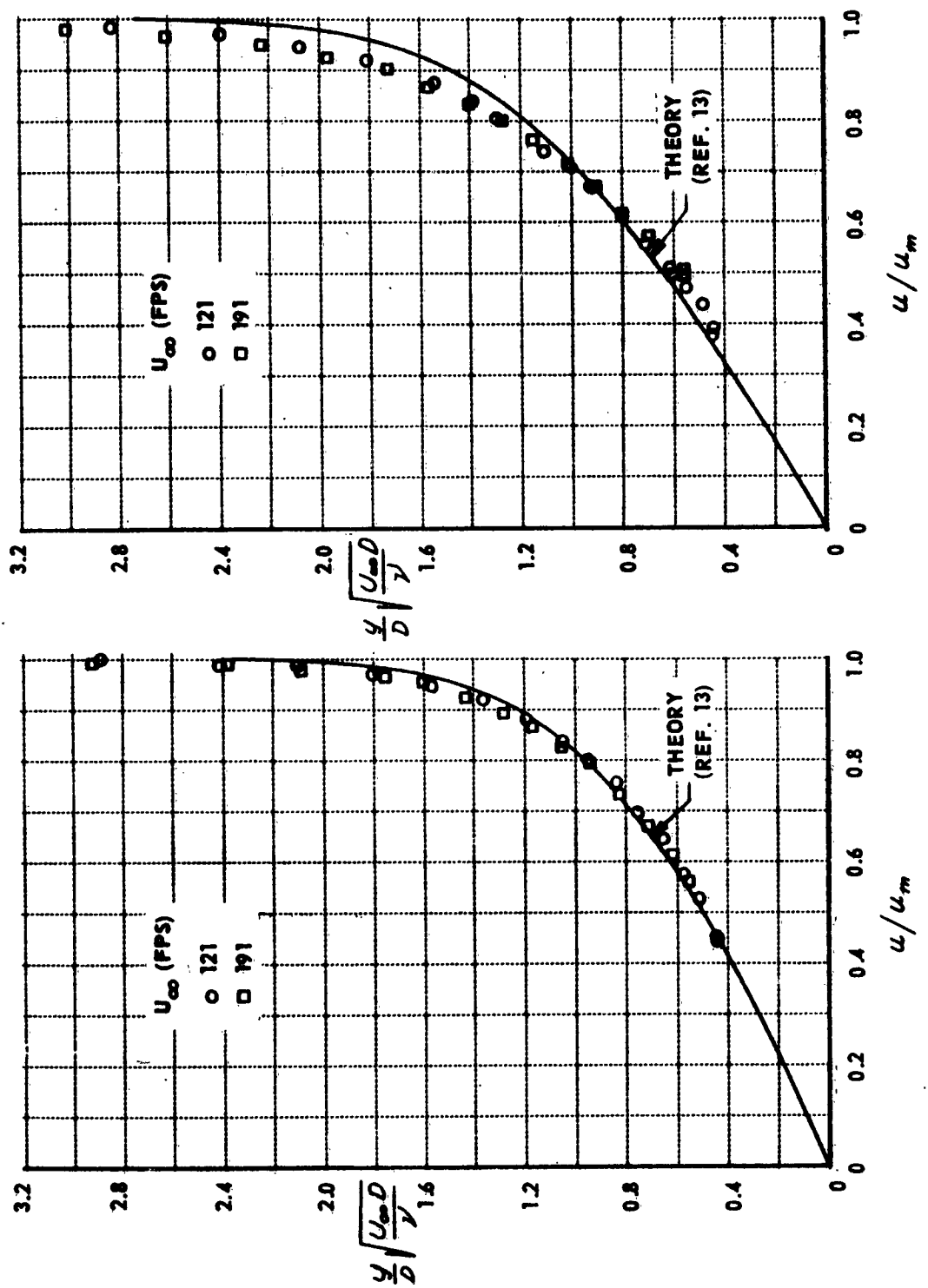


Figure 13(c). GROUND-PLANE BOUNDARY LAYER PROFILES - $H/D = 1.0$, $r/D = 0.83$ Figure 13(d). GROUND-PLANE BOUNDARY LAYER PROFILES - $H/D = 1.0$, $r/D = 1.0$

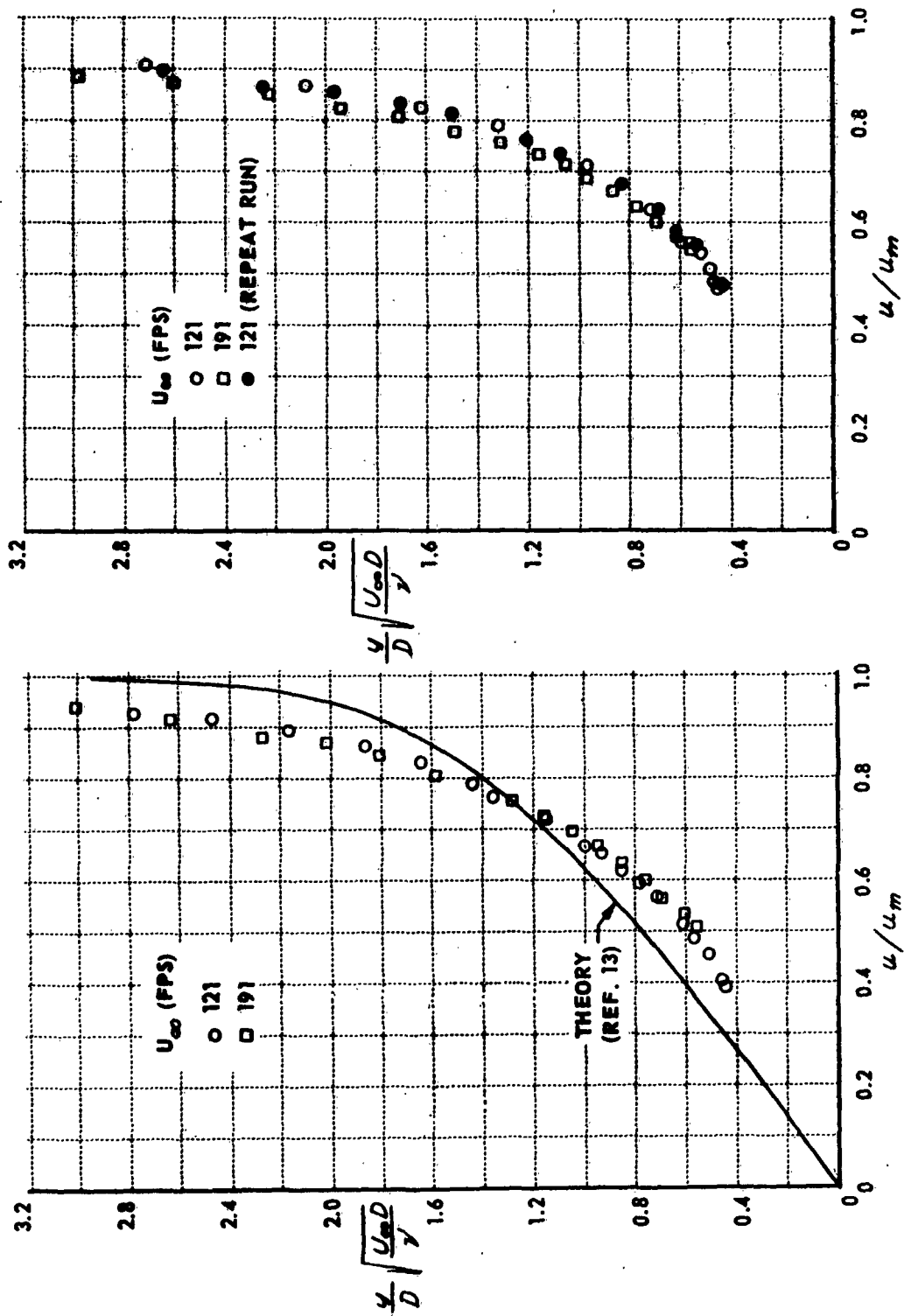


Figure 13(f). GROUND-PLANE BOUNDARY LAYER PROFILES - $H/D = 1.0$, $r/D = 1.33$

Figure 13(e). GROUND-PLANE BOUNDARY LAYER PROFILES - $H/D = 1.0$, $r/D = 1.17$

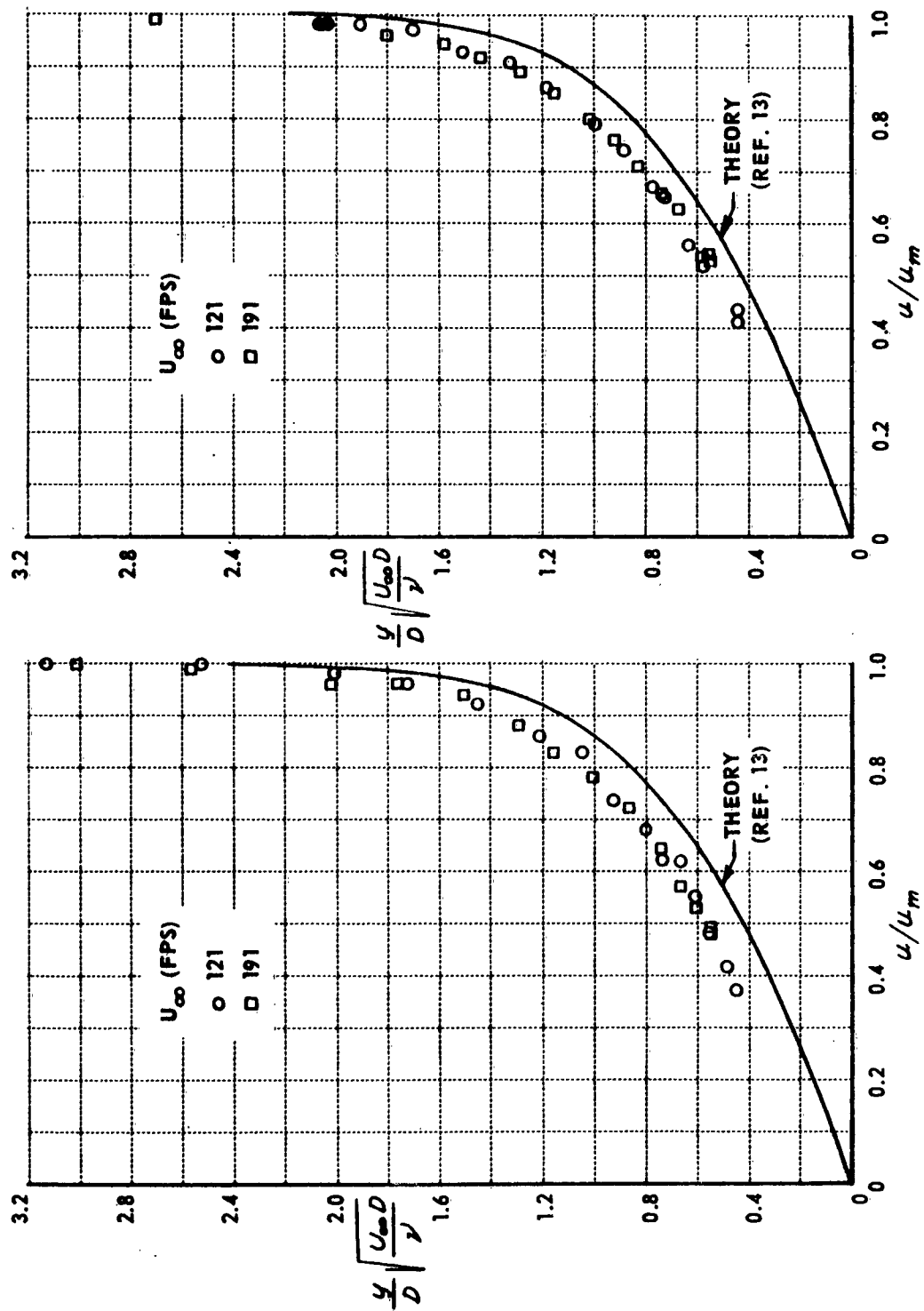


Figure 14(a). GROUND-PLANE BOUNDARY LAYER PROFILES - $H/D = 2.0$, $r/D = 0.5$

Figure 14(b). GROUND-PLANE BOUNDARY LAYER PROFILES - $H/D = 2.0$, $r/D = 0.667$

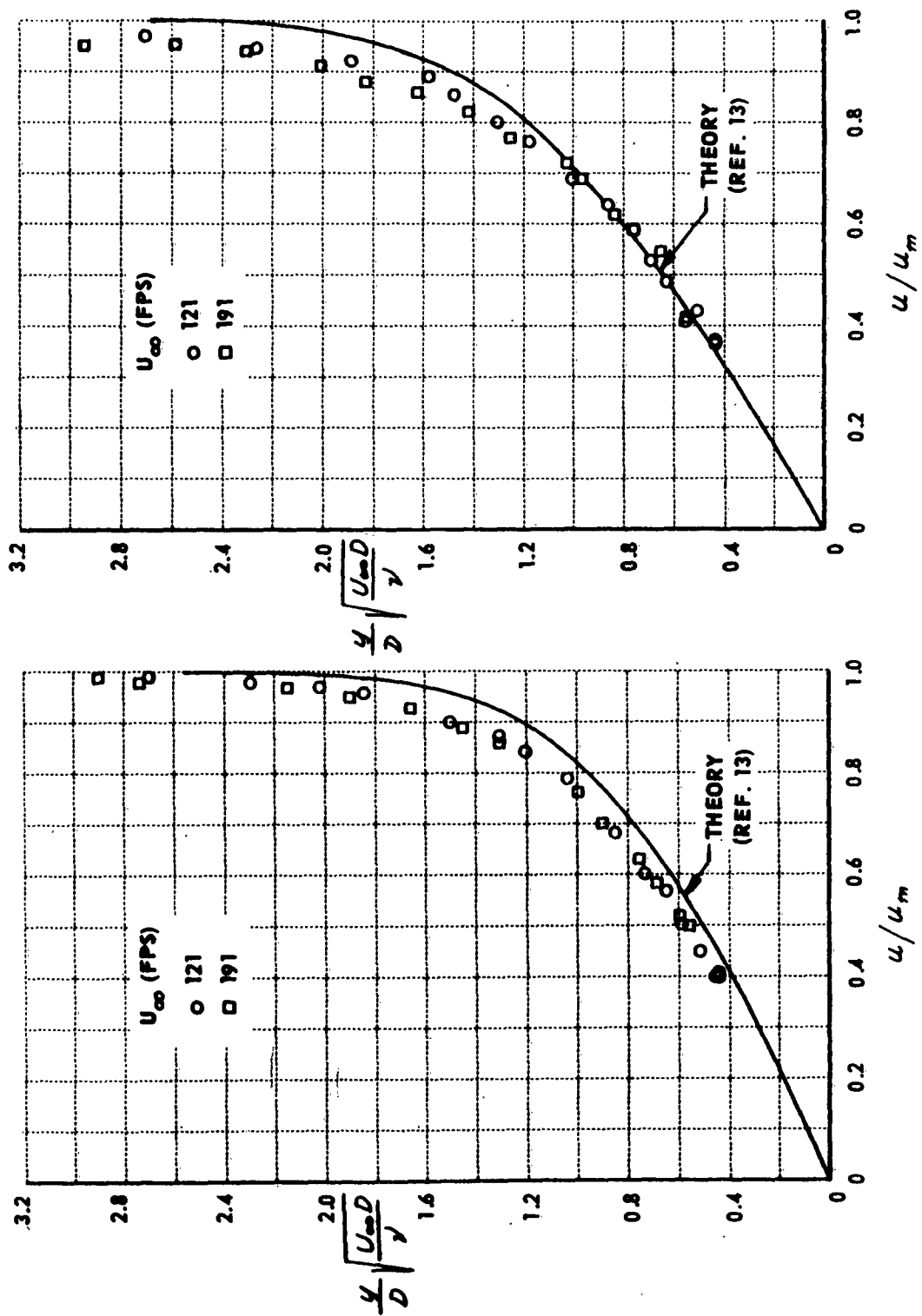
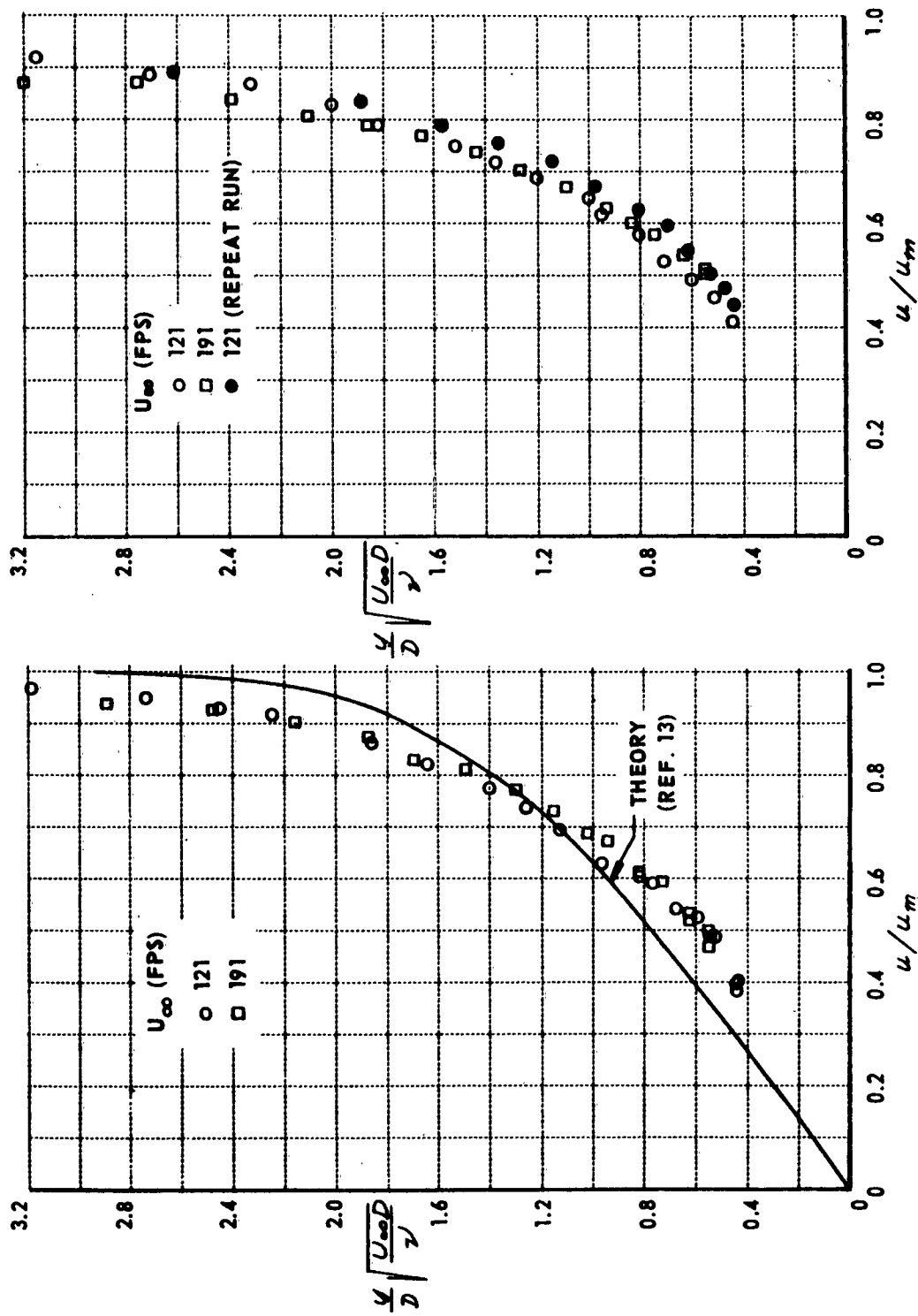


Figure 14(c). GROUND-PLANE BOUNDARY LAYER PROFILES - $H/D = 2.0$, $r/D = 0.83$ Figure 14(d). GROUND-PLANE BOUNDARY LAYER PROFILES - $H/D = 2.0$, $r/D = 1.0$



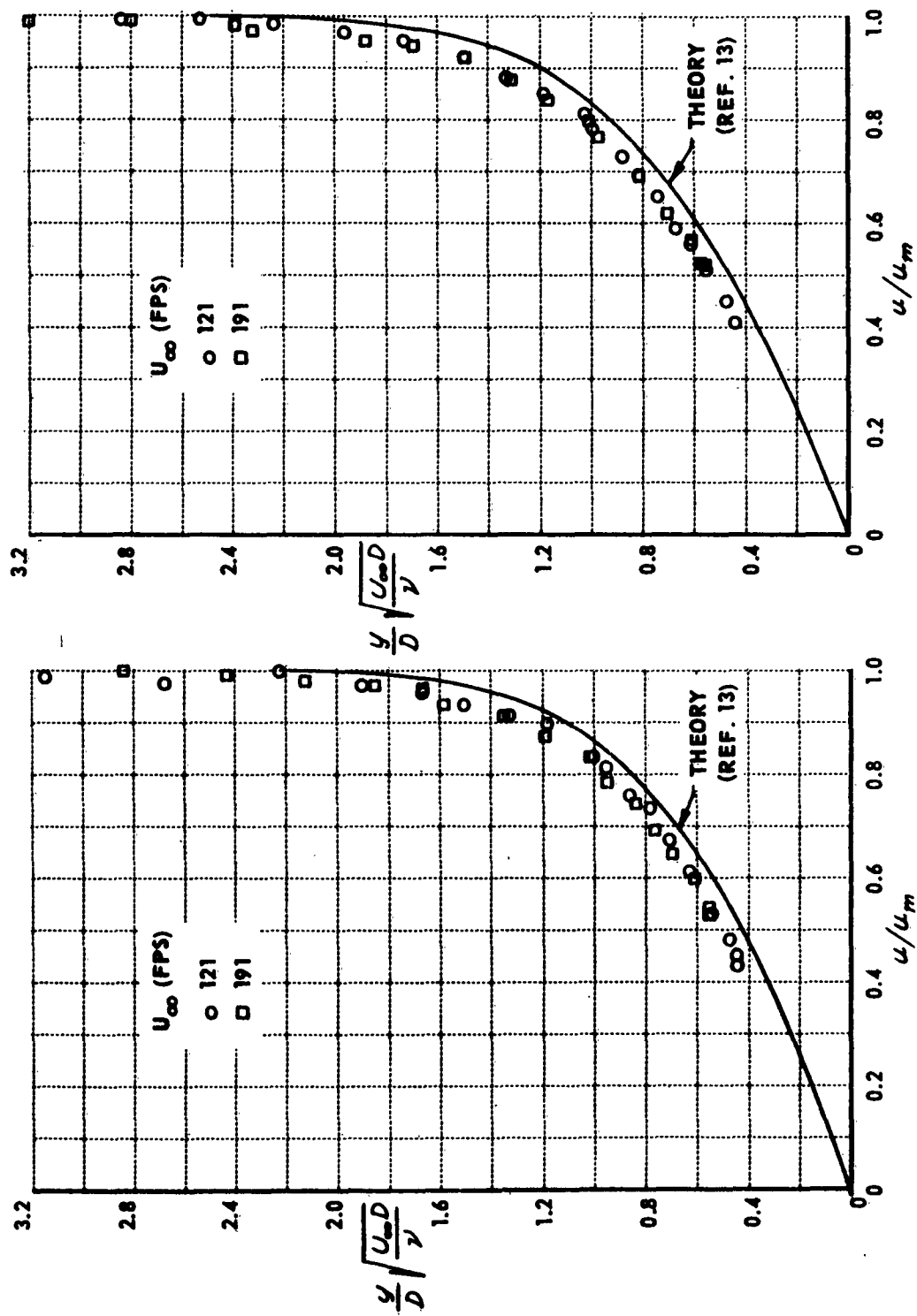


Figure 15(b). GROUND-PLANE BOUNDARY LAYER
PROFILES - $H/D = 4.0$, $r/D = 0.667$

Figure 15(a). GROUND-PLANE BOUNDARY LAYER
PROFILES - $H/D = 4.0$, $r/D = 0.5$

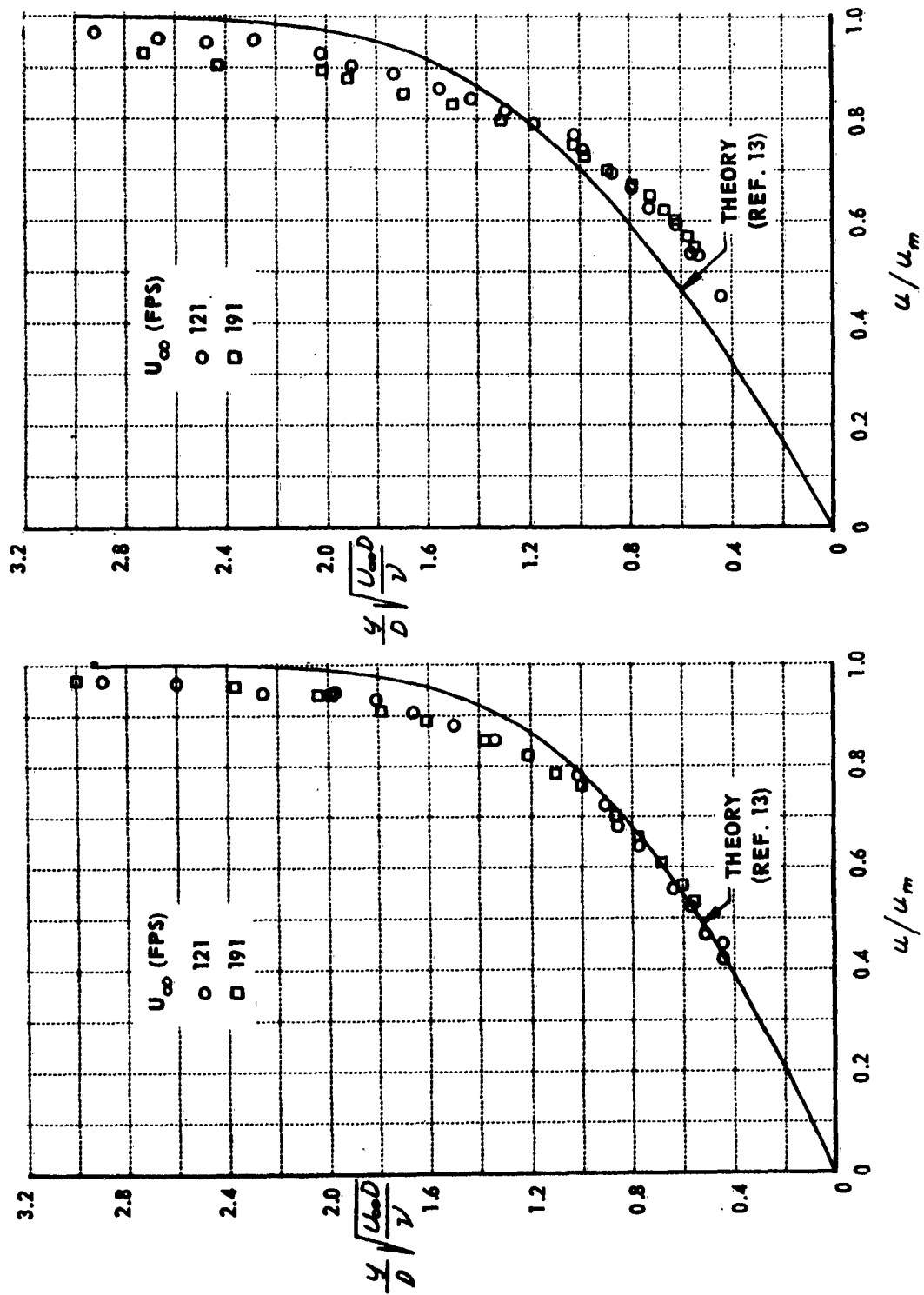


Figure 15(c). GROUND-PLANE BOUNDARY LAYER PROFILES - $H/D = 4.0$, $r/D = 0.83$

Figure 15(d). GROUND-PLANE BOUNDARY LAYER PROFILES - $H/D = 4.0$, $r/D = 1.0$

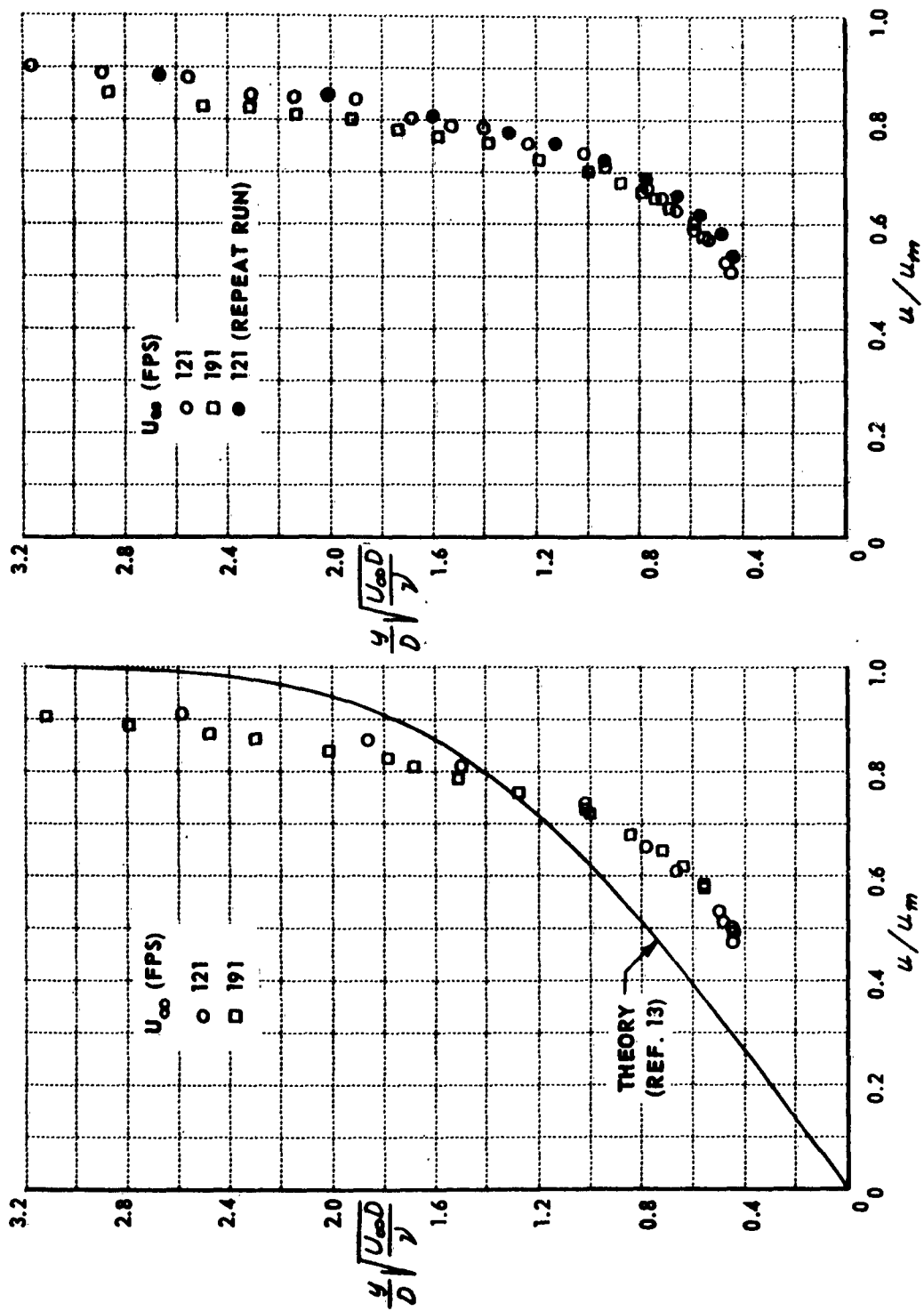


Figure 15(e). GROUND-PLANE BOUNDARY LAYER PROFILES - $H/D = 4.0$, $r/D = 1.17$ Figure 15(f). GROUND-PLANE BOUNDARY LAYER PROFILES - $H/D = 4.0$, $r/D = 1.33$

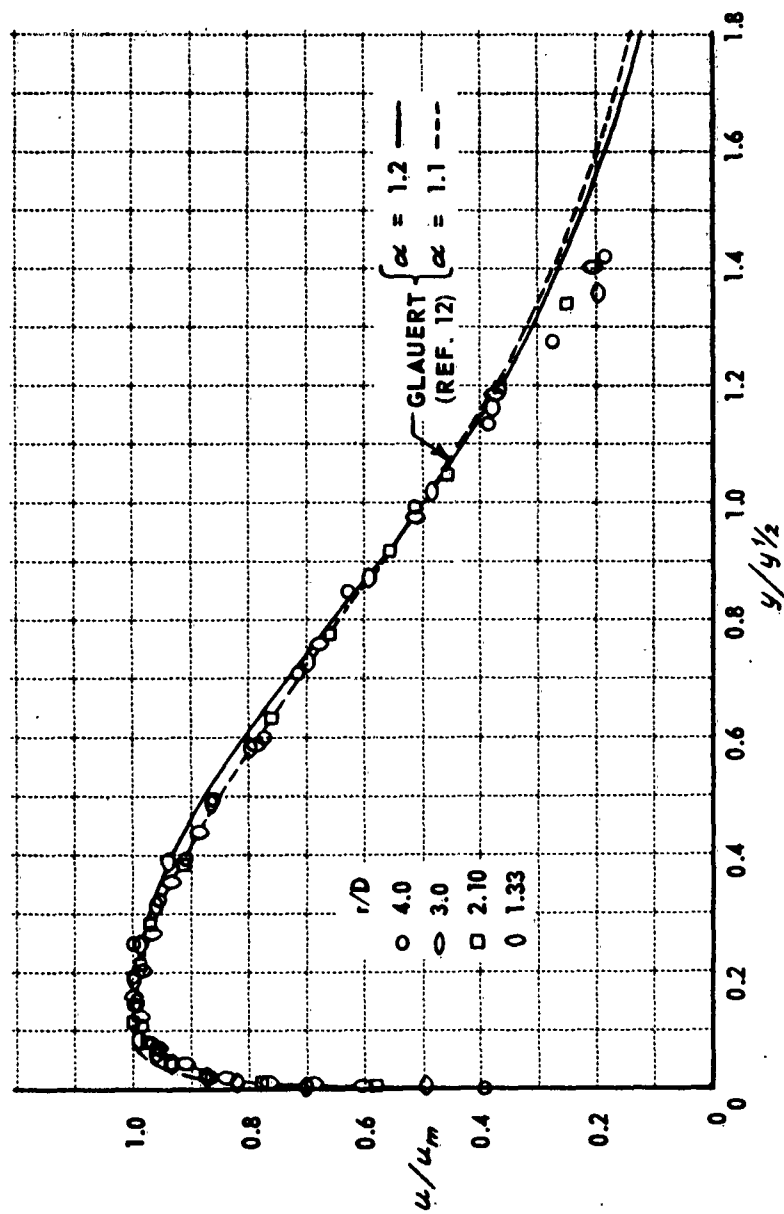


Figure 16(a). VELOCITY PROFILES NEAR THE GROUND FOR $r/D > 1.0$
 $H/D = 0.25$, $U_\infty = 191$ FPS

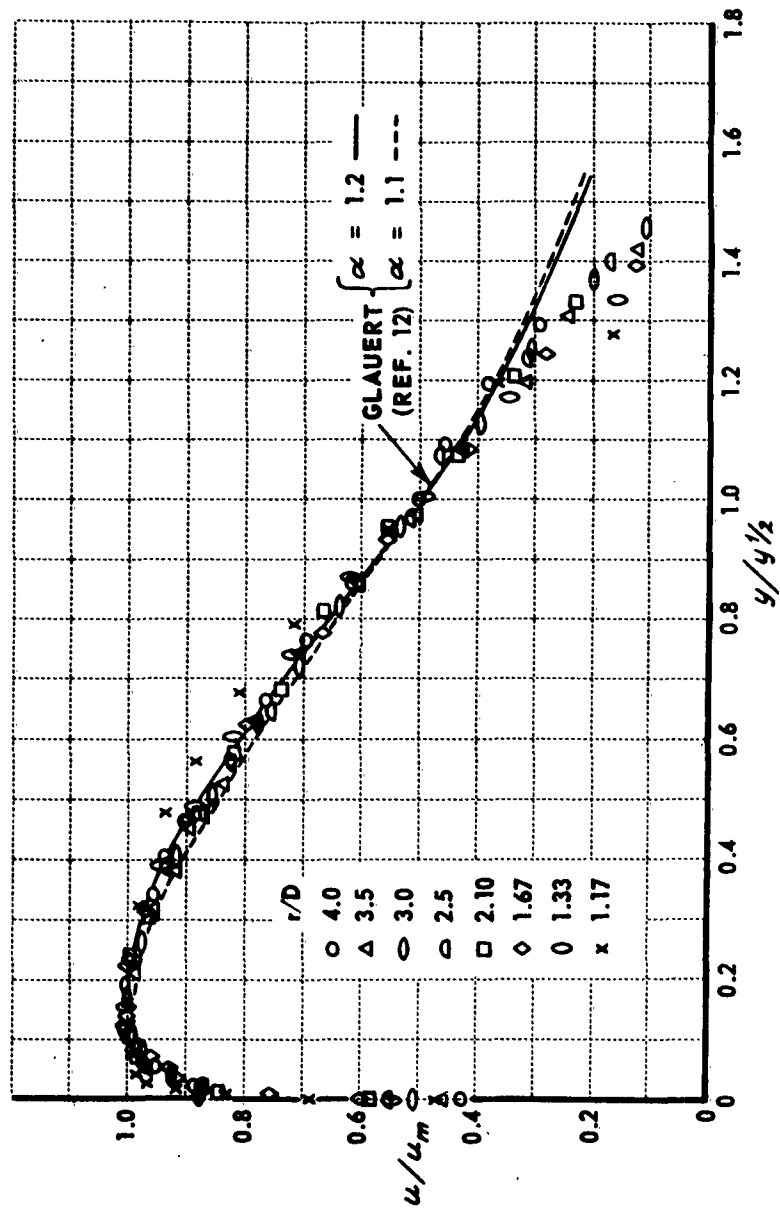


Figure 16(b). VELOCITY PROFILES NEAR THE GROUND FOR $r/D > 1.0$
 $H/D = 0.50$, $U_\infty = 191$ FPS

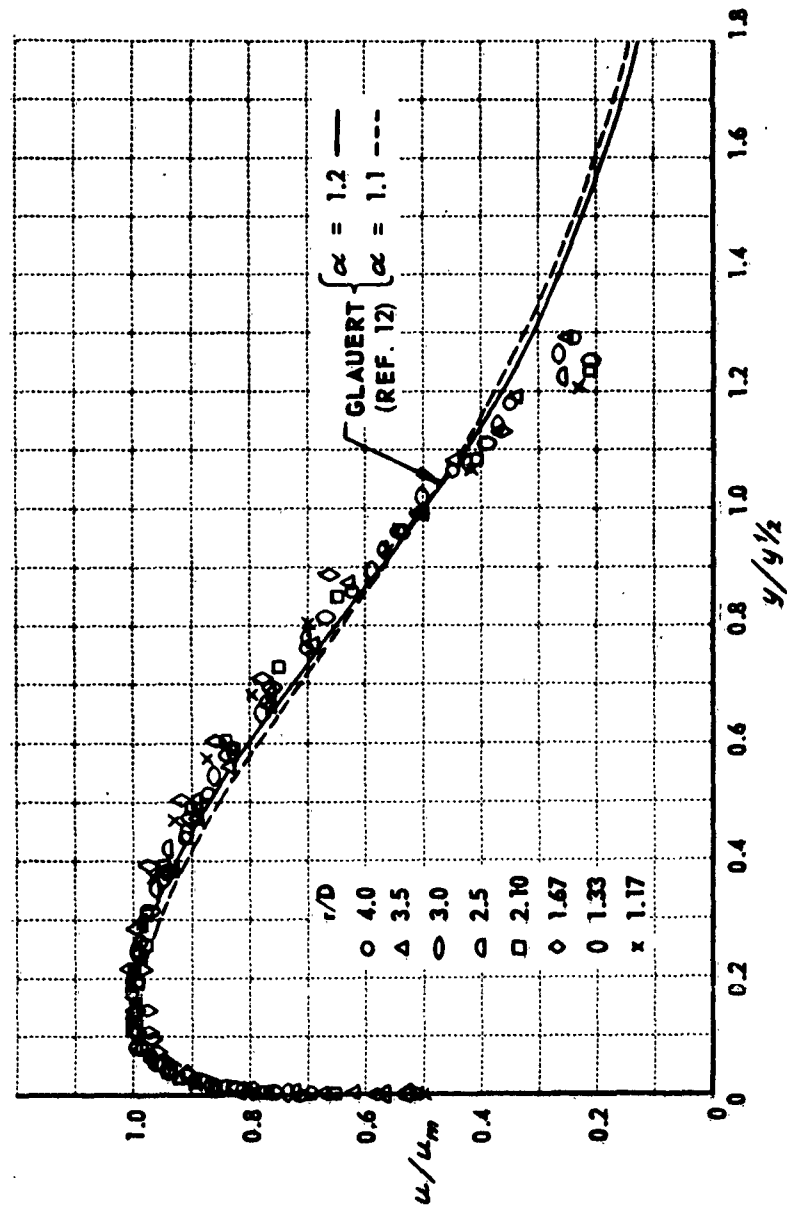


Figure 16(c). VELOCITY PROFILES NEAR THE GROUND FOR $r/D > 1.0$
 $H/D = 1.0$, $U_\infty = 191$ FPS

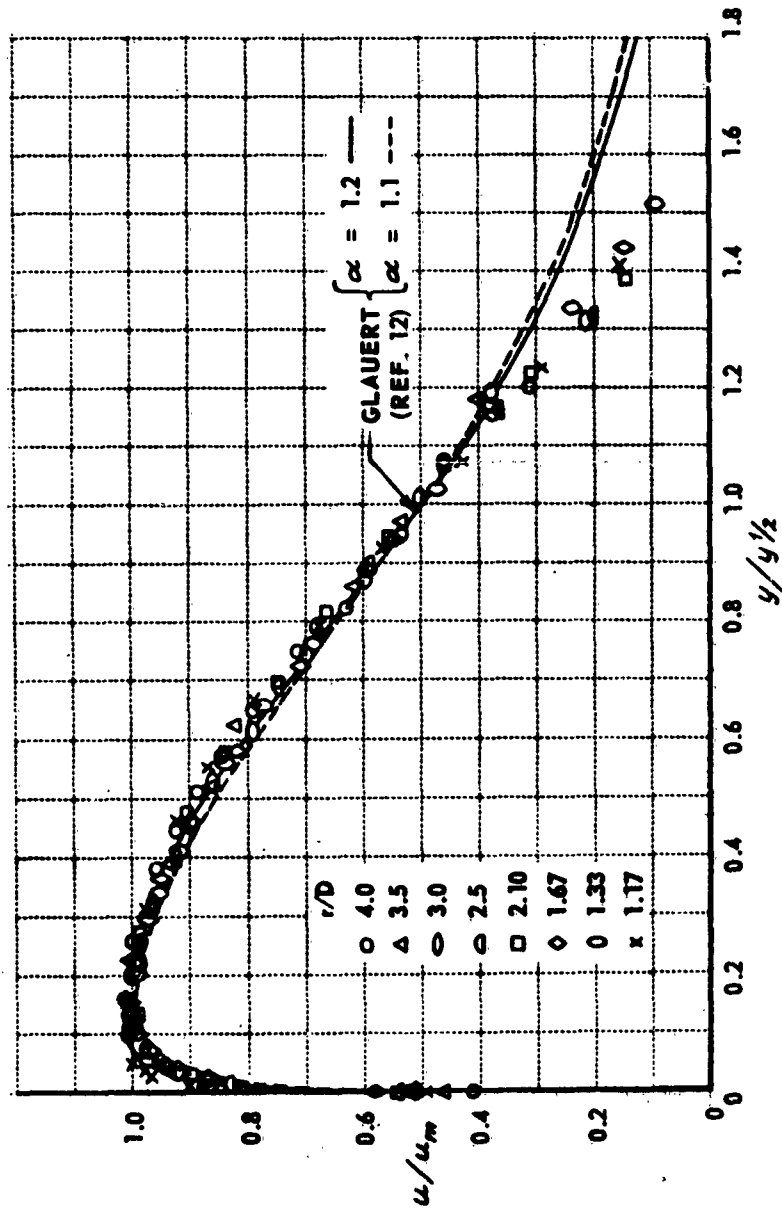


Figure 16(d). VELOCITY PROFILES NEAR THE GROUND FOR $r/D > 1.0$
 $H/D = 2.0$, $U_\infty = 191$ FPS

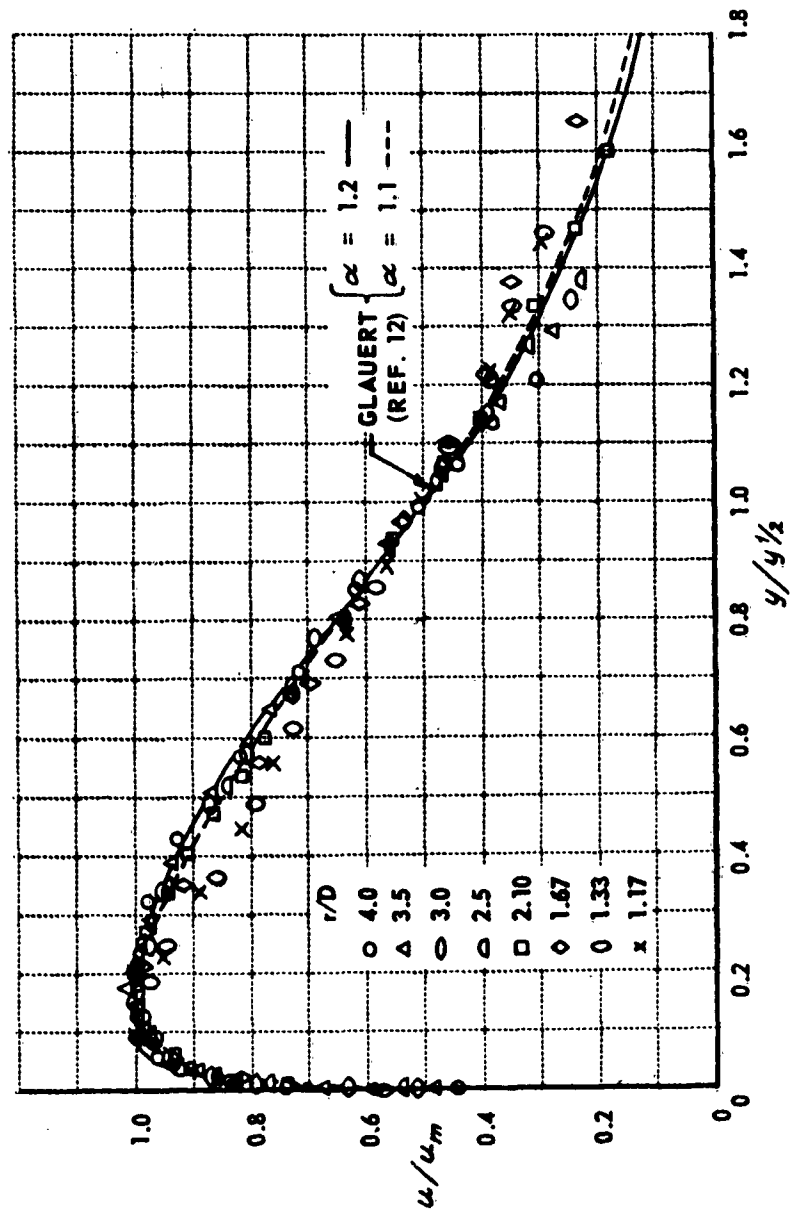


Figure 16(e). VELOCITY PROFILES NEAR THE GROUND FOR $r/D > 1.0$
 $H/D = 4.0$, $U_\infty = 191$ FPS

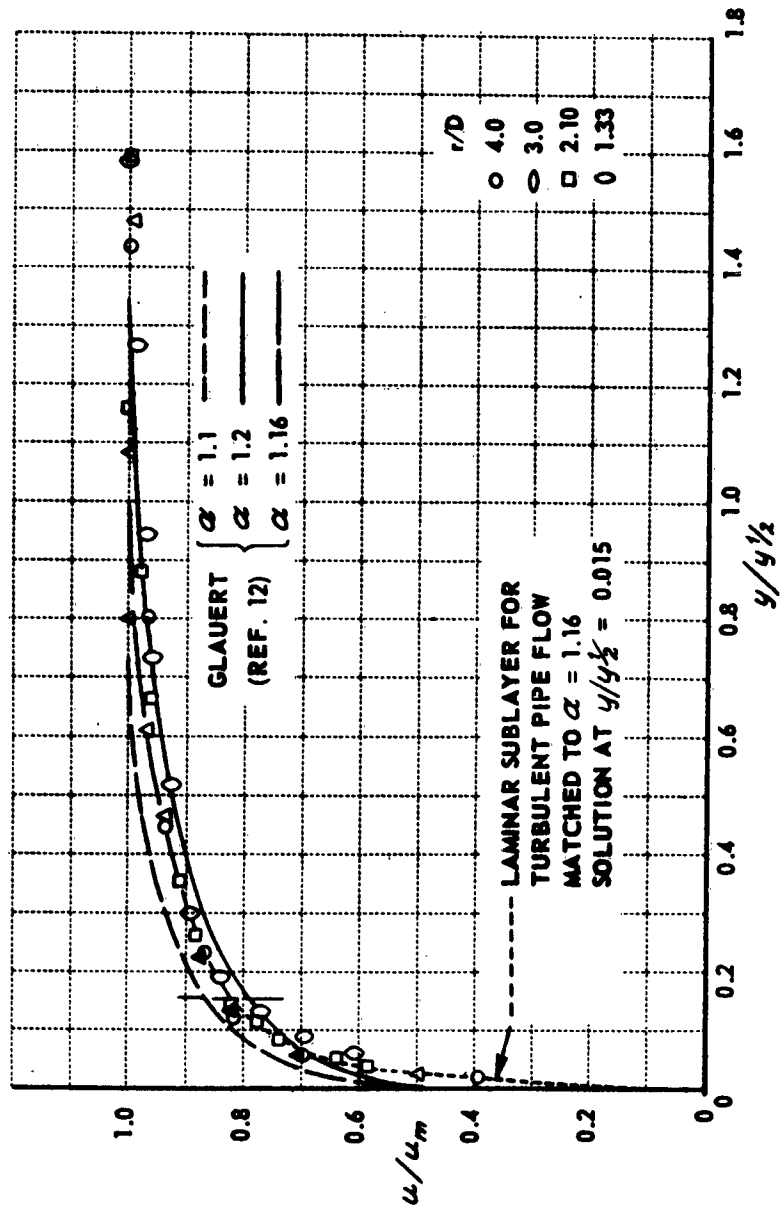


Figure 17(a). BOUNDARY LAYER VELOCITY PROFILES FOR $r/D > 1.0$
 $H/D = 0.25$, $U_\infty = 191$ FPS

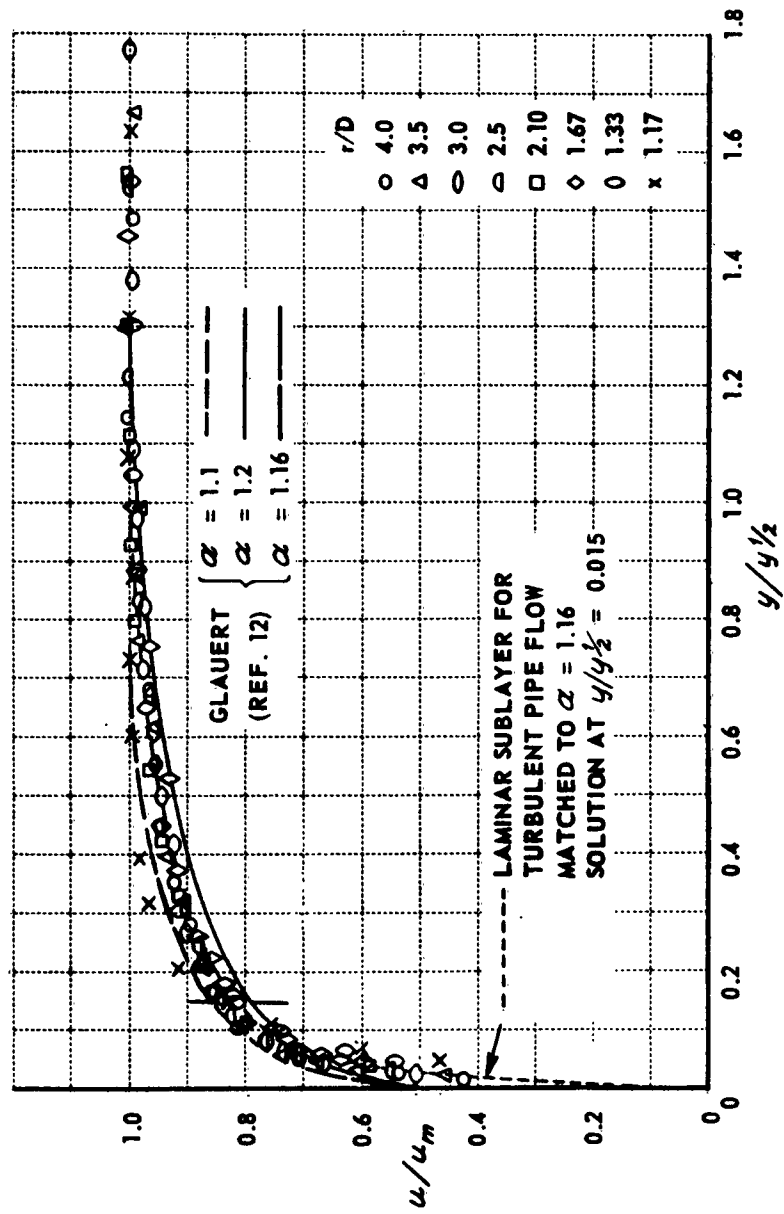


Figure 17(b). BOUNDARY LAYER VELOCITY PROFILES FOR $r/D > 1.0$
 $H/D = 0.50$, $U_\infty = 191$ FPS

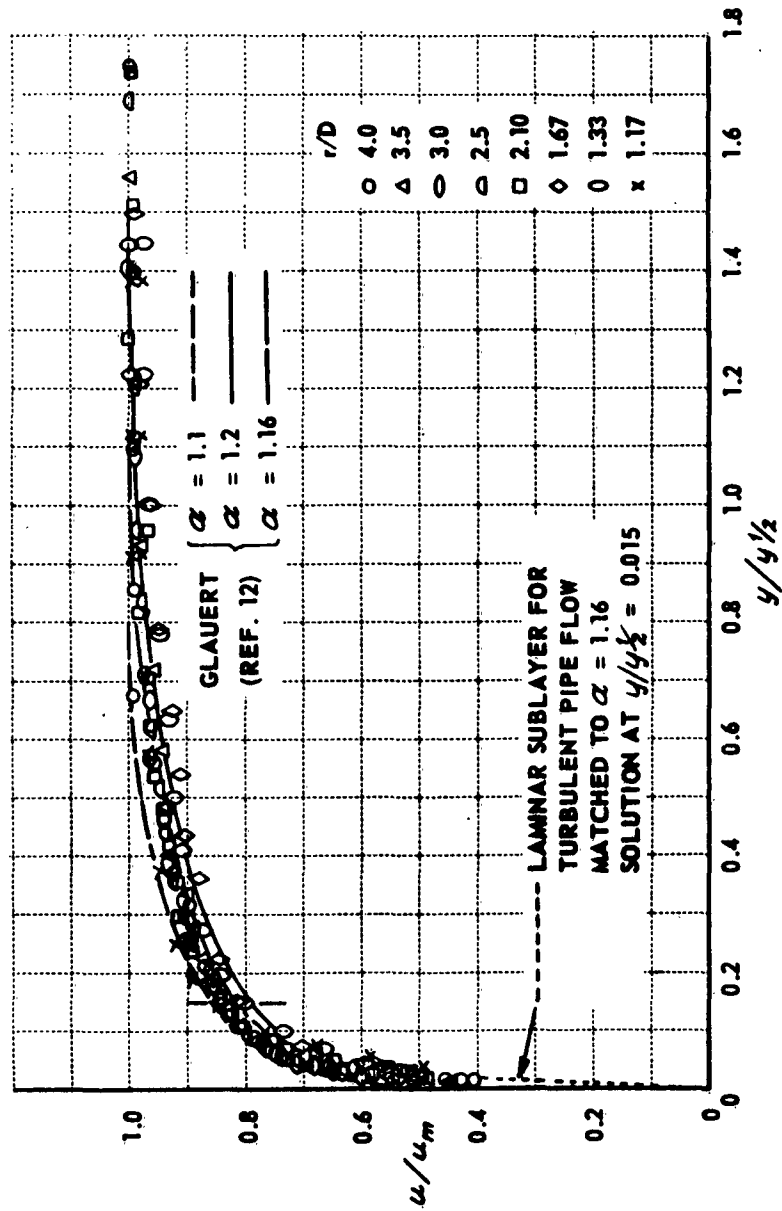


Figure 17(c). BOUNDARY LAYER VELOCITY PROFILES FOR $r/D > 1.0$

$H/D = 1.0$, $U_\infty = 191$ FPS

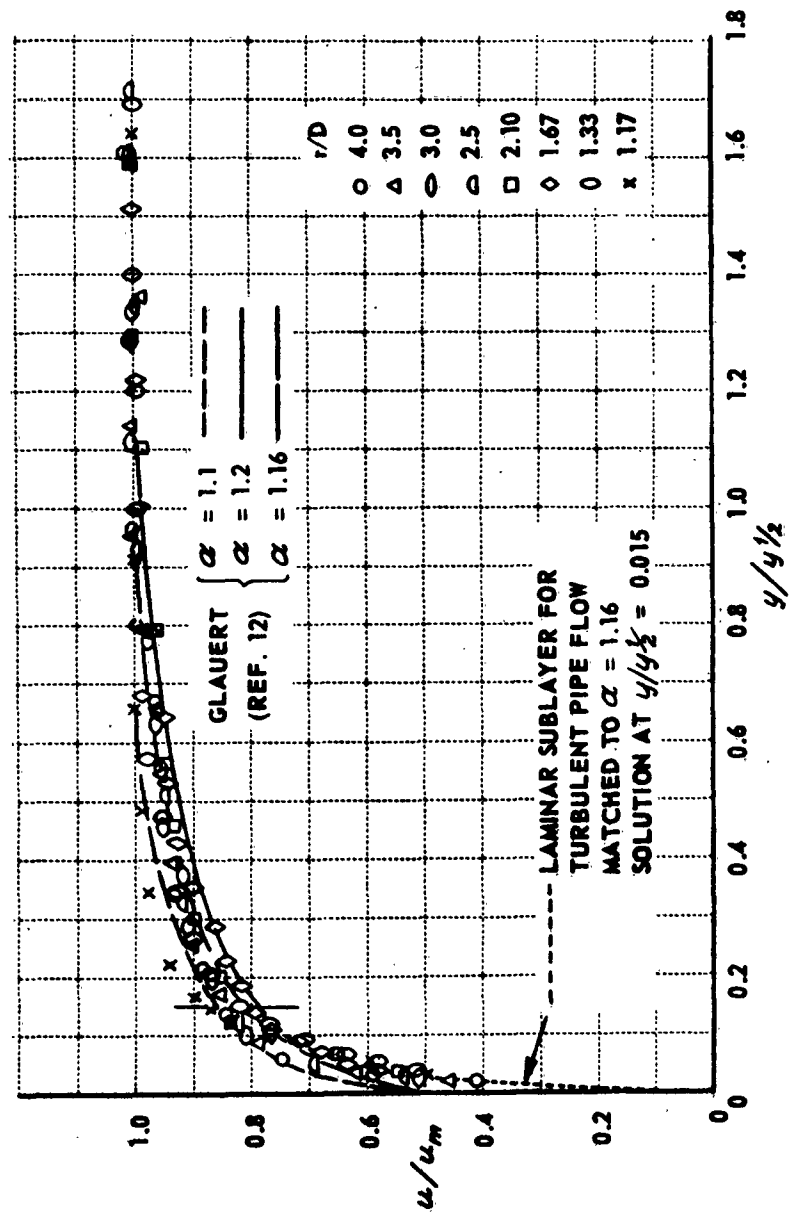


Figure 17(d). BOUNDARY LAYER VELOCITY PROFILES FOR $r/D > 1.0$
 $H/D = 2.0$, $U_\infty = 191$ FPS

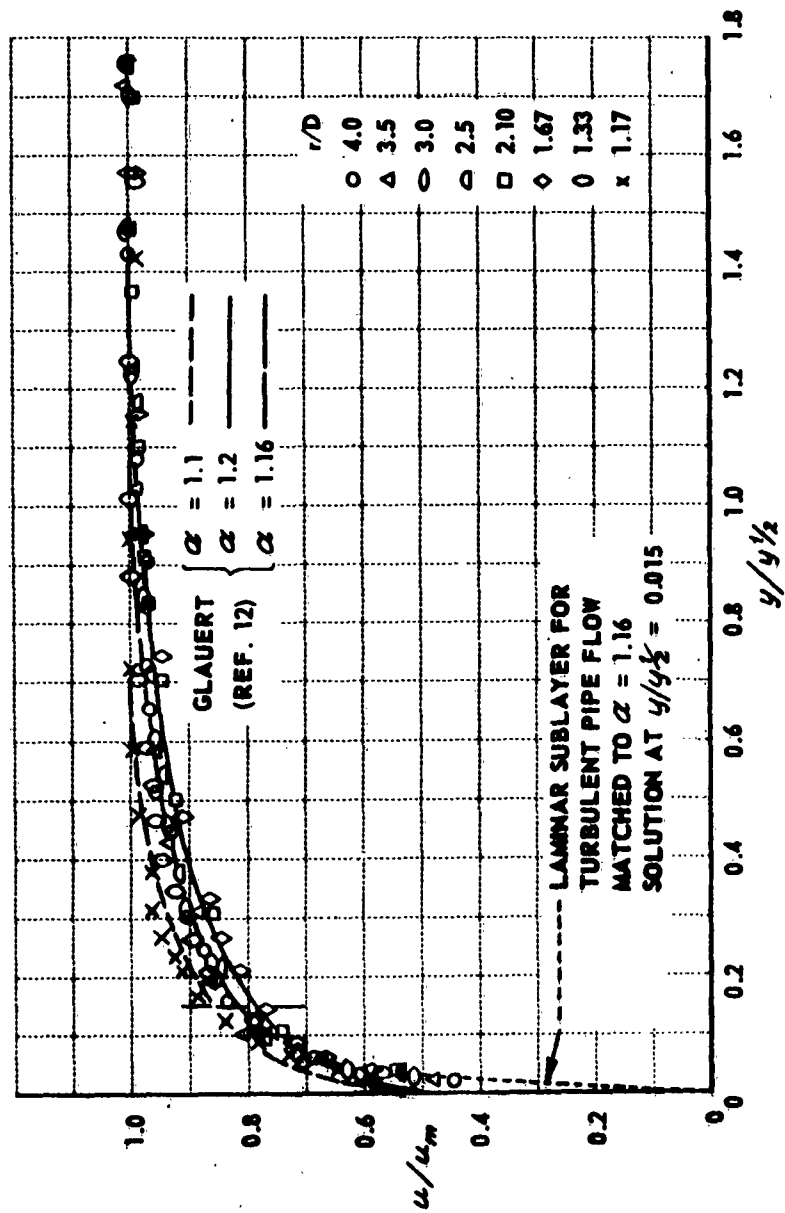


Figure 17(e). BOUNDARY LAYER VELOCITY PROFILES FOR $r/D > 1.0$
 $H/D = 4.0$, $U_\infty = 191$ FPS

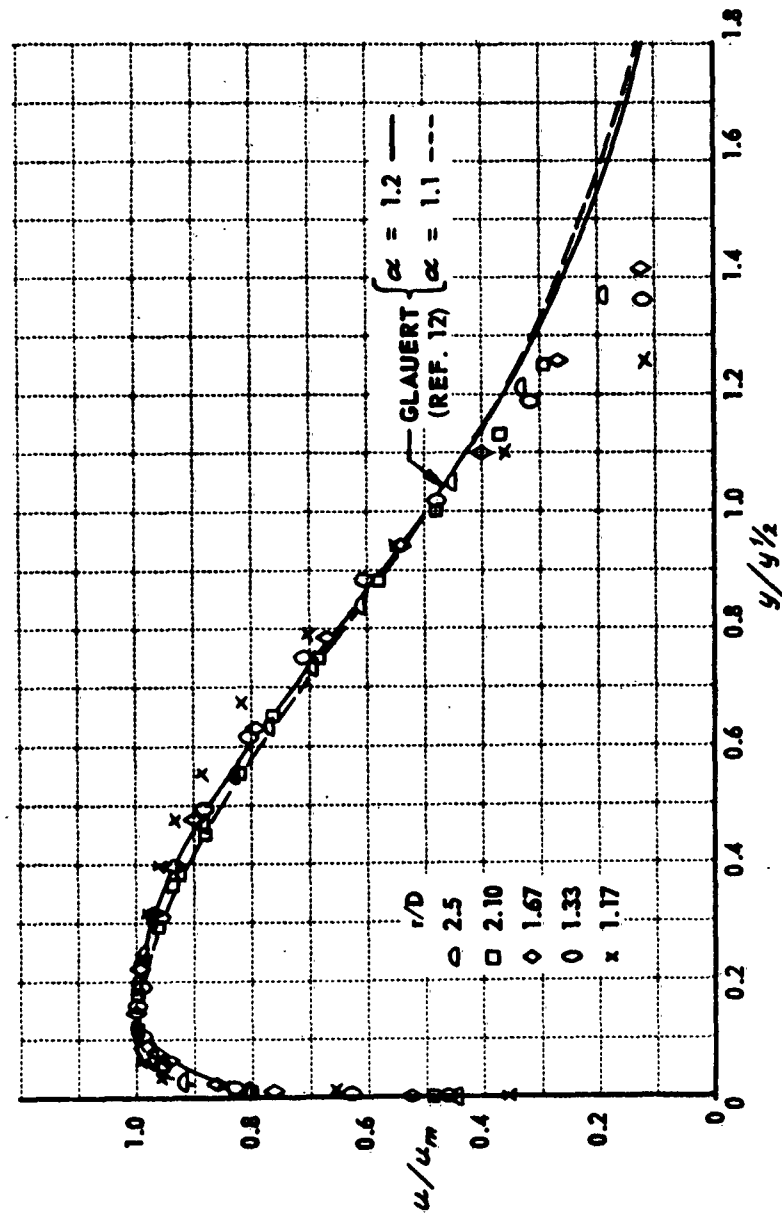


Figure 18(a). VELOCITY PROFILES NEAR THE GROUND FOR $r/D > 1.0$
 $H/D = 0.50, U_{\infty} = 121 \text{ FPS}$

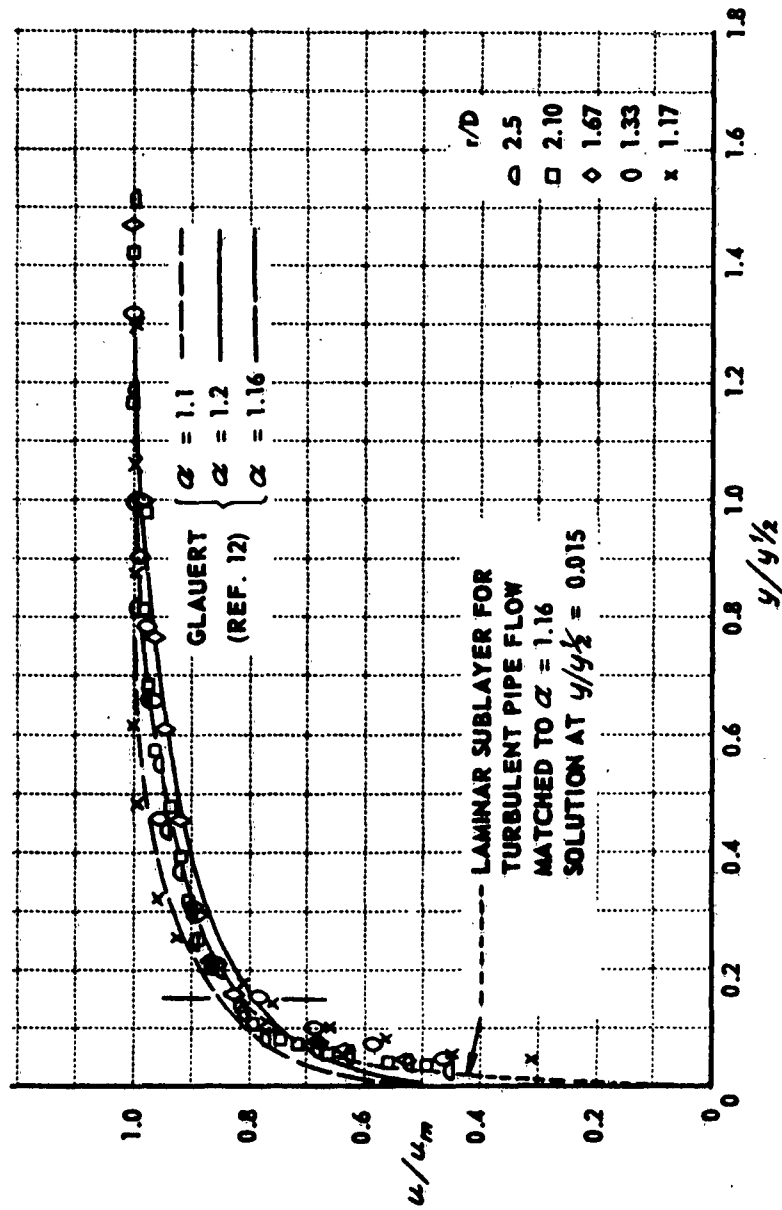
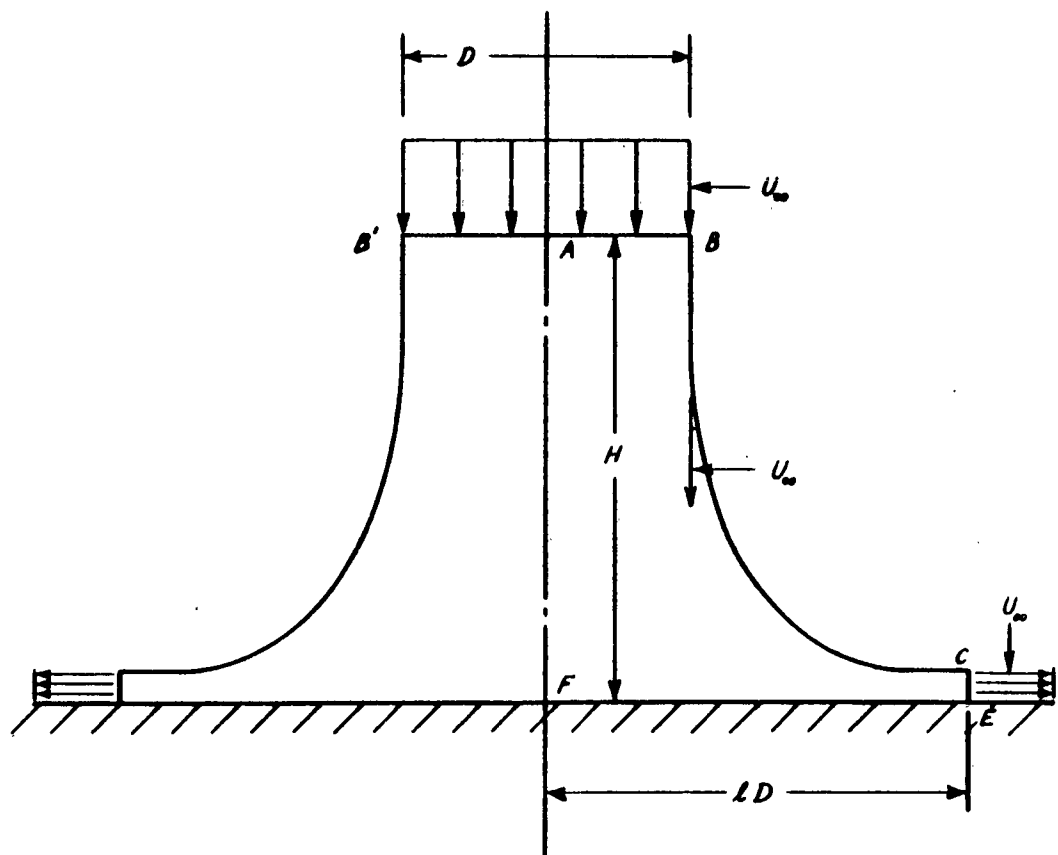


Figure 18(b). VELOCITY PROFILES NEAR THE GROUND FOR $r/D > 1.0$
 $H/D = 0.50, U_\infty = 121 \text{ FPS}$



**Figure 19. FLOW MODEL FOR CIRCULAR IMPINGING UNIFORM JET
USED IN REFERENCES 8, 9, AND 10**

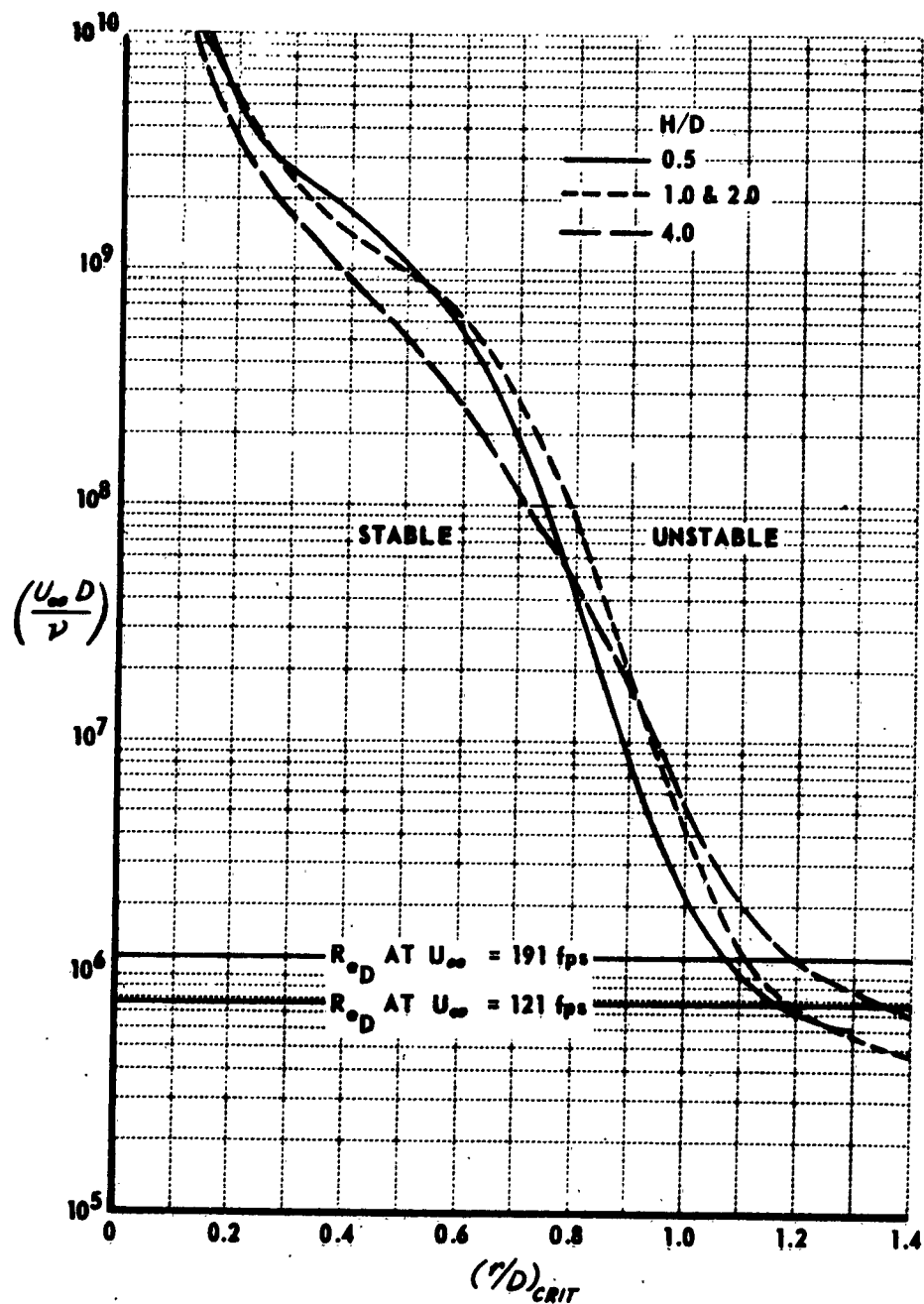


Figure 20. RADIAL POSITION OF THE POINT OF NEUTRAL STABILITY IN THE LAMINAR BOUNDARY LAYER VERSUS NOZZLE REYNOLDS NUMBER FOR VARIOUS VALUES OF H/D

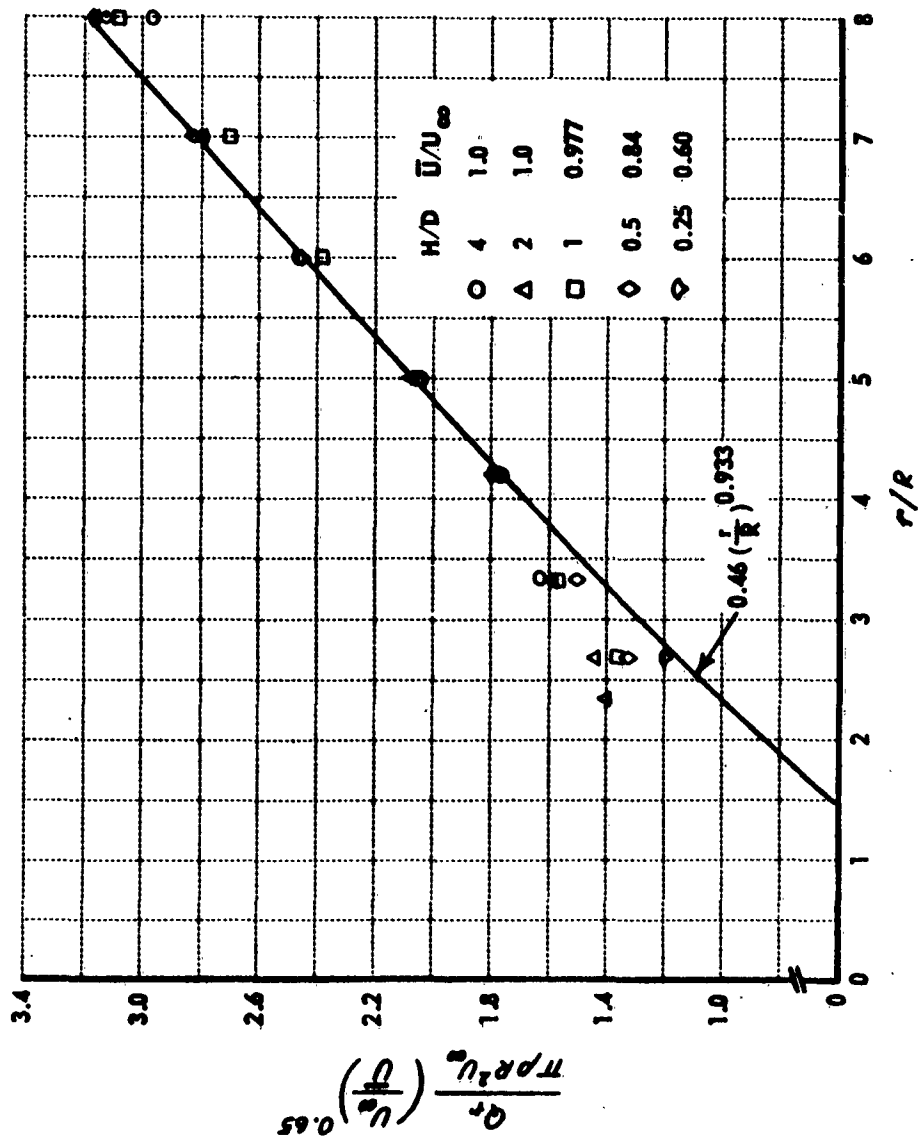


Figure 21. UNIVERSAL CURVE OF RADIAL MASS FLOW vs r/R

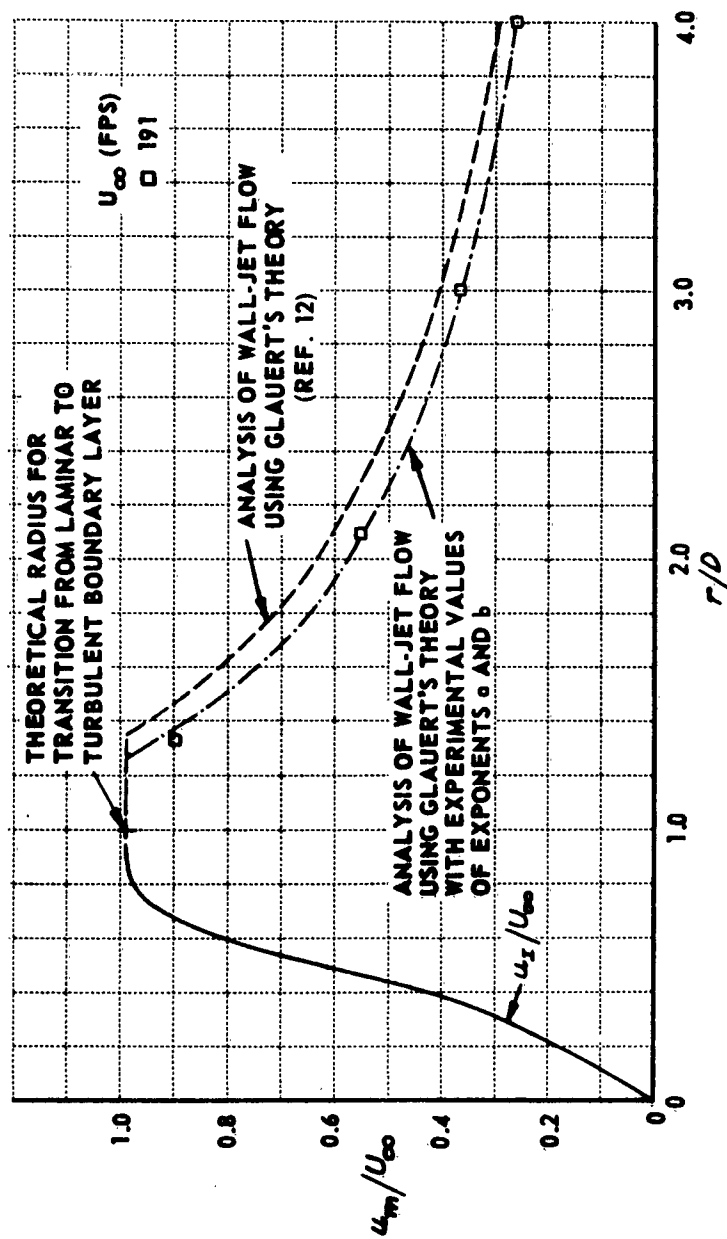


Figure 22(a). VARIATION OF EXPERIMENTAL MAXIMUM LOCAL VELOCITY NEAR THE GROUND WITH r/D COMPARED WITH THEORY FOR $H/D = 0.25$, $U_\infty = 191$ FPS

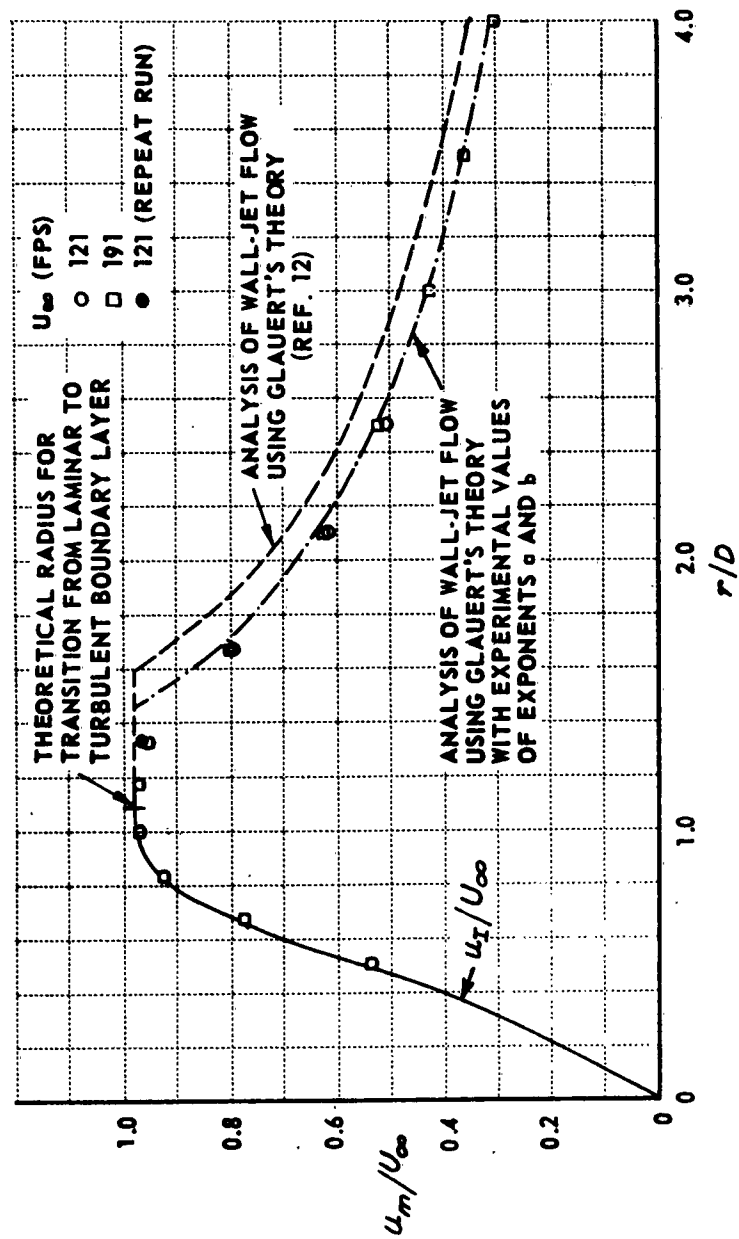


Figure 22(b). VARIATION OF EXPERIMENTAL MAXIMUM LOCAL VELOCITY NEAR THE GROUND WITH r/D COMPARED WITH THEORY FOR $h/D = 0.5$, $U_\infty = 191$ FPS

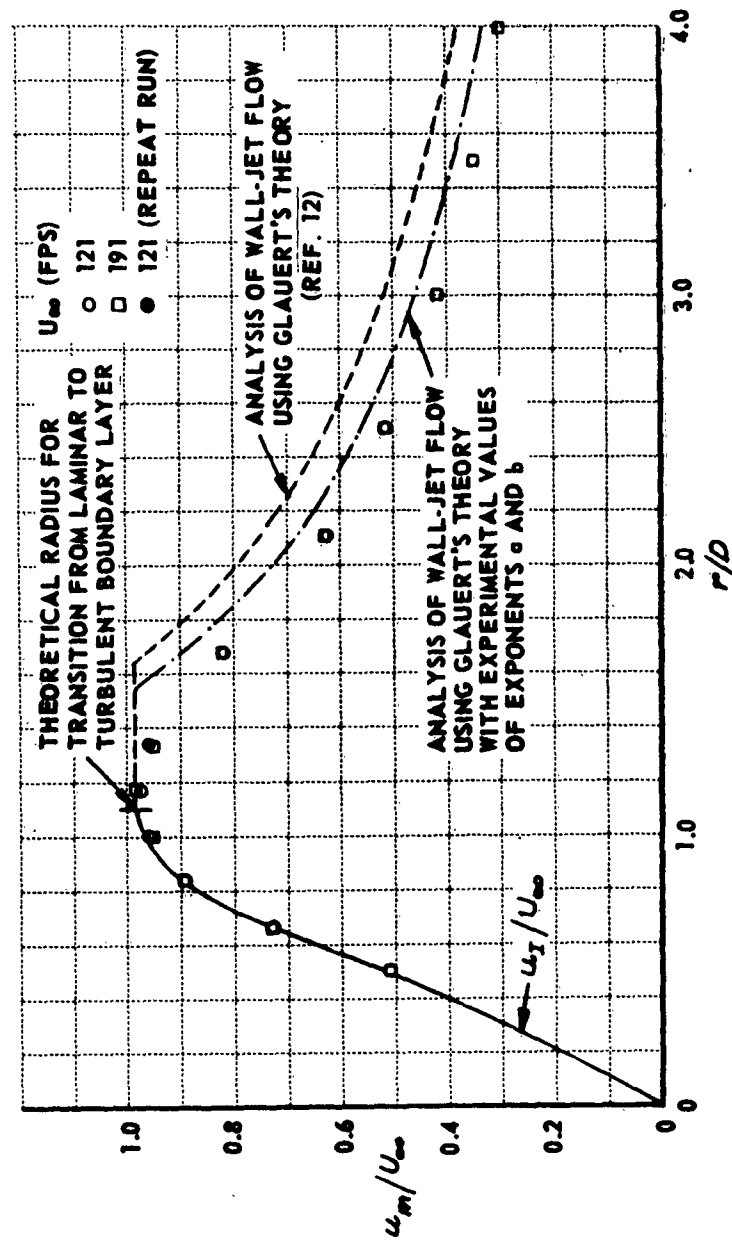


Figure 22(c). VARIATION OF EXPERIMENTAL MAXIMUM LOCAL VELOCITY NEAR THE GROUND WITH r/D COMPARED WITH THEORY FOR $H/D = 1.0$, $U_\infty = 191$ FPS

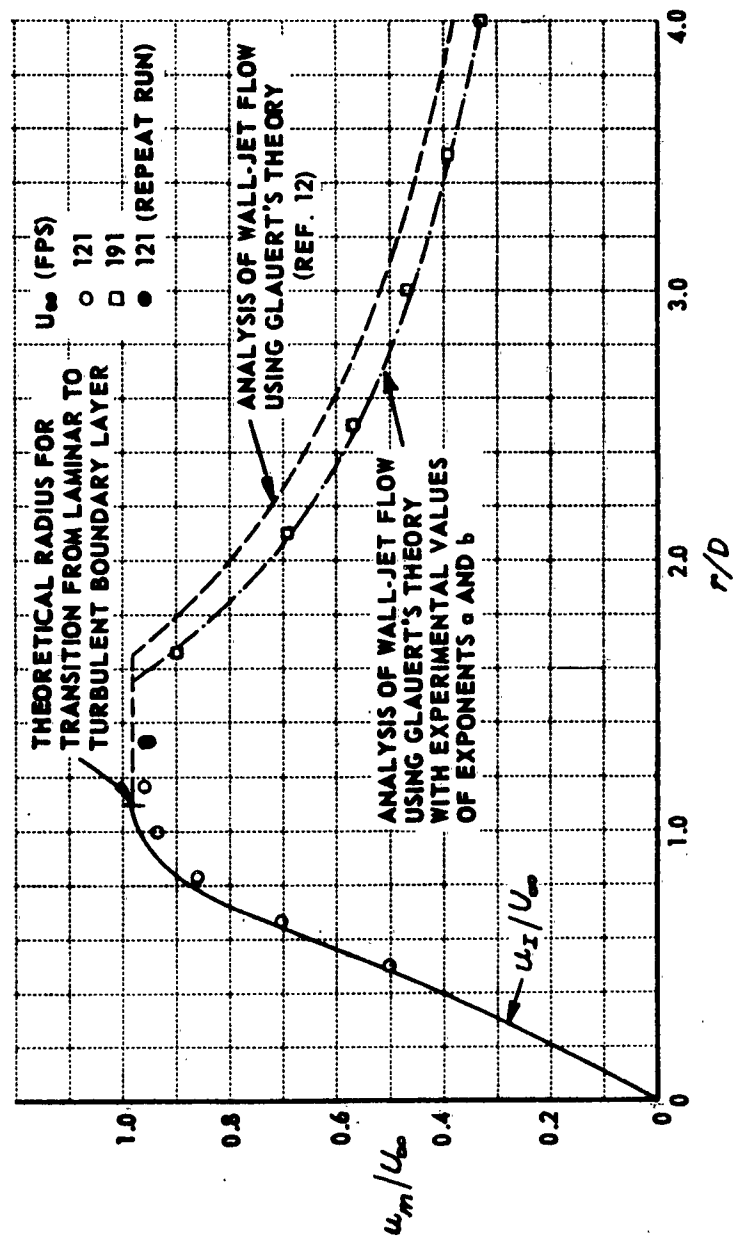


Figure 22(d). VARIATION OF EXPERIMENTAL MAXIMUM LOCAL VELOCITY NEAR THE GROUND WITH r/D COMPARED WITH THEORY FOR $H/D = 2.0$, $U_\infty = 191$ FPS

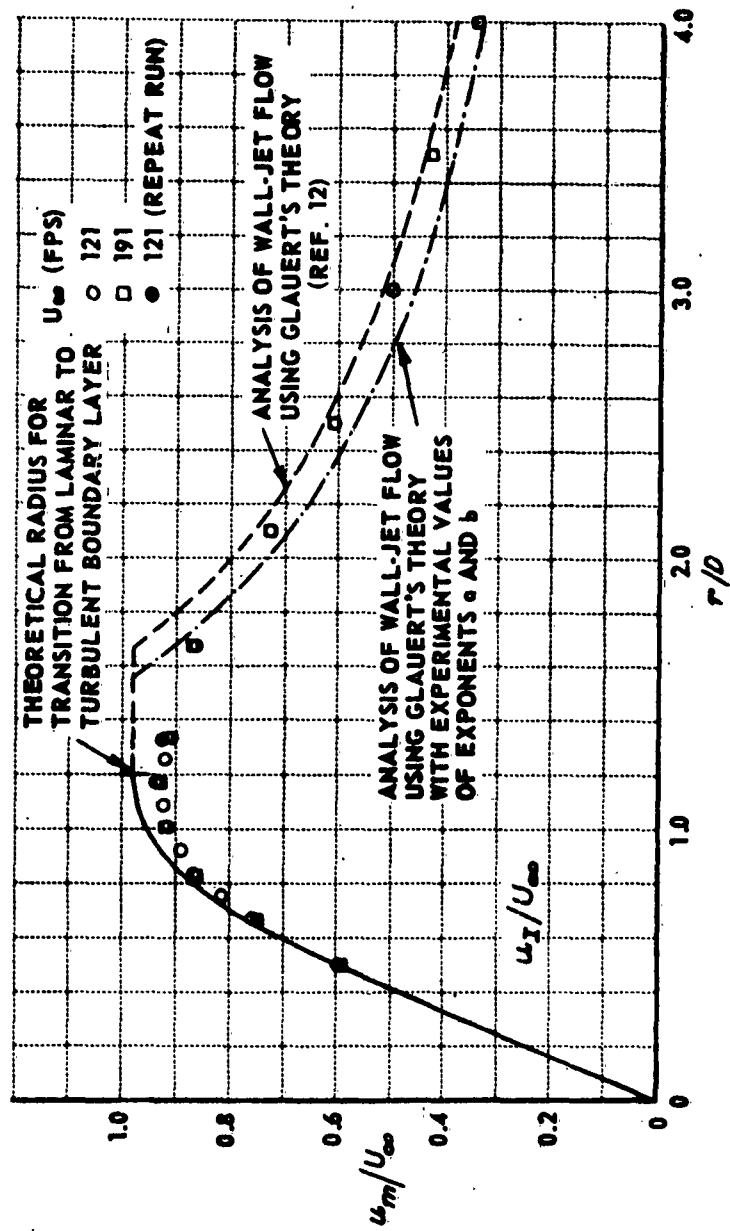


Figure 22(a). VARIATION OF EXPERIMENTAL MAXIMUM LOCAL VELOCITY NEAR THE GROUND WITH r/D COMPARED WITH THEORY FOR $H/D = 4.0$, $U_\infty = 191$ FPS

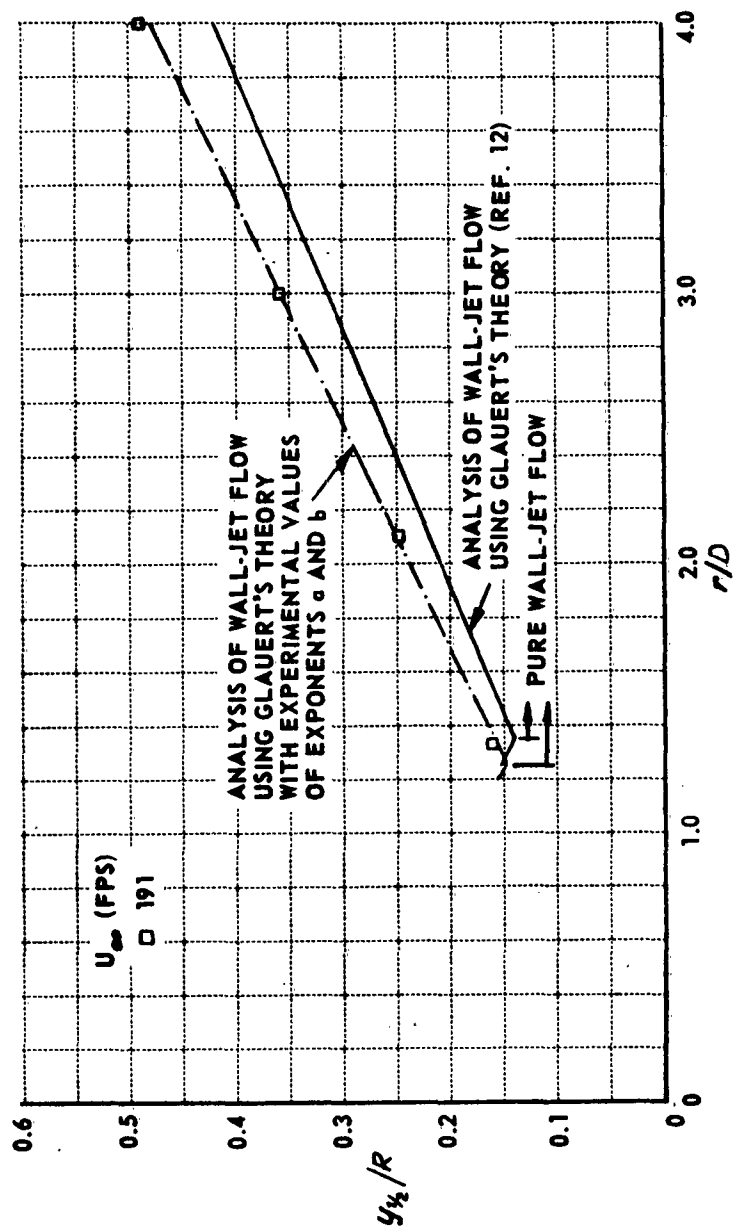


Figure 23(a). VARIATION OF EXPERIMENTAL VALUES OF $y_{1/2}/R$ WITH r/D COMPARED WITH THEORY FOR $H/D = 0.25$, $U_{\infty} = 191$ FPS

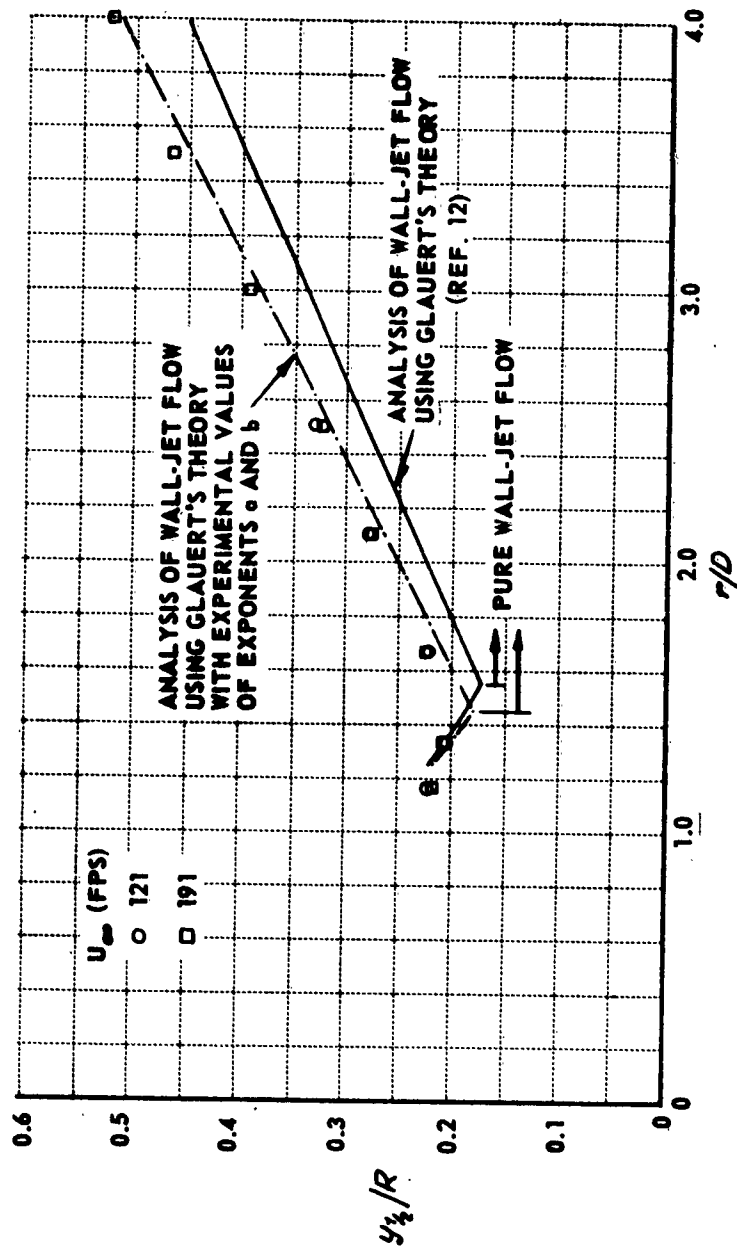


Figure 23(b). VARIATION OF EXPERIMENTAL VALUES OF $y_{1/2}/R$ WITH r/D COMPARED WITH THEORY FOR $H/D = 0.5$, $U_{\infty} = 191$ FPS

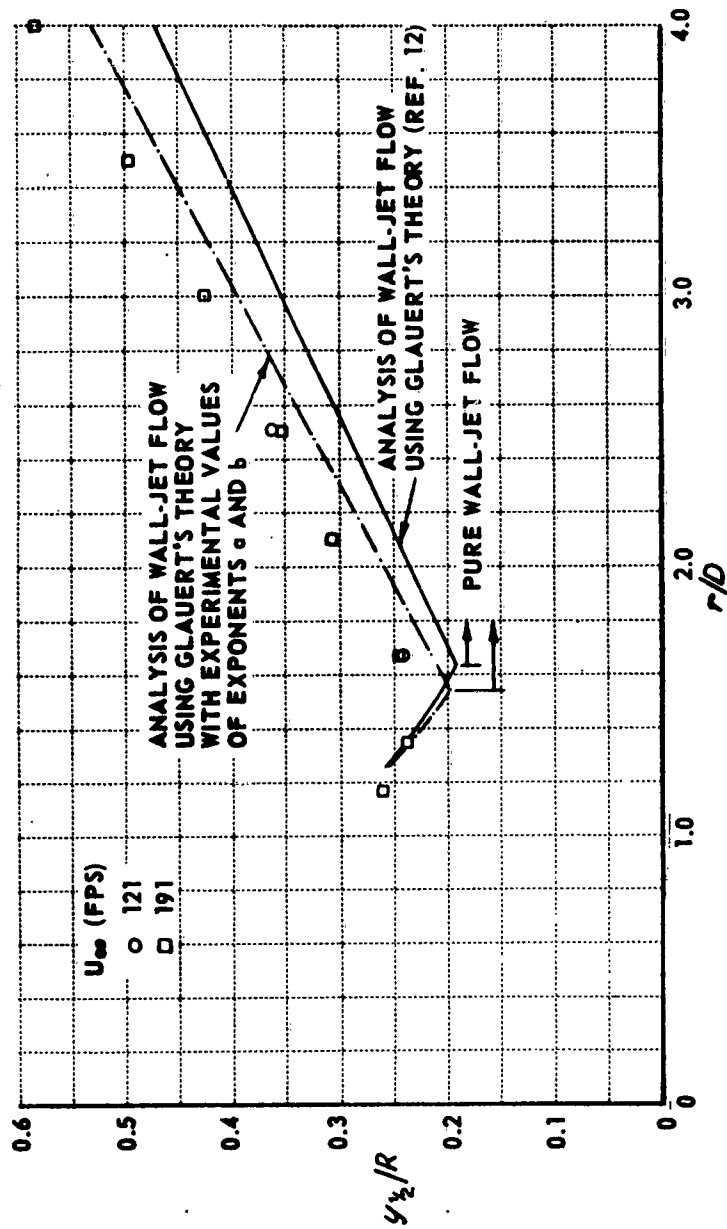


Figure 23(c). VARIATION OF EXPERIMENTAL VALUES OF $y_{1/2}/R$ WITH r/D COMPARED WITH THEORY FOR $H/D = 1.0$, $U_{\infty} = 191$ FPS

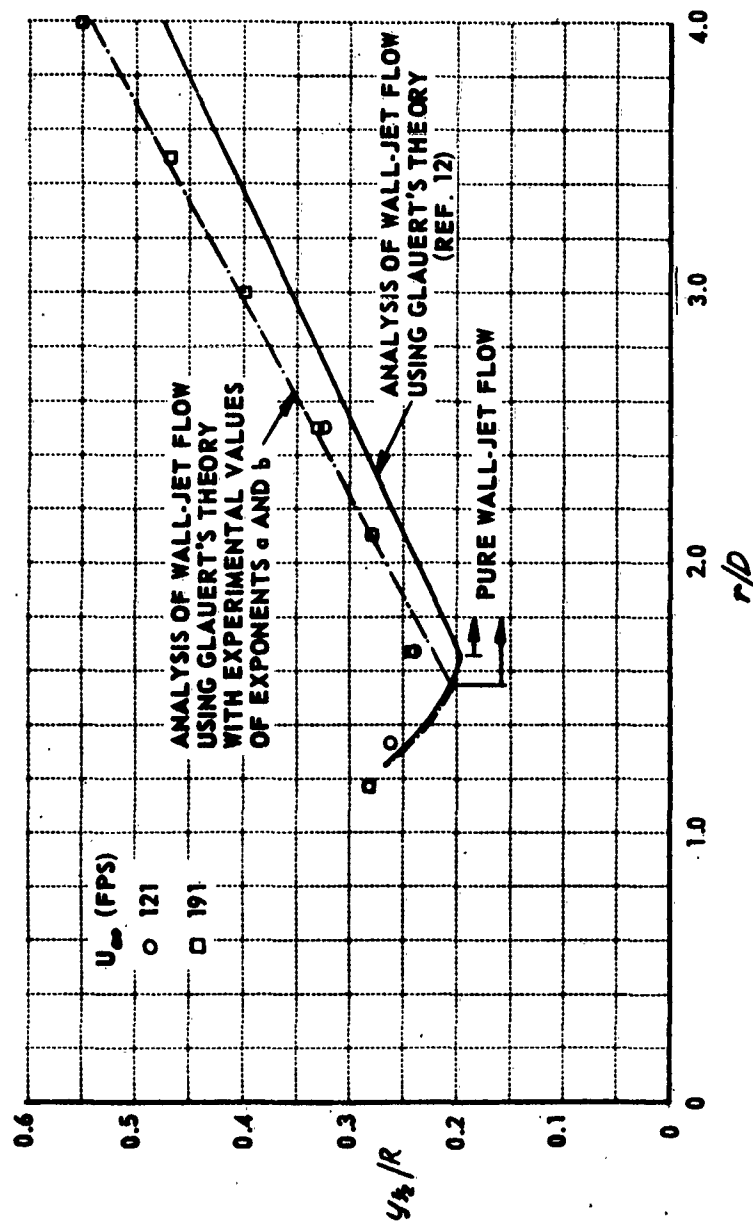


Figure 23(d). VARIATION OF EXPERIMENTAL VALUES OF $y_{1/2}/R$ WITH r/D COMPARED WITH THEORY FOR $H/D = 2.0$, $U_{\infty} = 191$ FPS

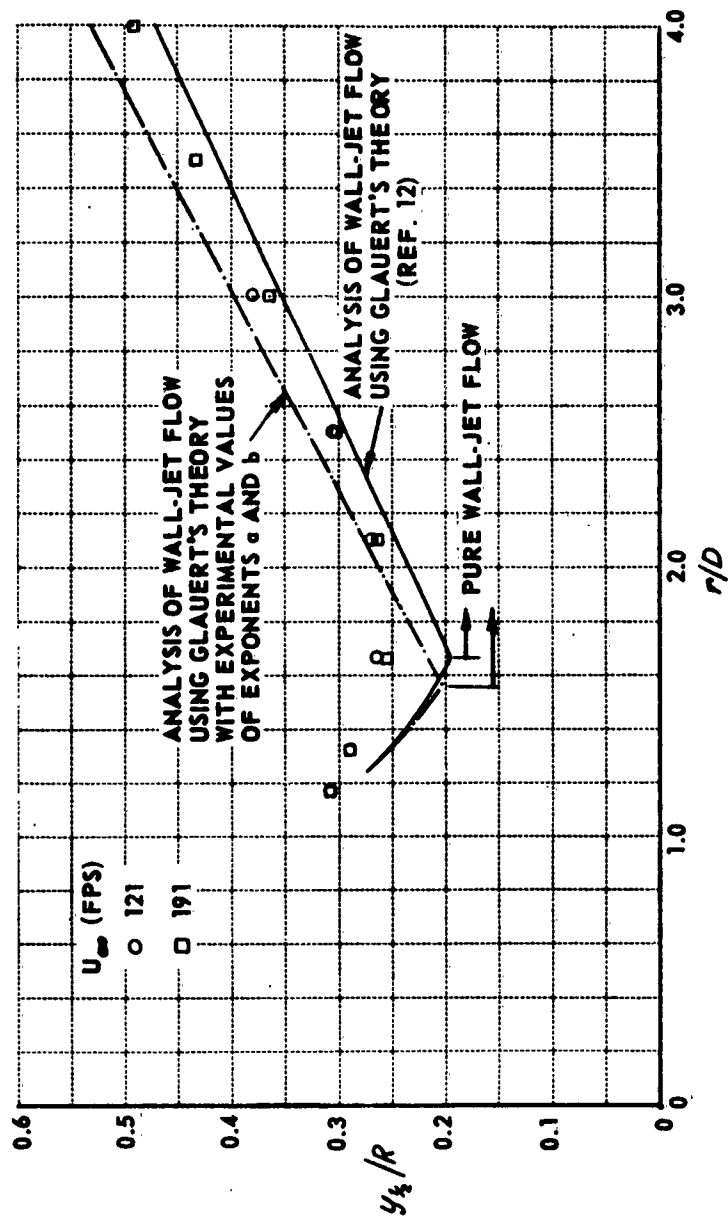


Figure 23(e). VARIATION OF EXPERIMENTAL VALUES OF y_k/R WITH r/D COMPARED WITH THEORY FOR $H/D = 4.0$, $U_\infty = 191$ FPS

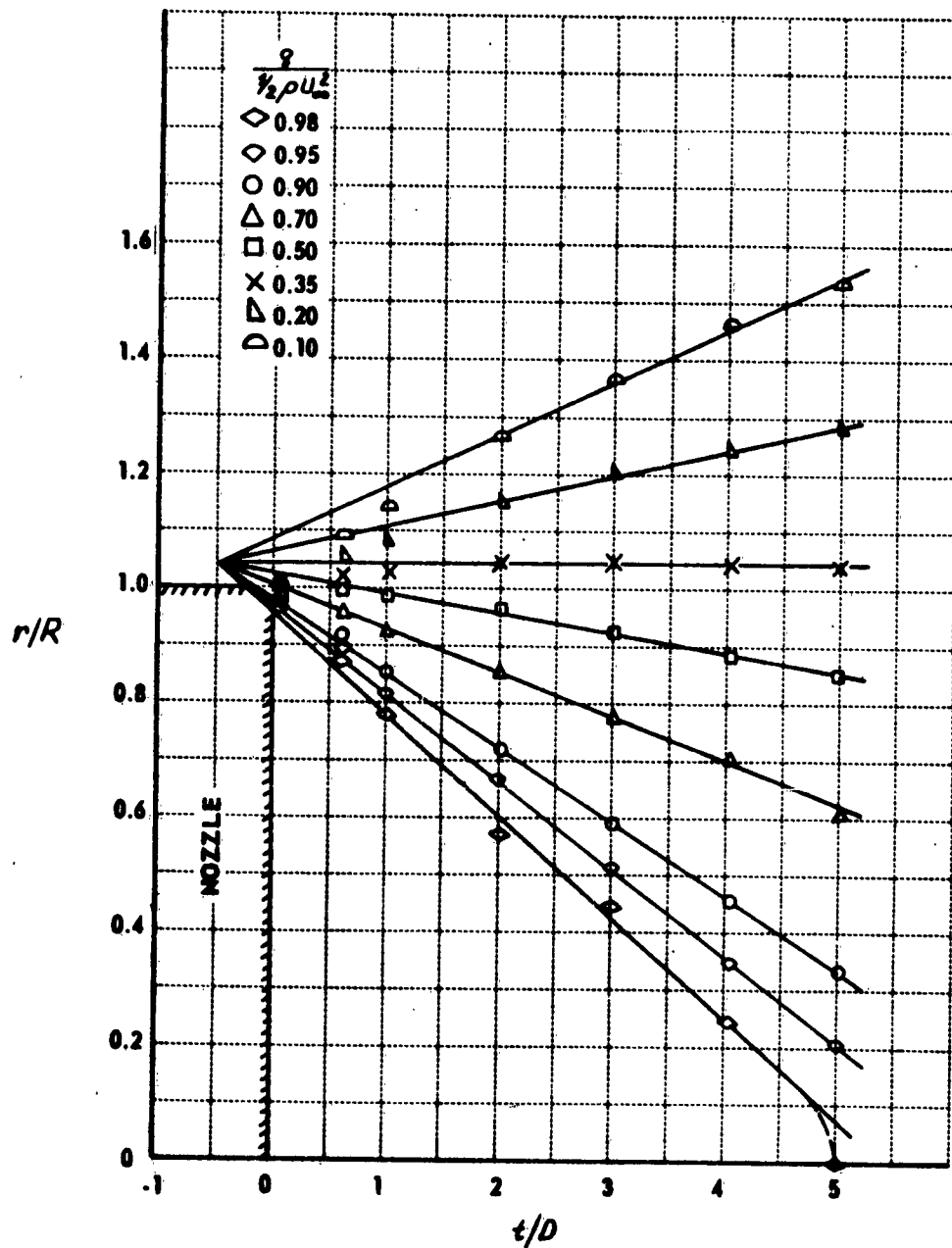


Figure 24. LINES OF CONSTANT DYNAMIC PRESSURE IN MIXING REGION SURROUNDING THE POTENTIAL CORE OF THE FREE JET

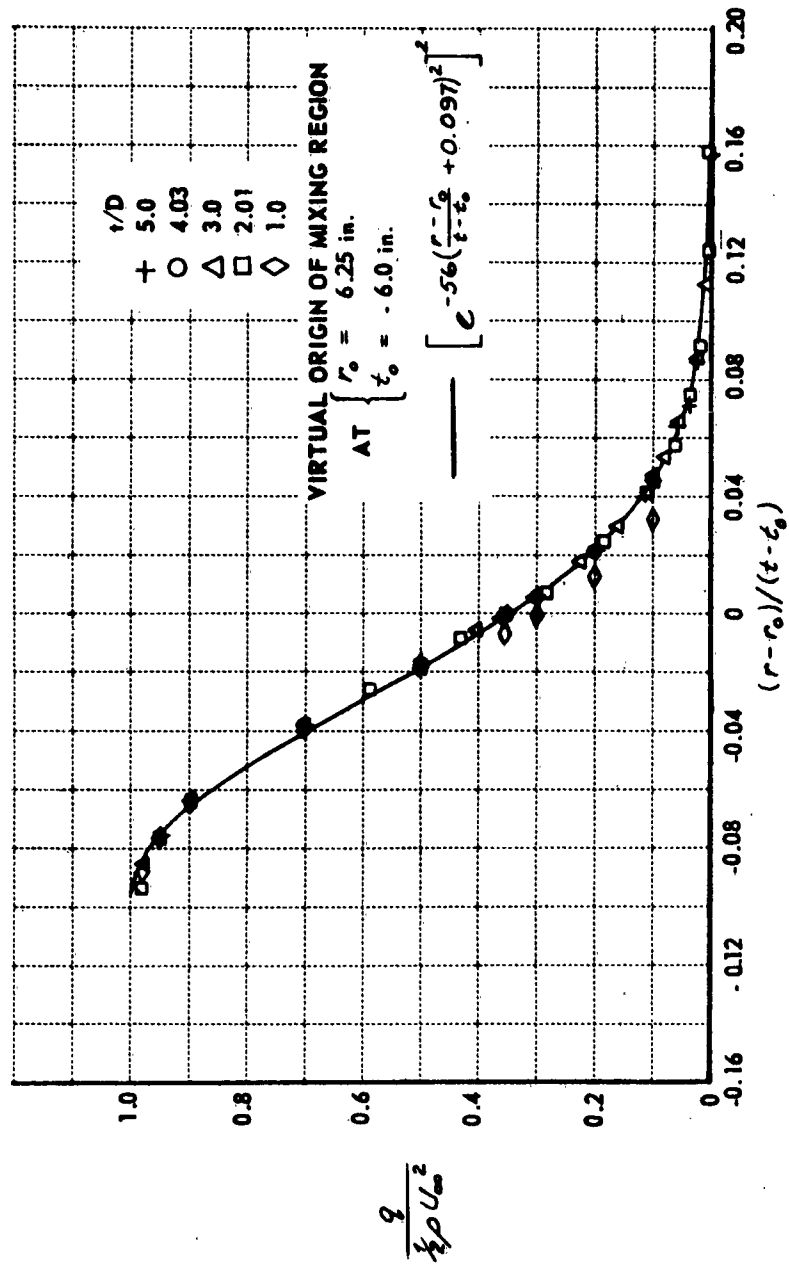


Figure 25. EXPERIMENTAL CURVE OF DYNAMIC PRESSURE IN MIXING REGION
 SURROUNDING THE POTENTIAL CORE OF THE FREE JET, $U_{\infty} = 121 \text{ FPS}$

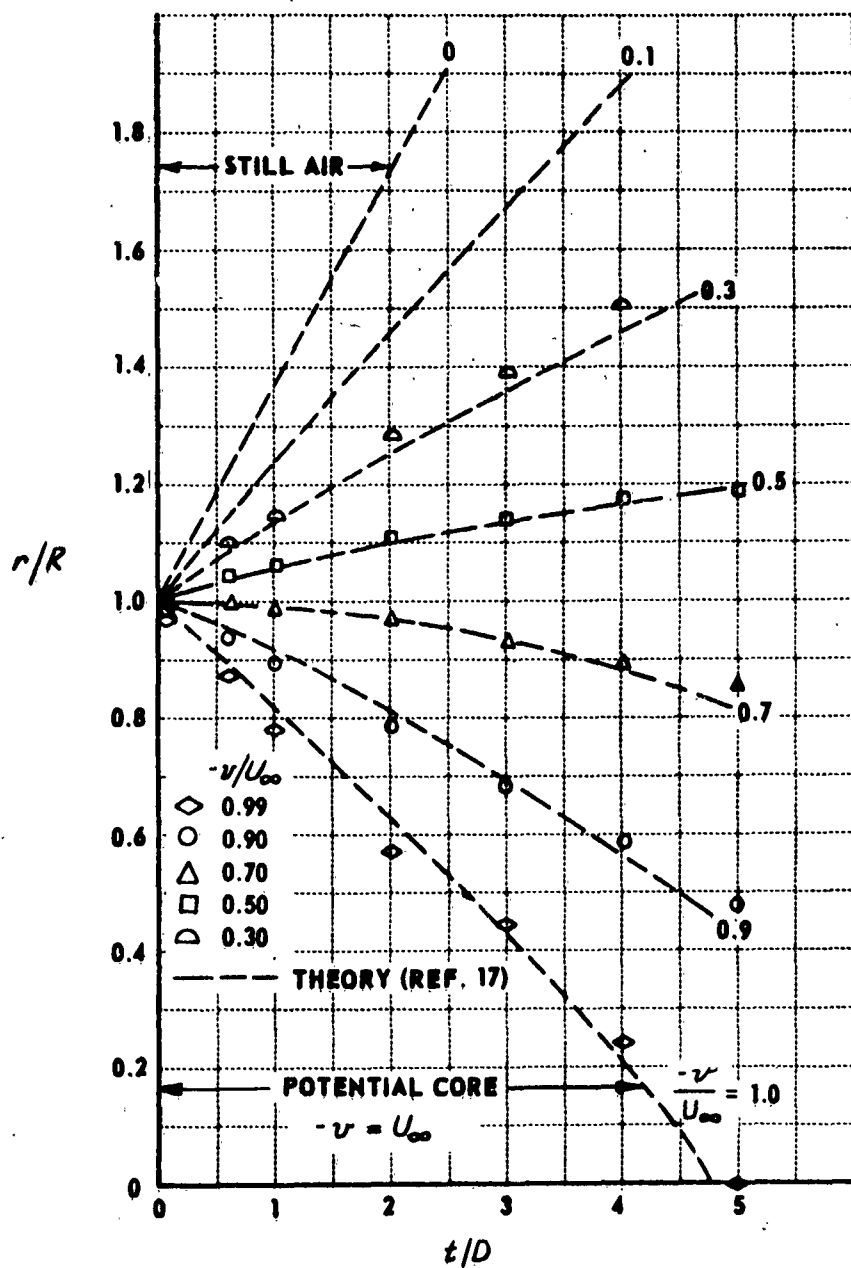


Figure 26. CONSTANT VELOCITY CONTOURS IN MIXING REGION SURROUNDING THE POTENTIAL CORE OF THE FREE JET

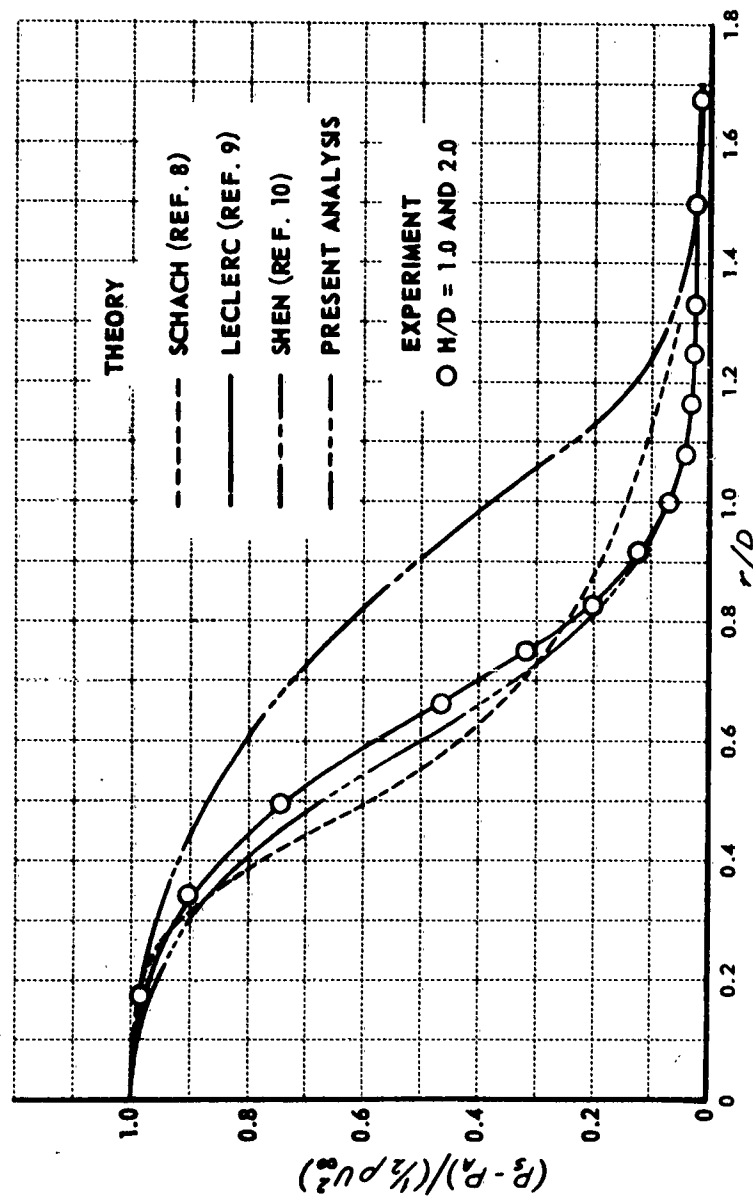


Figure 27. COMPARISON OF PREDICTED AND EXPERIMENTAL GROUND-PLANE STATIC PRESSURE DISTRIBUTIONS - $H/D = 1.0$ TO 2.0

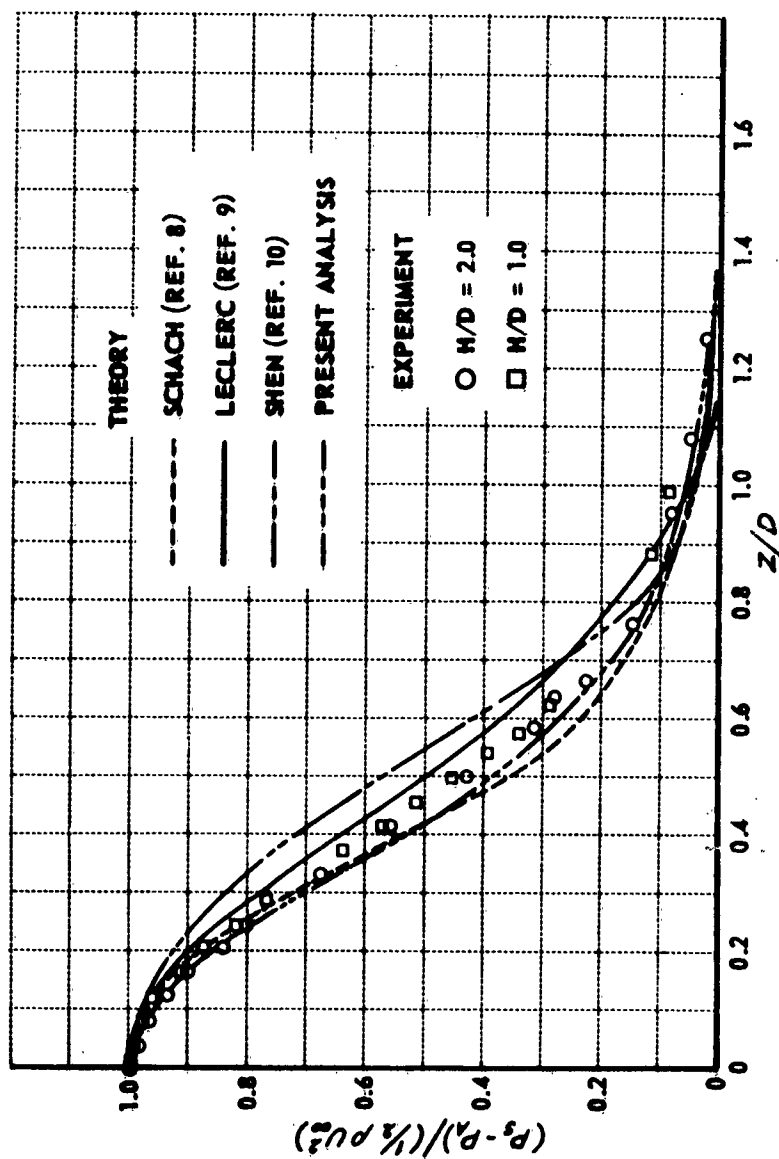


Figure 28. COMPARISON OF PREDICTED AND EXPERIMENTAL JET-CENTERLINE
STATIC PRESSURE DISTRIBUTIONS - $H/D = 1.0$ TO 2.0

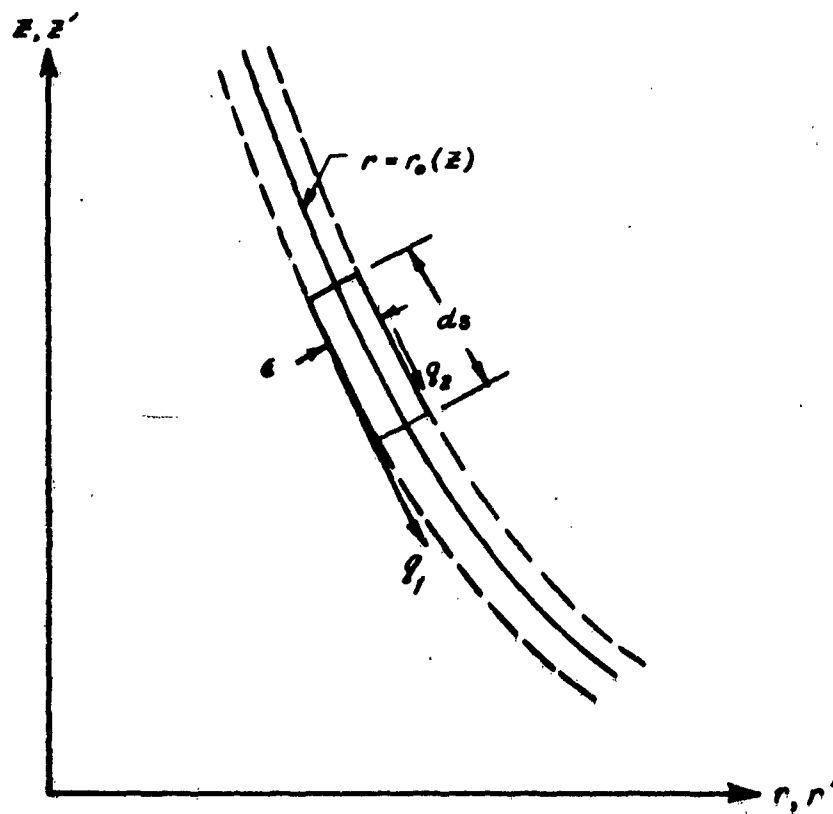


Figure 29. REPRESENTATION OF VORTICITY LAYER ON EDGE OF INVISCID JET

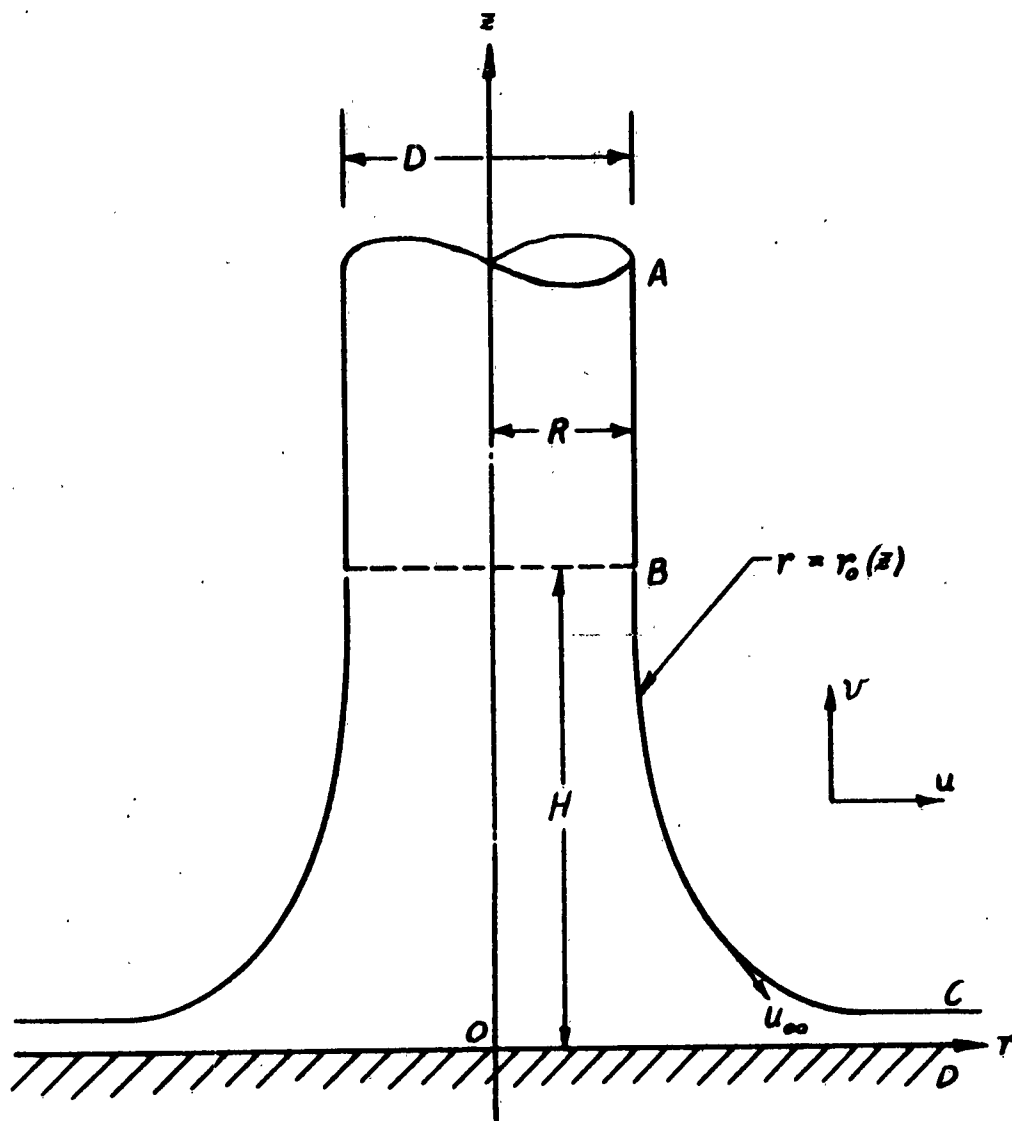


Figure 30. FLOW MODEL USED IN PRESENT ANALYSIS FOR CIRCULAR IMPINGING UNIFORM JET

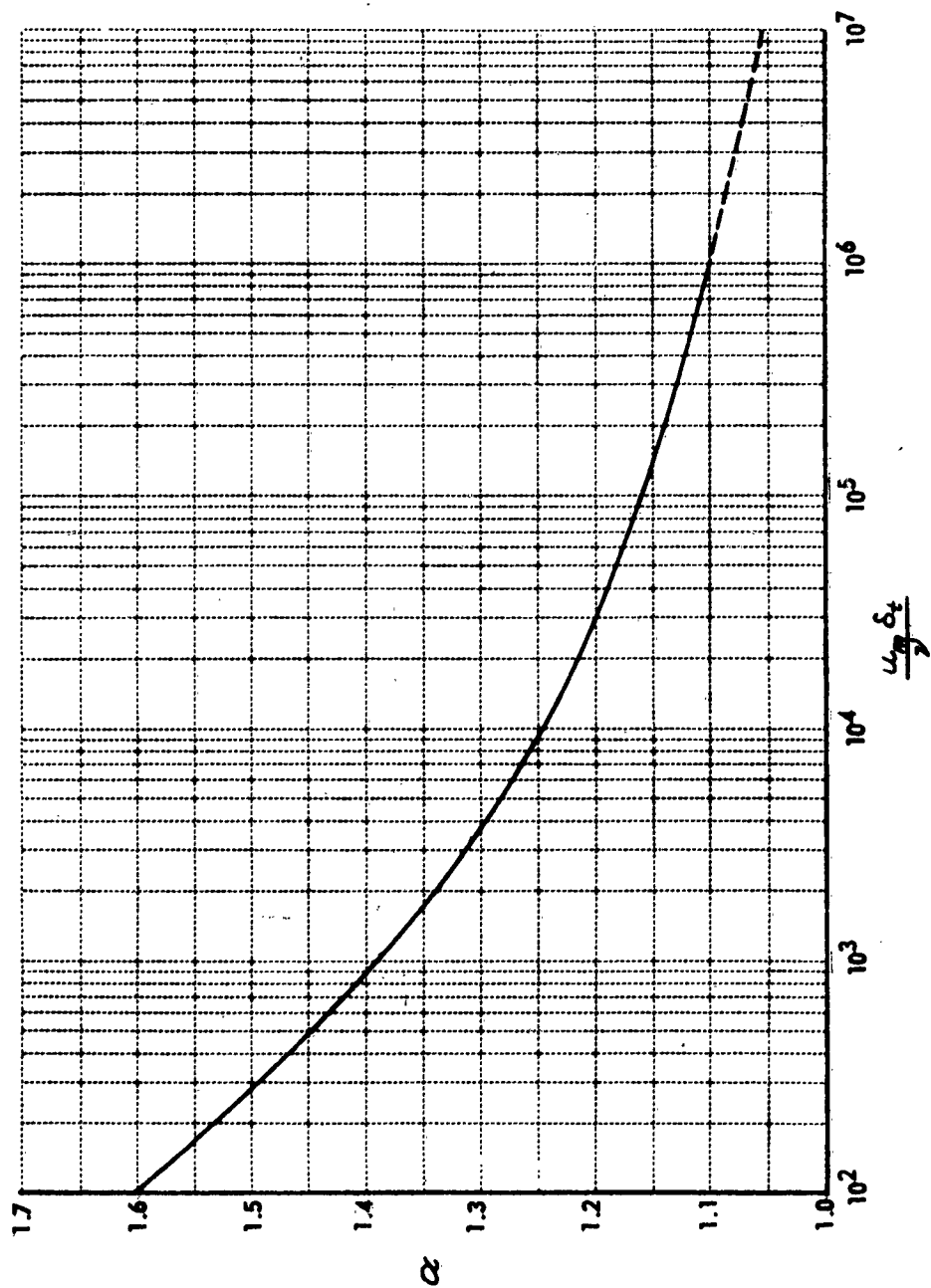


Figure 31. VARIATION OF GLAUERT'S PARAMETER α vs $\frac{u_{\infty} \delta_t}{\nu}$
 $\kappa = 0.013$

DISTRIBUTION

U. S. Army Aviation Test Board	1
Aviation Test Office, Edwards AFB, Calif.	1
The Research Analysis Corporation	1
Army Research Office, Durham, N. C.	2
Office of Chief of R&D, DA	1
Army Research Office, DA	1
U. S. Army Communications-Electronics Combat Developments Agency	1
U. S. Army Aviation and Surface Materiel Command	1
U. S. Army Transportation School	3
U. S. Army Transportation Research Command	77
Air University Library	1
ASD (ASRMPT), Wright-Patterson AFB, Ohio	1
Bureau of Naval Weapons, DN	1
U. S. Naval Postgraduate School	1
David Taylor Model Basin	1
National Aviation Facilities Experimental Center	3
Langley Research Center, NASA	2
George C. Marshall Space Flight Center, NASA	1
Manned Spacecraft Center, NASA	1
Ames Research Center, NASA	2
Lewis Research Center, NASA	1
Scientific and Technical Information Facility	1
U. S. Government Printing Office	1
Armed Services Technical Information Agency	10
U. S. Patent Office	1
Flight Control Laboratory, Air Force Systems Command	1
U. S. Army Materiel Command	1
U. S. Army Mobility Command	1

AD	<p>Cornell Aeronautical Laboratory, Inc., Buffalo, N. Y. THEORETICAL AND EXPERIMENTAL STUDIES OF IMPINGING UNIFORM JETS - W. Gordon Brady and Gary R. Ludwig, TRECOM Technical Report 63-11, CAL Report BB-1657-S-1, April 1963, 105 pp., incl. illus., 19 refs. (Contract DA 44-177-TC-782) USATRECOM Task 9R38-01-017-29.</p> <p>Unclassified Report</p> <p>The flow field under a uniform circular jet perpendicular to and impinging on the ground was studied experimentally and theoretically in order to further the understanding of the aero- dynamic processes associated with ground particle entrainment in the impinging downwash from VTOL aircraft.</p> <p>Experimental data have been obtained for the flow in the deflected jet and in the ground boundary layer for jet height-to-nozzle diameter ratios (H/D) from 0.25 to 4 and for two mass flows. The boundary layer measurements were obtained at radial stations between one-half and four nozzle diameters from the stagnation point.</p> <p>The flow field of an inviscid uniform jet perpendicular to the ground was analyzed theoretically, based on a vortex sheet model, and partial results obtained. Boundary layer analyses were performed for the laminar region which occurs up to approximately one jet diameter from the stagnation point and for the region beyond two jet diameters from the stagnation point where the flow is of the wall-jet type. These two regions were joined by means of a semi- empirical analyses based on an assumption as to loss in momentum flux in the transition zone joining the laminar boundary layer and the wall-jet flow. Comparisons between the results of the theoretical analyses and the experimental results are made.</p>	<p>UNCLASSIFIED</p> <p>1. Vertical Takeoff Planes 2. Downwash Impingement</p> <p>I U.S. Army Transportation Research Command, Ft. Eustis, Va. II Cornell Aeronautical Laboratory, Inc., Buffalo, N. Y. Contract DA 44-177-TC-782 Brady, W. Gordon Ludwig, Gary R.</p>	<p>UNCLASSIFIED</p> <p>1. Vertical Takeoff Planes 2. Downwash Impingement</p> <p>I U.S. Army Transportation Research Command, Ft. Eustis, Va. II Cornell Aeronautical Laboratory, Inc., Buffalo, N. Y. Contract DA 44-177-TC-782 Brady, W. Gordon Ludwig, Gary R.</p>
AD	<p>Cornell Aeronautical Laboratory, Inc., Buffalo, N. Y. THEORETICAL AND EXPERIMENTAL STUDIES OF IMPINGING UNIFORM JETS - W. Gordon Brady and Gary R. Ludwig, TRECOM Technical Report 63-11, CAL Report BB-1657-S-1, April 1963, 105 pp., incl. illus., 19 refs. (Contract DA 44-177-TC-782) USATRECOM Task 9R38-01-017-29.</p> <p>Unclassified Report</p> <p>The flow field under a uniform circular jet perpendicular to and impinging on the ground was studied experimentally and theoretically in order to further the understanding of the aero- dynamic processes associated with ground particle entrainment in the impinging downwash from VTOL aircraft.</p> <p>Experimental data have been obtained for the flow in the deflected jet and in the ground boundary layer for jet height-to-nozzle diameter ratios (H/D) from 0.25 to 4 and for two mass flows. The boundary layer measurements were obtained at radial stations between one-half and four nozzle diameters from the stagnation point.</p> <p>The flow field of an inviscid uniform jet perpendicular to the ground was analyzed theoretically, based on a vortex sheet model, and partial results obtained. Boundary layer analyses were performed for the laminar region which occurs up to approximately one jet diameter from the stagnation point and for the region beyond two jet diameters from the stagnation point where the flow is of the wall-jet type. These two regions were joined by means of a semi- empirical analyses based on an assumption as to loss in momentum flux in the transition zone joining the laminar boundary layer and the wall-jet flow. Comparisons between the results of the theoretical analyses and the experimental results are made.</p>	<p>UNCLASSIFIED</p> <p>1. Vertical Takeoff Planes 2. Downwash Impingement</p> <p>I U.S. Army Transportation Research Command, Ft. Eustis, Va. II Cornell Aeronautical Laboratory, Inc., Buffalo, N. Y. Contract DA 44-177-TC-782 Brady, W. Gordon Ludwig, Gary R.</p>	<p>UNCLASSIFIED</p> <p>1. Vertical Takeoff Planes 2. Downwash Impingement</p> <p>I U.S. Army Transportation Research Command, Ft. Eustis, Va. II Cornell Aeronautical Laboratory, Inc., Buffalo, N. Y. Contract DA 44-177-TC-782 Brady, W. Gordon Ludwig, Gary R.</p>
AD	<p>Cornell Aeronautical Laboratory, Inc., Buffalo, N. Y. THEORETICAL AND EXPERIMENTAL STUDIES OF IMPINGING UNIFORM JETS - W. Gordon Brady and Gary R. Ludwig, TRECOM Technical Report 63-11, CAL Report BB-1657-S-1, April 1963, 105 pp., incl. illus., 19 refs. (Contract DA 44-177-TC-782) USATRECOM Task 9R38-01-017-29.</p> <p>Unclassified Report</p> <p>The flow field under a uniform circular jet perpendicular to and impinging on the ground was studied experimentally and theoretically in order to further the understanding of the aero- dynamic processes associated with ground particle entrainment in the impinging downwash from VTOL aircraft.</p> <p>Experimental data have been obtained for the flow in the deflected jet and in the ground boundary layer for jet height-to-nozzle diameter ratios (H/D) from 0.25 to 4 and for two mass flows. The boundary layer measurements were obtained at radial stations between one-half and four nozzle diameters from the stagnation point.</p> <p>The flow field of an inviscid uniform jet perpendicular to the ground was analyzed theoretically, based on a vortex sheet model, and partial results obtained. Boundary layer analyses were performed for the laminar region which occurs up to approximately one jet diameter from the stagnation point and for the region beyond two jet diameters from the stagnation point where the flow is of the wall-jet type. These two regions were joined by means of a semi- empirical analyses based on an assumption as to loss in momentum flux in the transition zone joining the laminar boundary layer and the wall-jet flow. Comparisons between the results of the theoretical analyses and the experimental results are made.</p>	<p>UNCLASSIFIED</p> <p>1. Vertical Takeoff Planes 2. Downwash Impingement</p> <p>I U.S. Army Transportation Research Command, Ft. Eustis, Va. II Cornell Aeronautical Laboratory, Inc., Buffalo, N. Y. Contract DA 44-177-TC-782 Brady, W. Gordon Ludwig, Gary R.</p>	<p>UNCLASSIFIED</p> <p>1. Vertical Takeoff Planes 2. Downwash Impingement</p> <p>I U.S. Army Transportation Research Command, Ft. Eustis, Va. II Cornell Aeronautical Laboratory, Inc., Buffalo, N. Y. Contract DA 44-177-TC-782 Brady, W. Gordon Ludwig, Gary R.</p>